THE OPTIMISATION OF SHEET THICKNESS IN SUPER-PLASTIC FORMING

Aoshuang Huang
B.E. (Beijing Institute of Technology)

June 1998

A thesis submitted for the degree of Master of Engineering of The Australian National University

Department of Engineering
Faculty of Engineering and Information Technology
The Australian National University

Declaration

This thesis contains no material which has been previously accepted for the award of any other degree or diploma in any university, institute or college, and contains no material previously published or written by another person, except where due reference is made.

Canberra, June 1998.

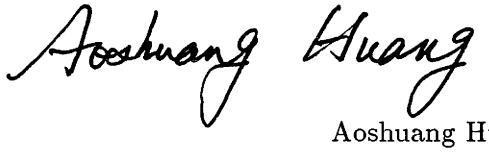

Aoshuang Huang
Department of Engineering
Faculty of Engineering and Information Technology
The Australian National University
Canberra ACT 0200, AUSTRALIA.

Conference Paper:

M. Cardew-Hall, A. Huang, "*Sheet Thickness Optimisation for Superplastic Forming of Engineering Structures*," Australasia-Pacific Forum on Intelligent Processing and Manufacturing of Materials, July 14–17, 1997, Gold Coast, Australia.

Abstract

This thesis investigates the optimisation of sheet thickness in superplastic forming. Two optimisation strategies, gradient search and proportional control, are explored for determining the initial sheet thickness based on the FE simulations to ensure final thickness. Experiments are then held to validate the simulation results.

Simulations which are developed on the FE code ABAQUS/Standard, show that the results from gradient search technique are acceptable in terms of the optimised thickness obtained in 2-D cases, but display poor criterion convergent rates and low thickness accuracy. Conversely proportional control algorithm yields not only high criterion convergent speeds but good consistence with the target thickness. Also its application can be extended to 3-D models.

Experiments are conducted based on Sn-Pb eutectic alloy which exhibits superplasticity just above room temperature. Sheets with 2 mm thickness and the optimised thickness towards 1 mm thick component are inflated into a dome shape under constant pressures. Good agreements with the simulation results are achieved.

Acknowledgements

I would like to thank the following people. Their contributions have made this project possible:

- Mick Cardew-Hall for my academic supervision,
- Chunyan for love and support,
- Mum and Dad for their commitment to my education,
- Martin Stonebridge for his fresh ideas and helpful discussions,
- Shankar Kalyanasundaram for advice on finite element analysis,
- Matthew James for advice on mathematical model,
- Adrian Lowe, Darius Krivanek and Rob Gresham for establishing experimental rig and
- Bob Waterford for EDM cutting.

Contents

List of Figures

List of Tables

Notation

A	material constant (equivalent to $\frac{1}{k}$)
E	Young's Modulus
P_r	pressure of the die entry radius
R_l	die entry radius
$\mathbf{T}, T$	sheet thickness
T_m	melting point of alloy in Kelvin
g	gas pressure
h	sheet thickness
k	material constant (equivalent to $\frac{1}{A}$)
m	strain rate sensitivity
p	proportional control parameter in proportional control method
r	geometric inhomogeneity of tensile specimen
t	time
$\mathbf{t}, t$	component thickness
Δt	time increment
ε	strain
$\dot{\varepsilon}$	strain rate
λ	step length in gradient search method
μ	coefficient of friction
ν	Poisson's ratio
ρ	density
σ_f	flow stress
σ_h	through thickness stress of sheet
σ_w	in-sheet stress in the width direction

$\bar{\sigma}$ yield stress

Bold face indicates a vector or a matrix. Where variables are multiply defined the definition is obvious from the context.

Chapter 1

Introduction

1.1 The Research Problems

Superplastic materials are polycrystalline solids which have the ability to undergo large uniform strains prior to failure [6]. Although extensions greater than 1000% occur in some materials, it is usually, for deformation in uni-axial tension, indicative of superplasticity while elongations to failure in excess of 200%. The highest elongations reported are 4850% and 7750% in a Pb-Sn eutectic alloy; 5500% and greater than 8000% for an aluminium bronze (figure 1-1).

Superplastic behaviour were initially observed in the late 1920's when it was found a maximum elongation of 361% for the Cd-Zn eutectic at $20^{o}C$ and strain rates of 10^{-8}/s, and 405% at $120^{o}C$ and a strain rate of 10^{-6}/s [7]. However, the most spectacular of the earlier observations was done by Pearson [2] who, while working on eutectic, reported a tensile elongation of 1950% without failure for a Bi-Sn alloy in 1934 (figure 1-2).

An increasing interest came in 1962 when Underwood presented a review article [8]. Backofen and his colleagues showed in 1964 that the superplastic Zn-Al alloy could be formed into a practical shape by a simple air-pressure operation [9]; four years later in

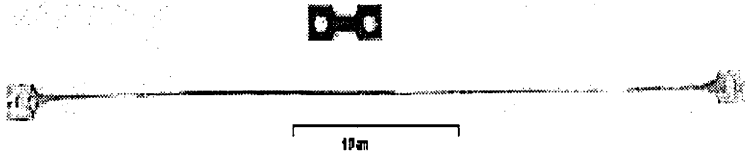

Figure 1-1: The extraordinary elongation (8000%) achieved in a Cu–Al alloy by Higashi [1].

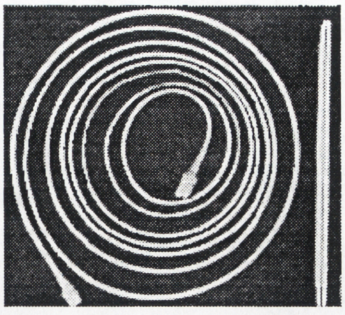

Figure 1-2: Pearson's famous photograph in 1934 of a Bi–Sn alloy that has undergone 1950% elongation [2].

1968 Chaudhari published the review paper on this subject [10]; and in the next year the first book, *Superplasticity of Metals and Alloys* was published by Presnyakov [11]. After that monographs were published by Western, Soviet and Japanese researchers [3].

It was the 1982 international conference entitled *Superplastic Forming of Structural Alloys* which showed how great the interest was in the subject of fine-structure superplasticity from both academic and commercial viewpoints. It was also the first conference fully dedicated to the subject of superplasticity [3].

Superplastic forming (SPF) is a manufacturing process whereby certain materials, under the correct conditions of temperature and strain rate, exhibit high ductility resulting in large strain deformations. This property has allowed the development of forming operations which permit thin sheet to be blown into die cavities to produce complex engineering structures. It involves large deformation, large strain, nonlinear material behaviour and, usually, deformation dependent boundary conditions.

Superplastic forming is becoming an important manufacturing technique, especially in industries where weight saving is of critical importance [12]. It has led to considerable commercial interest using techniques similar to those developed for the bulge forming of thermoplastic. Superplastic forging of nickel-base alloys has been used to form turbine discs with integral blades, while diffusion bonding and superplastic forming (DB-SPF) of titanium alloys is used to produce fan and compressor blades for aero-engines. Aluminium alloys can be used in the fabrication of air-frame control surfaces and small scale structural elements where low weight and high stiffness are required. Non-aerospace applications of Al alloys include containers with complex surface profiles and decorative panels for internal and external cladding of buildings.

Commonly a superplasticly formed part is produced from inflating a flat sheet with

uniform thickness into some intricate geometric shape. However this practice usually yields a product with thinner portions where the shape of the die is complex — this is sometimes undesirable because of the high stresses in those areas. So thinning control as a technique has been applied in fabrication, including material treatment, lubrication application, thermo-forming methods, profiled gas pressure and etc..

It would be advantageous to be able to design the initial thickness distribution of the blank, in other words, to optimise the initial sheet thickness, so that a prescribed final (either uniform or varied) thickness profile can be obtained directly from superplastic inflation. Machining or chemical milling processes can be employed to get the desired thickness distribution over the blank. It is , however, much more economical to remove the materials from the blank sheet, which is initially flat, than from the inflated part whose geometry is usually complex.

This thesis investigates the optimisation with two kinds of method. One is the gradient search technique, a classic method widely applied in various problems; the other is called "proportional control" which is developed for the particular circumstance of SPF. Also a set of experiment works is performed to verify the results of computer simulations.

1.2 Aims

The aims of this research project are as followings:

- To simulate the SPF process correctly by using ABAQUS, a commercial finite element analysis (FEA) package. Both 2-dimensional and 3-dimensional simulations are to be done in the shapes of hemispherical dome, flat pan and rectangular box. Two kinds of forming conditions will apply – constant maximum strain rate by which ABAQUS calculates the correspondent pressure for each time interval, as well as constant pressure which is quite straight forward.

- To optimise the initial flat sheet thickness profile, using classic optimisation method, so that final constant thickness profile can be achieved after the forming process.

- To develop a efficient method for the same purpose mentioned above in view of this particular SPF situation. The method should have fewer iteration times, fast converging speeds, and ease of programming. And comparison of these two methods should be made as well.

- To conduct a series of experiments to verify the simulation results. In order to corroborate the outcome properly, grain structure of the material should be maintained in the correct state.

1.3 Organisation of the Thesis

This thesis is presented in seven chapters. The remaining chapters are structured as followings:

Chapter two commences with a brief review of superplasticity and superplastic forming process.

Chapter three presents both implicit and explicit finite element mathematical models used by ABAQUS/Standard and ABAQUS/Explicit, and the geometry models adopted by ABAQUS in later simulations. Also material properties and loading controls are described at the end.

Chapter four reviews the classic optimisation methods which have been extensively applied in various optimisation problems.

Chapter five presents two kinds of optimisation methods, the gradient search technique and the proportional control method, to solve the optimisation problem of SPF. The gradient search is one of the most powerful common method used in general problems, whereas the proportional control method is specially designed for SPF sheet thickness profile optimisation. Comparison and analysis are also made at the end of this chapter.

Chapter six describes the material properties of Pb-62%Sn eutectic alloy, the design of SPF experimental rig, analyses of the grain structures of rolled sheets, and also presents the results of experimental verifications performed.

Chapter seven summarises the main conclusions of the study and provides some recommendations for the further research in this area.

Chapter 2

Literature Review

A general literature review about superplasticity, superplastic material and SPF processes is presented in this chapter. The mechanism of superplastic behaviour and superplastic materials are exceptional and complex comparing with those of conventional processes and materials of manufacturing. Currently a great deal of research work is being carried out in this field.

2.1 Superplasticity and Superplastic Materials

2.1.1 Superplasticity

Superplasticity is a term used to indicate the exceptional ductility that certain metals can exhibit when deformed under proper conditions. Mostly the term refers to the ductile tensile behaviour of the material. There are several different types of superplasticity in terms of the microstructural mechanisms and deformation conditions [4], including:

- micrograin superplasticity,
- transformation (or environmental) superplasticity and
- internal stress superplasticity.

Superplasticity is a very complex property of materials, and only the micrograin superplasticity is of importance in the fabrication of parts at this current stage [4], so the review presented in this thesis will be limited to this type.

For micrograin superplasticity, the high ductilities are observed only under certain conditions, and the basic requirements are:

- fine grain size material (normally less than 10 μm),
- relatively high temperature (greater than $0.5T_m$, where T_m is the melting point in Kelvin)[1], and
- controlled strain rate ranging from 10^{-5} to 10^{-1}/s,

But Nieh argued in his book [3] that "historically simple concepts regarding key characteristics of superplastic materials are no longer appropriate". Superplastic material, which was formerly believed to be a metallic two-phase material with a uniform, fine, equiaxed, grain (phase) size, covers much broader areas defined by the description — "Metallic, ceramic, intermetallic, or composite multiphase materials with uniform or nonuniform, relatively coarse (20 μm) to ultrafine (20 nm) grain sizes that have isotropic or anisotropic grain (phase) shape, size, or orientation."

However material superplasticity itself is not the goal of this thesis, and therefore let us leave it to the researchers specialised in that field.

The Governing Equation

Superplastic alloys generally exhibit high values of the strain rate sensitivity exponent m during tensile deformation, which is characterised by the constitutive law:

$$\sigma_f = k\dot{\varepsilon}^m \tag{2.1}$$

where σ_f is the true flow stress, k is a material constant, and $\dot{\varepsilon}$ is the strain rate. For superplastic behaviour, m would be equal or greater than 0.3 and for the majority of superplastic alloys m lies in the range 0.4 to 0.8 [6], whereas most other metals and alloys normally exhibit $m < 0.2$.

Pilling [6] explained the mechanism of m in superplasticity quite clearly. Supposing necking happens in the tensile process, it would lead to a locally high strain rate. With high strain rate sensitivity m, high strain rate then results in a sharp increase in the flow stress within the necking region, hence inhibits further development of necking, so that high tensile elongations could be expected.

Rewriting equation 2.1 by taking logarithm of both sides, gives

$$\ln\sigma_f = k' + m\ln\dot{\varepsilon} \tag{2.2}$$

[1]Nieh [3] pointed out that, typically, superplastic temperature is greater than $0.75T_m$. However from author's experience, $0.75T_m$ is quite suitable for Pb-Sn alloy.

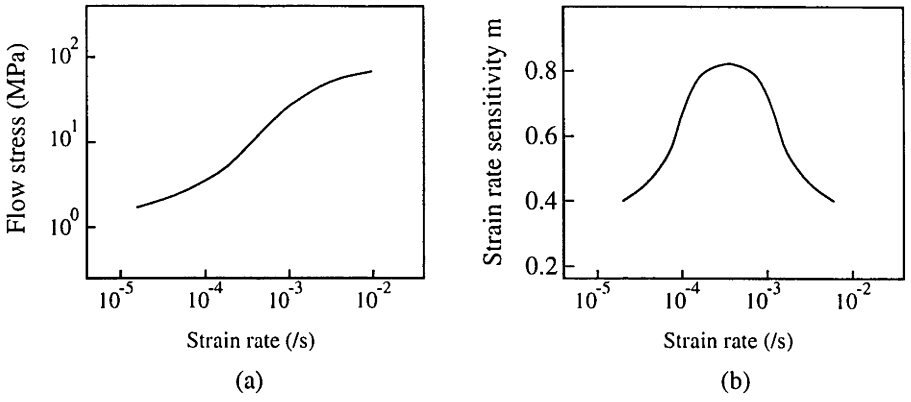

Figure 2-1: (a) Variation of the flow stress with strain rate; (b) Variation of the sensitivity m with strain rate.

then

$$m = \frac{\partial \ln \sigma_f}{\partial \ln \dot{\varepsilon}} \tag{2.3}$$

It is clear from above equations that, by logarithmically plotting σ_f and $\dot{\varepsilon}$, the slope of the plot is the sensitivity m. Interestingly most superplastic materials show a sigmoidal variation between σ_f and $\dot{\varepsilon}$ (figure 2-1(a)). This implies that maximum m (slope) exists (figure 2-1(b)).

Strain Rate Sensitivity

Typical superplastic materials have a strong dependence with the strain rate sensitivity m, and there is a good relationship between the m value and superplastic ductility. Although the total elongation can also be affected by fracture, the strain rate sensitivity takes the first-order effect.

The parameter which is commonly selected to measure the superplastic formability is the tensile elongation at the optimum temperature and strain rate. Tensile elongation can be measured as a function of strain rate, as it is a highly strain rate sensitive property and the real components can experience significant variations in strain rate during forming. An alternative is to determine the strain rate sensitivity of the flow stress, m, which has been proved to correlate well with tensile elongation for different classes of materials [13]. Measurements of flow stress and strain rate sensitivity of flow stress can be conducted in a step strain rate test and can be used to determine the optimum strain rate for superplastic forming [14].

Although strain rate sensitivity is the dominant parameter in superplastic forming, more recent results show that a significant amount of hardening can occur as a function of superplastic strain even at a constant strain rate [15, 16]. This type of strain hardening is believed to be related primarily to the grain growth that occurs during superplastic forming.

Forming Temperature

Forming temperature is just as important as the strain rate in SPF. Temperature variation in a forming die is a primary source of localised thinning. Therefore characterisation of material behaviour should include not only determination of the optimum superplastic temperature but also the sensitivity of flow stress and elongation to temperature. A large temperature sensitivity of flow stress is not desirable, because local hot spots will lead to severe strain localisation.

2.1.2 Superplastic Materials

Although superplasticity is the exceptional property of some materials, a great number of superplastic materials have been found or developed. The diversity of superplastic materials has enable researchers to exploit this property in a wide range of applications. Metal alloys used to dominate superplastic materials. However more classes of material join the superplastic material group with more complex mechanisms, such as ceramics, intermetallics and laminates. Furthermore, some of the new materials have high-strain-rate superplasticity and can be deformed at room temperature. From commercial viewpoints these features are very attractive.

Understanding advanced superplastic materials requires more professional knowledge. Excessive discussion of those materials will not help to achieve the goal of this thesis. So the review of superplastic material presented below is only limited to basic alloys, such as aluminium, titanium, magnesium and nickel-based alloys.

Aluminium-Based Alloys

The first observation of superplasticity in an aluminium alloy was probably by Petty [17]. Superplasticity and superplastic-like behaviour were found in the alloys containing 7.9 to 40.4 wt% Cu.

Most of the early studies on superplastic aluminium alloys were based on the Al-33wt%Cu eutectic system. This is because researchers tried to stabilise grain structure and prevent rapid grain growth by ensuring approximately equal volume fractions of two phases. Academic studies on aluminium alloys were largely centred on eutectic structure like Al-Cu, Al-Ca, Al-Si and Al-Pd, whereas other significant studies on noneutectic structure, such as Al-Cu-Mg, Al-Zn-Mg, Al-Mg-Si and Al-Mg-Zr, were also carried out [3].

Ground breaking work was carried out by Stowell, Watts and Grimes with superplastic Al-Cu alloys in 1969. They rendered superplasticity to a dilute aluminium alloys (Al-6%Cu-0.5%Zr) with the introduction of relatively high levels of zirconium in solution via specialised casting techniques and subsequent thermal treatment to create extremely fine $ZrAl_3$ precipitates. This work was not reported until 1976 [18]. These dilute alloys containing zirconium are lately known by the trade name – SUPRAL. They are heavily cold worked into sheet and dynamically recrystallised to a fine stable grain size, typically 4-5 μm, during the initial stages of hot deformation. Superplastic tensile elongations to failure approaching 2000% have been measured in SUPRAL alloys.

In recent years most efforts have been made on developing superplastic properties in existing commercial compositions, instead of creating a superplastic alloy and then attempting to develop it for commercial compositions. This trend reflects the extreme difficulty of introducing new alloy systems into our society [3]. The commercial alloys, such as Al 7000 series alloys, Al-Li alloys, Al-based metal-matrix composites and mechanically alloyed materials, are thermomechanically processed to develop superplasticity. It is worthy to note that Al-based metal-matrix composites and mechanically alloyed materials exhibit superplasticity at unusually high strain rates up to 0.1-1.0 /s.

Aluminium-lithium alloys are primarily of great interest for the aircraft and aerospace industries because Li is the one of only three elements that significantly increase the elastic modulus and simultaneously decrease the density of aluminium. For aerospace and aircraft applications, improvements in specific modulus and specific strength can lead directly to weight savings.

Titanium-Based Alloys

Superplasticity in some titanium alloys was known more than 20 years ago [13]. There are two main reasons of particular interest in titanium alloys. Firstly, they can exhibit good superplasticity. Secondly they are expensive and difficult to fabricate into structural shapes by traditional forming and machining methods. It has been shown that superplastic forming can offer the potential for significant cost savings for the construction of structure of titanium alloy parts. Many commercial applications of the superplastic forming process for titanium alloys have been successful. However, to achieve further improvements in the process and a reduction of costs, improved superplastic titanium alloys need to be developed.

Most of the experimental studies as well as commercial applications have focussed on Ti-6Al-4V alloy. This alloy has found wide-spread application because of its desirable structure properties. Studies show that a range of titanium-based alloys can be superplastic , including Ti-6Al-5V[19], Ti-6Al-2Sn-4Zr-2Mo[20], Ti-6Al-4V-2Ni[21], Ti-6Al-4V-2Co[21], Ti-6Al-4V-2Fe[21], Ti-5.8Al-4.0Sn-3.5Zr-0.7Nb-0.5Mo-0.3Si-0.05C[22] and etc..

Superplasticity in fine-grained ($\sim$0.5 μm) Ti-12Co-5Al and Ti-6Co-6Ni-5Al alloys was reported by Liu [23]. In these two alloys, grain growth was inhibited by a significant amount ($\sim$27% in volume) of intermetallic particles, Ti_2Co and Ti_2Ni, during superplastic forming . A maximum superplastic elongation of over 2000% was observed at a strain rate 3×10^{-2}/s and at relatively low temperature $700^{o}C$. Obviously the relatively high strain rate and low temperature were attributed to finer grain sizes in these two alloys compared with those in the other superplastic titanium alloys, which are typically around 5-10 μm [15].

Magnesium-Based Alloys

Magnesium alloys have the inherent advantage of being light. They are less dense than fibreglass and just over half as dense as aluminium. Magnesium is also an abundant element. Thus, there are many potential opportunities for the use of magnesium alloys in automotive industry. This is not only because of magnesium's relatively low density, which can reduce vehicle weight, but also its good damping characteristics, dimensional stability, machinability and low casting costs. These desirable attributes enable mag-

nesium to economically replace many zinc and aluminium die castings, as well as cast iron and steel components and assemblies in automotive drive trains. However their poor corrosion resistance limits their structural applications.

The study of superplasticity in magnesium alloys was begun as early as the 1960s, and primarily on Mg-6Zn-0.5Zr (ZK60) alloy. One of the important findings was that the grain size of the alloy must be smaller than 10 μm in order to gain superplasticity .

In the case of extrusion, elongations of 600% are obtainable for AZ61A with 6-8 μm grain size when extruded at 290^oC at an initial strain rate of 3.3×10^{-4}/s. Greater than 700% elongation was recorded for ZK60A of 4-5 μm grain size when deformed at 310^oC and at higher initial strain rate of 3.3×10^{-3}/s. ZK60A appears to be a more practical alloy for superplastic forming than AZ61A, because that ZK60A has higher strain rates and retains more strength than AZ61A when both are superplastically deformed to the same extent.

For sheet forming, apart from ZK60A and AZ61A, studies have been carried out on two British alloys ZW1 (Mg-1Zn-0.5Zr) and ZW3 (Mg-3Zn-0.5Zr), AZ31 and Mg-12Al [24]. These alloys can be thermomechanically processed into fine-grained structures, and they are all superplastic under the appropriate testing conditions.

Nickel-Based Alloys

The research of superplasticity in nickel-based alloys began as early as 1960s. So far superplasticity has been observed in a variety of nickel-based alloys, including cast alloys. Similar to the situation of aluminium alloys, there is relatively little interest in developing new superplastic nickel alloys, and work on superplastic nickel has been primarily focussed on existing alloys.

The most significant progress of Ni-based alloys is probably the development of superplastic Inconel 718 alloy (composition by wt%: 50-55 Ni, 17-21 Cr, 4.8-5.25 Nb, 2.8-3.3 Mo, 0.651 Ti, 0.2-0.8 Al, 0.35 Mn, 0.03 C, 0.015 S, bal Fe) [25]. Inconel 718 was developed by Inco Alloys International Inc. in the early 1960s. It is widely used in jet engine parts such as compressor and turbine disks and rings, turbine shafts, exhaust sections, hot air ducting and fasteners. The alloy is made by vacuum induction melting and electroslag remelting. It can be conventionally hot-worked, then cold processed to make a sheet product with a grain size of 5 μm. The grain size is sufficiently stable at

temperature about 980^oC or less to permit superplastic forming . An elongation value of over 700% can be obtained at a strain rate of 1.33×10^{-5}/s.

2.2 Superplastic Forming

2.2.1 Superplastic Forming Processes

Quite a few methods and techniques have been reported for forming superplastic parts, including:

- blow forming,
- vacuum forming,
- thermo-forming,
- deep drawing,
- superplastic forming /diffusion bonding (SPF/DB),
- forging,
- extrusion and
- dieless drawing.

However only those methods that relate to sheet metal forming will be described in this section.

Blow Forming and Vacuum Forming

Blow forming and vacuum forming are basically the same process which imposes a gas pressure differential so that the superplastic diaphragm is formed into the die configuration. Limited by atmospheric pressure (100 kPa or 15 psi), the forming rate and capability in vacuum forming are therefore limited. In blow forming sufficient pressure can be provided by a pressure reservoir where a maximum pressure of 690 to 3400 kPa (100 to 500 psi) is typically used.

The principle of blow forming is illustrated in figure 2-2, which shows a cross section of the dies and forming sheet. Normally the dies and sheet are maintained at the forming temperature for the whole process. The sheet is formed into the lower die by the imposed gas pressure. The gas in the lower die chamber is vented to atmosphere, or can also be held under vacuum. If necessary a back pressure can even be imposed to suppress cavitation (see section 2.2.3).

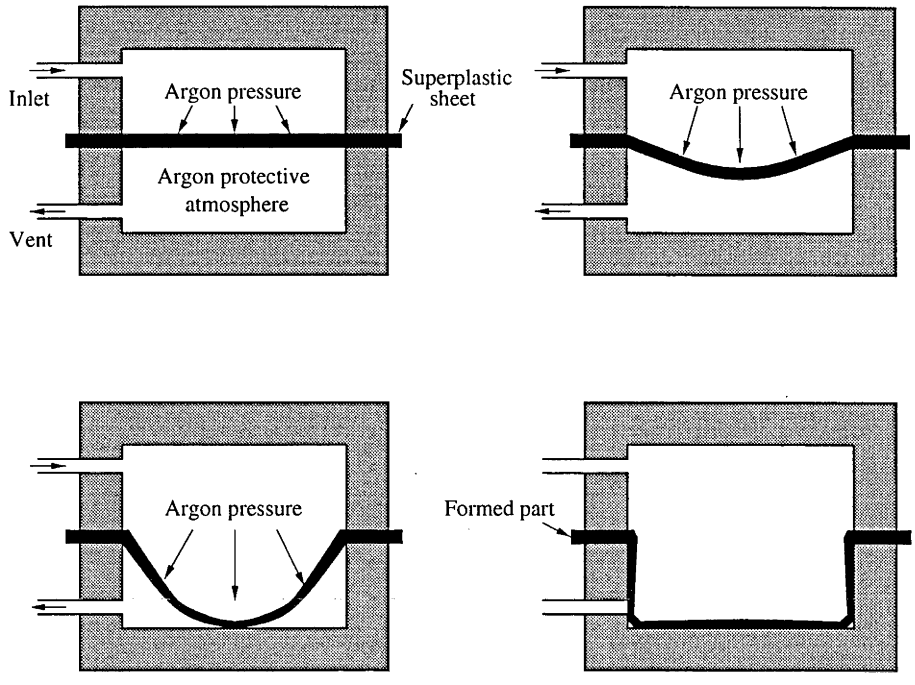

Figure 2-2: Schematic of blow forming for superplastic forming.

It is desired to maintain the induced strain rate in the forming sheet in the superplastic range by varying the gas pressure. The pressure amplitude curve can be determined by either trail and error or the application of analytical modelling methods. In order to prevent a sharp increase of strain rate and consequent rupturing the part, this pressure generally rises slowly.

This process has been successfully used in structural and ornamental parts from titanium, aluminium and other metals. An example in which a titanium aircraft nacelle frame is formed by blow forming is illustrated in figure 2-3. In this case, the forming is conducted at about 900^oC (1650^oF), and to prevent oxidation due to reactivity of titanium, inert gas (argon) is used on both side of the sheet[2]. By superplastic forming and diffusion bonding the frame is fabricated in one piece (figure 2-3(A)), and consequently resulting in a 33% weight savings and a 55% cost savings. By conventional technique the frame is made by eight separate pieces of the alloy which then have to be joined with 96 fasteners (figure 2-3(B)),

Large, complex parts can be readily formed by blow forming. It has the advantage that no moving die components (that is, no double-acting mechanisms) and mated

[2]Such protective gas usually is not necessary for aluminium alloys.

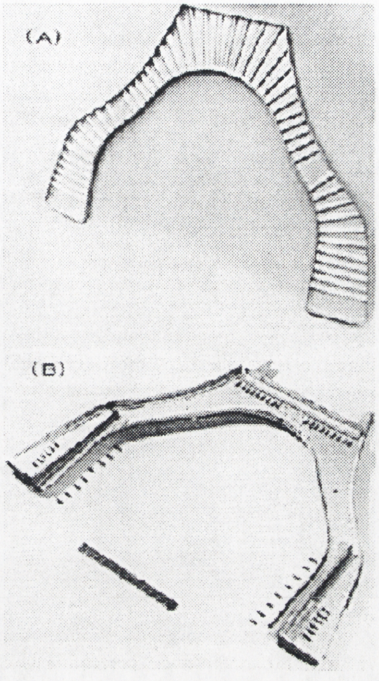

Figure 2-3: Ti-6Al-4V aircraft nacelle frames [3]. (A) Redesigned frame by superplastic forming; (B) Former frame by conventional techniques.

die components are required. Multiple parts can be formed in a single process cycle, thus production rate of some parts may be increased, though superplastic forming is recognised a fairly slow process compared with conventional forming techniques. These features are fully embodied in above example.

Thermo-Forming

Thermo-forming methods have been developed from conventional plastic technology for superplastic forming. Apart from using imposed gas pressure or vacuum, a movable or adjustable die member may be also applied [26, 27]. Figure 2-4 shows two examples of thermo-forming methods. In figure 2-4(a), an undersize male punch moves up first to stretch the sheet, and then followed by applying gas pressure to form the stretched sheet against the die configuration. In figure 2-4(b), gas pressure is applied first to blow a bubble. The male tool then moves into the bubble, and the pressure is reversed to cause the sheet to conform to the shape of the tool.

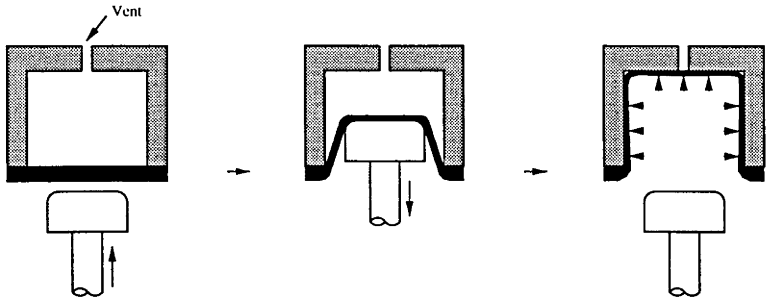

(a) Plug assisted forming into a female die cavity.

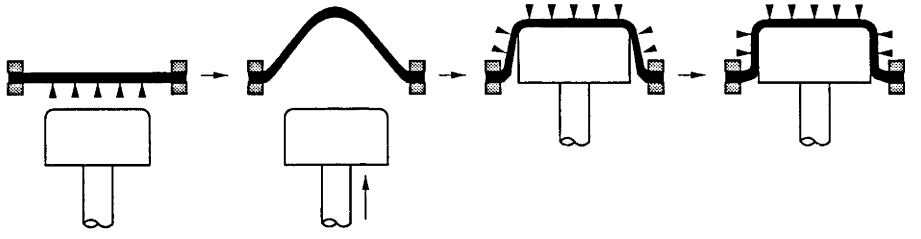

(b) Snap-back forming over a male die that is moved up into the sheet.

Figure 2-4: Two processes of thermo-forming method used in superplastic forming [4].

Deep Drawing

Although deep-drawing studies have been conducted with superplastic metals, this process does not appear to offer many significant advantages in superplastic forming[4]. Conventional deep-drawing depends on strain hardening to achieve the required formability and to prevent thinning and rupture during forming process. Superplastic materials do not strain harden to any great extent, however, they depend on the high strain rate hardening for their forming characteristics, and this property seems to offer little aid to deep-drawing.

In order to draw in the flange, the material in contact with the punch nose, as well as that in the sidewall , must be hard enough to carry the increasing stresses required to draw in increasing amounts of the flange. But no significant work hardening occurs at superplastic temperature, and the punch therefore typically pieces the blank, or the blank fails in the cup walls if the frictional constraint between the punch and the blank is high. However a maximum draw ratio of 2:1 has been developed for the zinc-aluminium alloy under an optimised conditions [4].

Hawkins provided a technique which can improve the drawability of superplastic

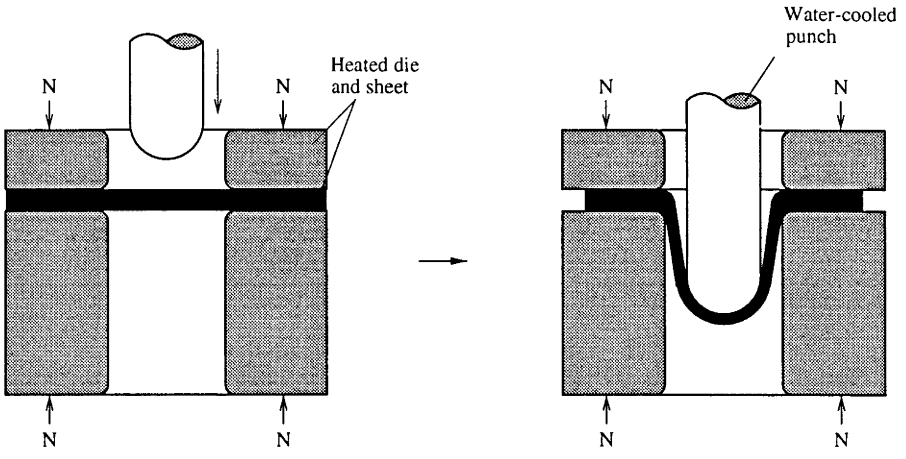

Figure 2-5: Deep drawing.

alloys [28]. This method, which is shown in figure 2-5, uses a punch cooled to a temperature below that of the forming blank, whereas the clamper is maintained at the forming temperature, so that the material around the punch nose has less superplasticity. This differential temperature technique permits an substantial increase in the limit drawing ratio from less than 2.4 : 1 to more than 3.75 : 1.

Another concept evaluated to explore the deep-drawing capability is given by Al-Naib [29]. In this method a high oil pressure is imposed around a blank periphery to aid drawing. It is actually a combined extrusion and drawing precess. Tin-lead eutectic was used in this study to permit processing at room temperature. Good control of wall thickness was achieved, but the applicability of the process to alloys requiring high temperature was not demonstrated.

SPF/DB Processes

Some unique processes are available if joining methods, such as diffusion bonding, can be combined with superplastic forming. These processes are generally referred to superplastic forming and diffusion bonding (SPF/DB) [30]. Diffusion bonding is based on the property of fine-grained superplastic materials that they can often be readily bonded in the solid state, either to themselves or to other nonsuperplactic materials. This type of bonding is possible because of the presence of many grain boundaries in fine-grained materials that act as short-circuit paths of diffusion [31].

Although diffusion bonding is not a sheet forming process, it complements and enhances superplastic forming to a great extent. Concurrent SPF/DB has been recognised

as an important and viable manufacturing technology which can provide with both cost and weight saving, compared with conventional manufacturing method [32].

The SPF/DB process successfully combines the SPF and DB processes because the process temperature requirements of both are similar. The low flow properties characteristic of the superplastic alloys aid the DB pressure requirements, and it has been found that many superplastic alloys can be diffusion bonded under pressures in the same low range as that of SPF processing (typically 2100 to 3400 kPa, or 300 to 500 psi). The SPF method used in SPF/DB so far is blow forming.

The SPF/DB process has the following variations:

- Forming of a single sheet onto a pre-placed details followed by diffusion bonding (figure 2-6(a)).
- Diffusion bonding of two sheets at selected locations, followed by superplastic forming of one or both into a die (figure 2-6(b)), the reverse sequence can also be applied.
- Diffusion bonding of three or more sheets at selected locations under pressure, followed by inflation under internal gas pressure to form the two outer sheets into a die (figure 2-6(c)). In this process the inner sheet(s) is(are) stretched into a core configuration.

In order to develop diffusion bondings only in the predetermined local areas, various techniques have been used. One of these adopts stop-off material between the sheets where no bonding is required. For different alloys and temperatures, the stop-off material may be different. After the diffusion bonding operation, the areas suspended by the stop-off materials are not bonded, and gas can be imposed internally in these areas, thus causing the external sheet to be separated and expanded into a surrounding die.

2.2.2 Thinning Characteristics

To take advantage of the high elongations possible with superplastic materials, it is necessary to accept the accompanying significant thinning in the sheet material, which is a natural consequence of the deformation conditions. For large tensile strains, the thinning will be correspondingly large. Although the superplastic materials are effective in resisting the necking process, they nevertheless do neck, and thinning gradients do

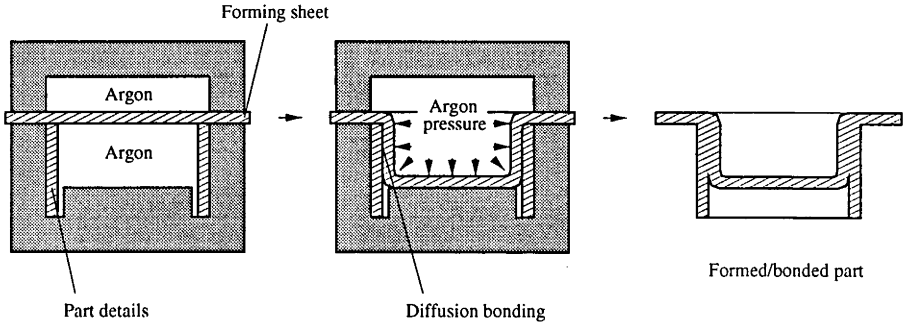

(a)

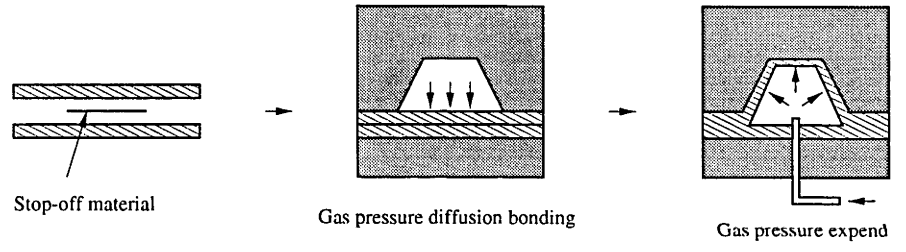

(b)

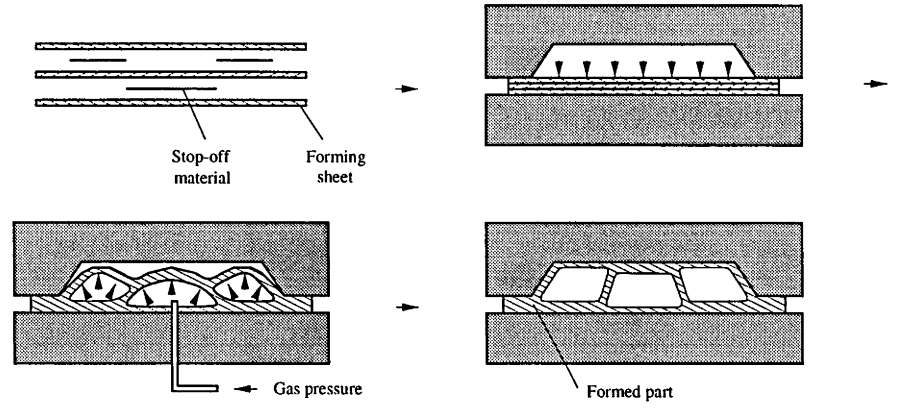

(c)

Figure 2-6: The SPF/DB processes. (a) Forming single sheet onto details; (b) Operations of joining two sheets; (c) Operations of joining three sheets.

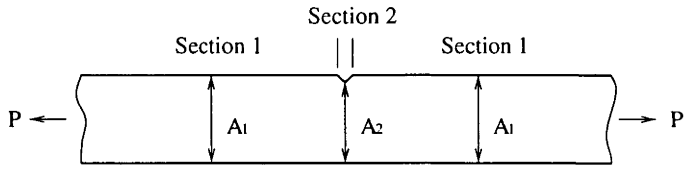

Figure 2-7: Inhomogeneous specimen.

develop [4]. Therefore, in the design and processing of SPF parts, it is important that the thinning be understood and considered.

For superplastic deformation, elastic strains are negligible, therefore constancy of volume can be assumed. From this consideration, the sum of the plastic strains is *zero*, which implies that tensile strain in one direction must be balanced by compressive (negative) strains in another, that is

$$\varepsilon_1 + \varepsilon_2 + \varepsilon_3 = 0 \tag{2.4}$$

where ε is the strain, and the subscripts indicate the principal directions.

It has been shown that superplastic deformation occurs when strain rate sensitivity m is large and deformation process is predominately post-uniform, in contrast to conventional metal tensile behaviour. However all deformation is virtually nonuniform in most cases. The thinning in the tensile specimen can be assumed to be the result of a preexisting inhomogeneity which can grow under the imposed deformation [33, 34].

The rate of thinning in the tensile specimen is determined by both the size of inhomogeneity and the m value [4]. Paton and Hamilton [35] have demonstrated analytically for an idealised tensile specimen (figure 2-7) containing a geometric inhomogeneity which is designated by r, that is

$$r = \frac{A_1 - A_2}{A_1} \tag{2.5}$$

where A_1 and A_2 are the sections areas of perfect and imperfect sites respectively. And the correspondent stresses in these two areas are:

$$\sigma_1 = \frac{P}{A_1} \tag{2.6}$$

$$\sigma_2 = \frac{P}{A_2} = \frac{P}{A_1(1-r)} \tag{2.7}$$

This analysis follows the strain development both inside and outside the inhomogeneity,

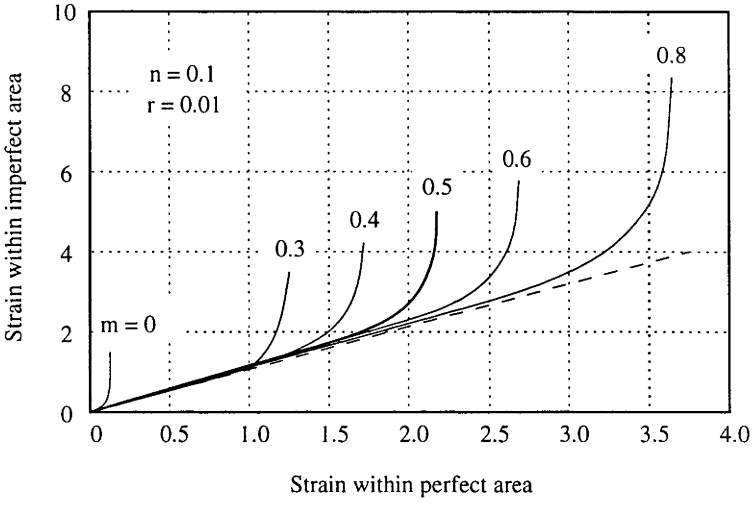

Figure 2-8: Calculated strains inside and outside an inhomogeneity in tensile specimen for various m values [4].

assuming that the applied load is fully transferred along the length of the specimen and that the material obeys the constitutive equation

$$\sigma = K\varepsilon^n \dot{\varepsilon}^m \tag{2.8}$$

where n is the strain-hardening exponent. The results of calculations using equation 2.8 are shown in figure 2-8, in which the strain in the inhomogeneity is plotted as a function of the strain outside the inhomogeneity for a number of m values. The extent of the thinning in the tensile specimen is shown to be strongly related to the m value, although thinning gradient will develop at all m values if the strain is sufficiently large. The inhomogeneities in tensile specimens have also been found to relate to the strain rate [36].

Spherical Domes

Although the thinning in superplastic tensile test specimens is the result of geometric inhomogeneities, the corresponding thinning in biaxially formed parts is usually the result of local stress state differences [4]. These differences subsequently lead to the development of geometric inhomogeneities. In all these cases the difference in the local stresses leads to strain rate gradients, and the strain rate gradients develop directly into thickness gradients. A major difference between the tensile specimen and the formed part is that, in the tensile specimen, the stress gradients can be varied by dimensional

control during machining, whereas in formed parts the configuration determines the stress state, which is not adjustable without changing the geometry.

The concept of thinning during superplastic forming process is perhaps best understood in terms of the bulging of a sheet [27, 5, 37, 38, 39, 40, 41, 42].

In this geometry, there is a stress state gradient from the pole of the dome to the edge. Suppose the dome is inflated into a configuration of hemisphere, the orthogonal stresses are equal at the pole, and the stress state is that of equibiaxial tensile; whereas at the edge of the dome, there is constrain around the periphery, leading to a plane-strain stress state. As the flow behaviour of superplastic metals has been found to obey the von Mises criterion [43], the effective stresses are

$$\bar{\sigma} = \frac{1}{\sqrt{2}}\left((\sigma_\theta - \sigma_\phi)^2 + (\sigma_\phi - \sigma_t)^2 + (\sigma_t - \sigma_\theta)^2\right)^{\frac{1}{2}} \tag{2.9}$$

If assuming that the through-thickness stress is small with respect to the in-plane stresses, the effective stresses at the pole and edge can be expressed in terms of the meridional stress σ_θ as

$$\bar{\sigma}_{pole} = \sigma_\theta \tag{2.10}$$

$$\bar{\sigma}_{edge} = \frac{\sqrt{3}}{2}\sigma_\theta \approx 0.87\sigma_\theta \tag{2.11}$$

Therefore, the pole experiences 15% higher flow stress than the edge, resulting in a higher strain rate. Imposing the concept of local geometric inhomogeneity of tensile specimen, r is 0.13.

Apart from the factor of geometry, strain rate sensitivity m also plays an important role in thinning characteristics. The initial strain rate difference between the pole and the edge depends on m value; larger m value gives smaller strain rate difference and less tendency to develop a thickness gradient. Therefore the stress gradient in a forming dome causes a more rapid thinning rate at the pole, and it may be expected that the thinning difference will accelerate with time, leading to a thickness gradient in the formed dome.

Figure 2-9 shows the different thickness profiles for bulge-formed sheets with m values of 0.57 and 0.23. It is quite obvious that high m value does impede localised thinning at the pole.

A number of analytical developments have been reported to predict the thinning of this kind of geometry in superplastic forming [27, 38, 40, 41, 42]. It has been shown

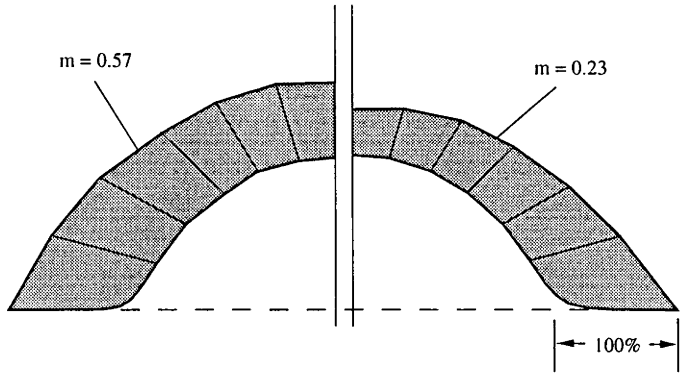

Figure 2-9: Experimentally observed thickness profiles for a hemispherical dome formed from materials with two different m values [5].

that the initial stress state differences and the corresponding strain rate differences along the meridian of forming dome lead to a predictable thinning gradient over the hemisphere. The magnitude of the thinning gradient of hemisphere geometry, however, is determined by the strain rate sensitivity m and the height to which the part is formed.

Rectangular Shapes

The factors that dominate the thinning characteristics in rectangular parts, as well as other shapes, are the same as those of the spherical dome-shaped parts discussed in the above section. The rectangular shape is a specific geometry that determines the initial stress state gradients, and different geometries will expect to develop different stress states in the forming parts.

The rectangular shape is the one that is commonly used in many parts or sections of parts, and it has been studied by both experimental and analytical methods [44, 43].

For a long rectangular shape, there is a plane-stress state throughout the width of the sheet. If the die entry radius does not cause a significant stress concentration, the sheet will not experience an initial stress state gradient. Thus the case is similar to that of the tensile test, in which only thickness variations or material inhomogeneities lead to local stress differences causing localised thinning. Experimental results for such a forming show that only a little thinning gradient is seen for rectangular shapes (figure 2-10) in comparison with that of hemispherical parts.

However interactions with the tooling, more or less, do cause local stress variations

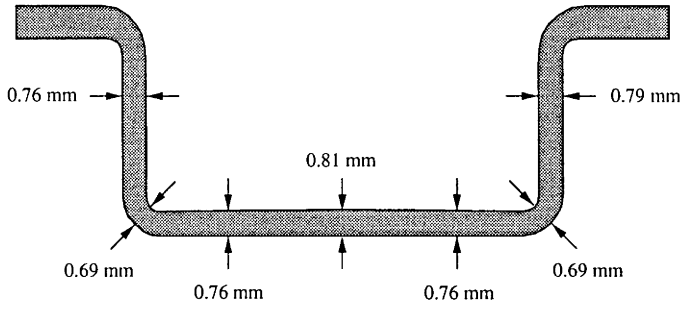

Figure 2-10: Thinning development in a 1.37 mm (0.054 in.) thick superplastic formed Ti-6Al-4V part with a rectangular cross section and semi-infinite length. Formed at $870°C$ $(1600°F)$ using a boron nitride lubricant, the sheet required 20 minutes to fabricate at an average strain rate of 5.8×10^{-4}.

that can lead to thinning gradients as shown in figure 2-10. This effect can be considered as two different types of action of different areas of the die – the die surface at the bottom and sidewall, and the die entry radius [4].

Ignoring the die entry effects, the die surface, of which the friction is non-zero, restricts deformation in the forming sheet where contact has been made. When the sheet makes contact with the die wall surface, the deformation in that contact area is restricted, and thinning is developed in the non-contact areas.

This type of thinning is readily predicted analytically, if it is assumed that the sheet sticks to the die surface after contact is made, by using an incremental method [45]. Results of this model show that there are a variety of thinning variations corresponding to various width and depth ratios of the rectangular shape, and the narrow and deep parts develop great amount of localised thinning. In this specific case, the thickness profiles can be predicted quite well without referring to the strain rate sensitivity m. This is the result of the dominant effect of the die friction coupled with the uniform initial stress state. If the interfacial friction is reduced, the thinning gradient will be reduced in the sidewall and the bottom areas, because continued deformation after contacting with die is possible.

The die entry radius causes a local stress concentration in the sheet, which then creates a stress state gradient, and this can lead to a localised thinning, especially if the ratio of die radius to sheet thickness is small and if the surface is lubricated.

The source of the stress concentration is the action of the back pressure exerted by the die radius on the forming sheet and the gas pressure on the opposite side of the

sheet. The pressure by the die radius has been shown to be [45]

$$P_r = \frac{\sigma_w h}{R_l} \tag{2.12}$$

where P_r is the pressure of the die entry radius, σ_w is the in-sheet stress in the width direction, h is the sheet thickness, and R_l is the die entry radius. P_r and the applied gas pressure g develop an average through-thickness stress σ_h of

$$\sigma_h = \frac{g + P_r}{2} \tag{2.13}$$

The magnitude of σ_w depends on the local friction coefficient μ and the position on the radius, so that the effective stress will vary around the die entry radius. A detailed analytical model is available in reference [45], but it has been shown that local stress increases in this area, causing a tendency toward local thinning. If the friction is sufficiently low, the initially thinned section can continue to thin after die contact is made. Therefore, significant localised thinning can occur, and even rupture may take place if the conditions are sufficiently severe.

Thinning over the die entry radius is the result of stress gradients, therefore once again the strain rate sensitivity m is an important parameter in determining the extent of thinning development. The strain rate variations result in corresponding variations in the m value during the respective forming process. In the circumstance where lubricant is used, high m values lead to reduced tendency toward local thinning around the die entry radius.

Thinning Control

Superplastically formed parts typically experience a great amount of elongation during the process, leading to potentially large thickness variations. Therefore it is important to control the thickness variations to meet the tolerance requirements. The methods used in thinning control include:

- Processing of the superplastic material to achieve a high m value;
- Use of surface lubrication;
- Use of thermo-forming methods to control the localised deformation;
- Modification of the die or part design to minimise local stress concentrations;
- Optimisation of the sheet thickness profile to achieve desired final thickness profile and

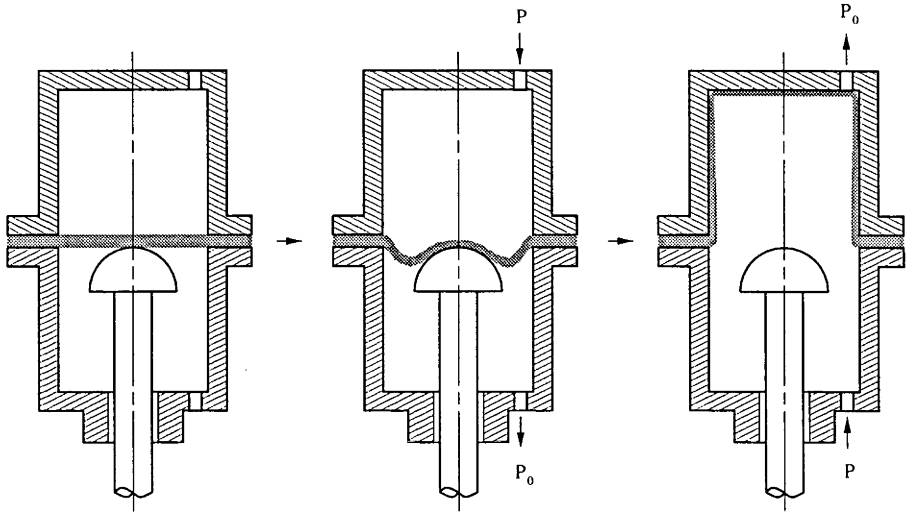

Figure 2-11: Apparatus for thermo-forming superplastic sheet materials using a convex die member to control thinning in forming of a hat configuration.

- Application of pressure with a profiled curve to control strain rate to a value corresponding to a high m value.

The raw sheet material is generally obtained from the commercial supplier by which the material superplastic properties are under the control. The effect of lubrication has been discussed briefly in the previous sections along with the effect of the die entry radius which may be increased to minimise the thickness gradients.

The thermo-forming method has been shown to offer effective techniques that can control the thinning gradients in single pocketed deep-drawn parts [27]. With these methods, a movable tool is usually used to contact the forming sheet before the finished shape is produced, causing the local friction to minimise deformation in some locations while free-forming sections continue to deform.

Apart from those methods discussed before, another application of thermo-forming techniques is demonstrated using apparatuses such as those shown in figure 2-11 and 2-12 [27].

For the convex upward die, the deformation is restricted in the centre of the sheet and concentrated at the outer area, resulting in a strain and thickness profile in which the top centre is thicker than the adjacent areas. This thickness profile can be substantially modified by the use of a concave upward die. In this case, the superplastic diaphragm is formed down into the concave die by gas pressure, and the die is slowly withdrawn until it reaches the bottom. The diaphragm is then formed into the upper

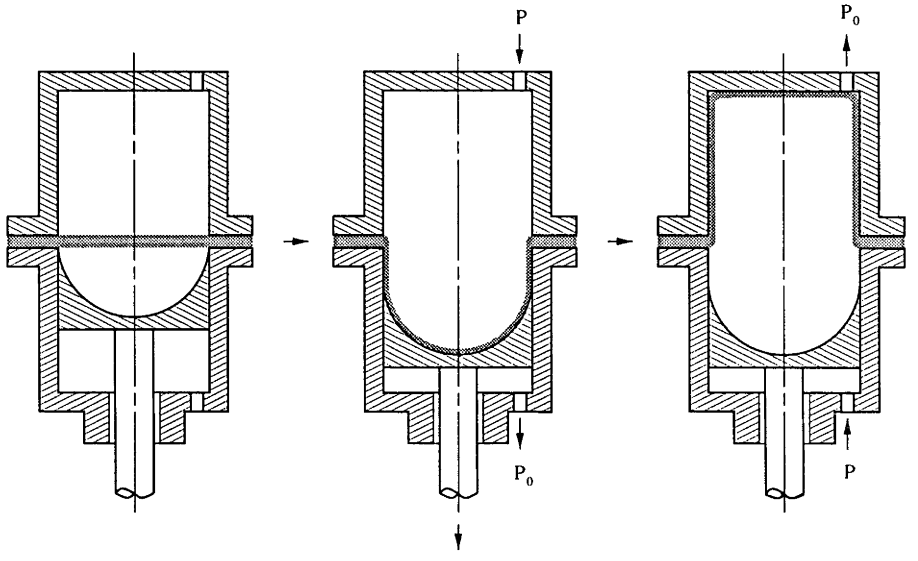

Figure 2-12: Apparatus for thermo-forming superplastic sheet materials using a concave die member to control thinning in forming of a hat configuration.

cylindrical chamber in the same manner as that of the previous figure. The final profile is considerably more uniform across the top of the part.

Pressure profiling is recognised as an efficient method in thinning control. In superplastic forming with constant pressure, the strain rate varies during the process, leading to the variation of strain rate sensitivity m. Therefore thinning uniformity also varies. The resulting strain rate variation for a spherical dome part configuration has been shown to be as much as three orders of magnitude [46] where, for a typical superplastic alloy, the m value can vary from a maximum to a value less than 0.2. The consequence of forming a part under these conditions is that excessive thinning or even rupture during forming is likely. To improve this condition and to maintain the strain rate at a constant level corresponding to a high m value, it is natural that a variable forming pressure would be required. Such pressure profiles have been established analytically for the spherical dome [46, 47] and rectangular [45] configurations. However with numerous commercial finite analysis packages, numerical results of pressure profiles, which are more reliable and precise, can be readily achieved for most of the configurations.

The pressure profiles for spherical dome and the rectangular part are illustrated in figure 2-13 and 2-14. It is typical that the pressure initially rises rapidly, followed by decrease. The rapid initial rise is due to a rapid decrease in the radius of curvature with little change in thickness, and the subsequent decrease is the result of thinning

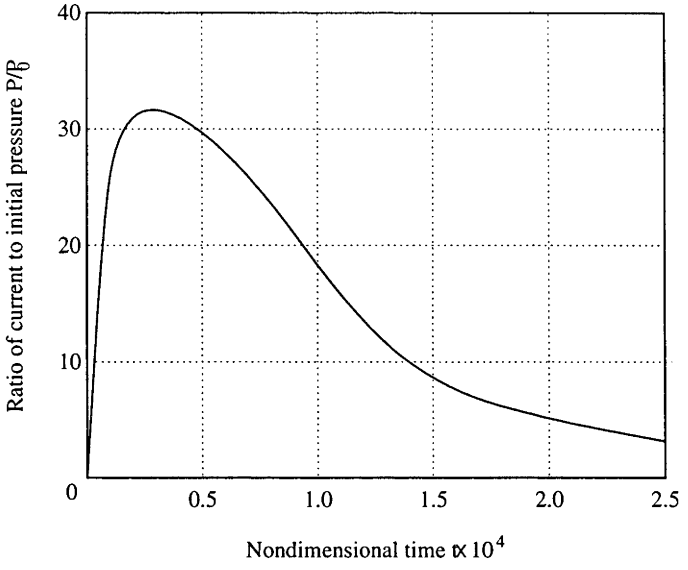

Figure 2-13: Ratio of current to initial pressure as a function of a time parameter for forming a spherical configuration under constant strain rate condition [3].

that is more rapid at this stage than the change in radius of curvature [4].

The use of thickness-profiled sheet was suggested to control the thickness in the final part [40]. This concept considers that the initial thickness variations can be used to offset the subsequent variations resulting from the stress state and part geometry effects on the thinning. Those areas that will thin excessively in the forming of constant thickness sheet, can be compensated by more materials so that more uniform thickness profile of final part could be obtained.

J. Cheng proposed a procedure to design the blank thickness profile for blowing a flat sheet into a hemispherical dome of prescribed thickness [12]. An analytical solution describing the thickness variation during a free inflation process is first derived, neglecting both bending and transverse shear effects. However large errors exist due to the simplified assumptions made in the analytical solution. A modified approach based on the numerical solution is an alternative approach. The analytical equation is replaced by a FE model. The thickness variation of the inflated sheet is generated from curve-fitting the finite element solutions.

No reported work has been found which describes the use of numerical FE models in the optimisation of initial sheet thickness.

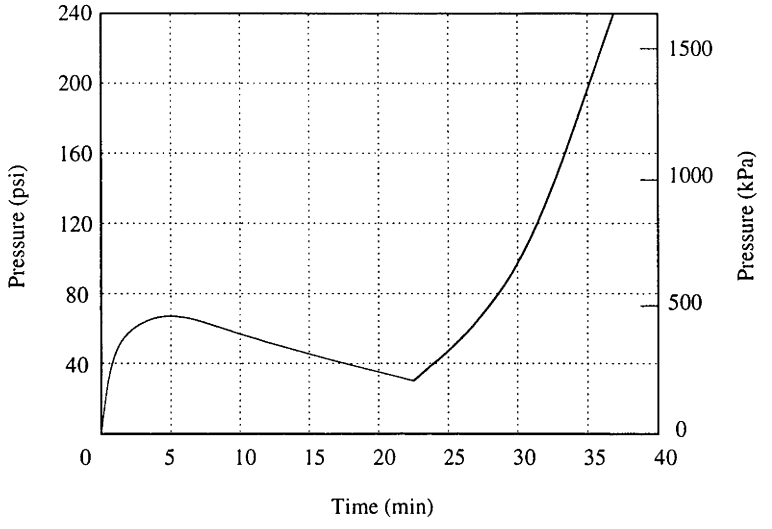

Figure 2-14: Analytically predicted pressure profile for forming a rectangular part under constant strain rate condition. The section of the rectangular part is square [3].

2.2.3 Cavitation and Cavitation Control

During the superplastic deformation, many superplastic alloys tend to form voids or cavities at intergranular locations. This is termed cavitation [4]. Cavitation can lead to the degradation of strength and other design properties. However it can be dealt with by either establishing reduced design properties, or utilising a back pressure technique to control cavitation.

Cavitation is typically a function of strain (figure 2-15). It can be seen that the absolute amount of cavitation in terms of the volume fraction is not large but depends on the strain imposed. The application of the back pressure concept imposes a hydrostatic pressure on the sheet during forming, and if this pressure is of the order of the flow stress, cavitation can be reduced or completely suppressed. In practice, the back pressure is achieved by imposing a pressure on the back side of the forming sheet to oppose the forming pressure and by sustaining this pressure during the forming cycle. However the same forming rates can be achieved if the differential of forming pressure and back pressure is the same.

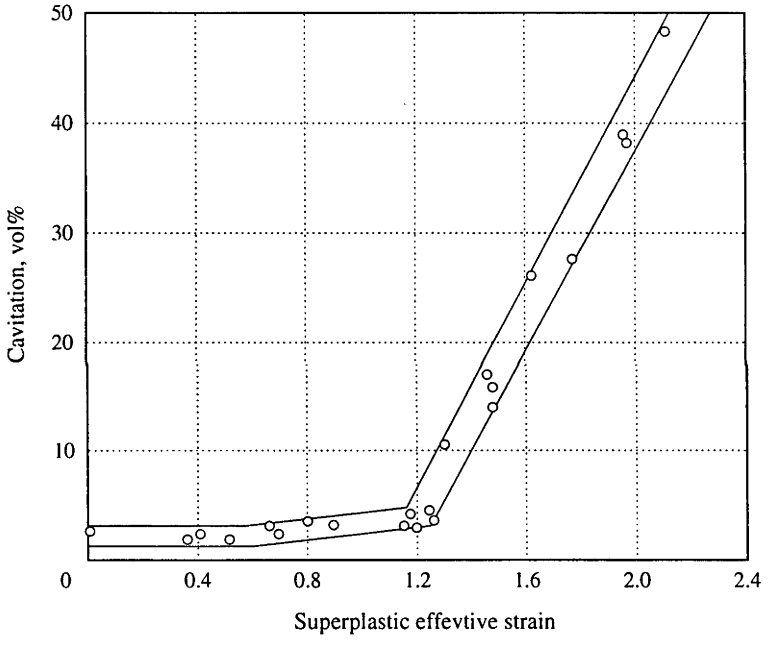

Figure 2-15: Development of cavitation with uniaxial tensile strain in a 7475 aluminium alloy specimen of 0.8 cm^2 cross-sectional area deformed at 516^oC under a constant strain rate of 2×10^{-4} /s.

Chapter 3

Finite Element Modelling

Finite element (FE) modelling of the SPF process is a key component of this project. A short review of the finite element analysis (FEA) is presented as an overview of this technique for later discussion. All the finite element analyses (FEA) carried out during this project are performed by using the general purpose implicit finite element code, ABAQUS/Standard. There has been work in which explicit dynamic based codes have been used to model the superplastic forming process. Therefore, both ABAQUS/Standard and ABAQUS/Explicit schemes of finite element analysis are discussed briefly in this chapter. Three superplastic forming models are used in the superplastic forming simulations which are described.

3.1 Introduction

Finite element analysis was first developed in 1943 by R. Courant [48], who utilised the Ritz method of numerical analysis and minimisation of variational calculus to obtain approximate solutions to vibration systems. Shortly thereafter, a paper [49] published in 1956 by M. J. Turner, R. W. Clough, H. C. Martin, and L. J. Topp established a broader definition of numerical analysis. The paper centred on the "stiffness and deflection of complex structures".

Be the early 1970's, the FEA technique had been developed to a point where it could be used for the analyses of many structural and dynamic problems. However, applications were restricted to the aerospace, automotive, nuclear and defence industries. This was primarily due to the need of powerful computing facilities required by

FEA system which at that time were restricted to such industries.

The period since the 1970's has seen a rapid increase in computing power with a corresponding decrease in cost. This has now brought the FEA technique within the reach of all users.

3.2 Implicit and Explicit Dynamic Analyses

Dynamic integration operators are broadly characterised as implicit or explicit[50].

Explicit schemes, as used in ABAQUS/Explicit, obtain values for dynamic quantities at $t + \Delta t$ based entirely on available values at time t. The central difference operator, which is the most commonly used explicit operator for stress analysis applications, is only conditionally stable, the stability limit being approximately equal to the time for an elastic wave to cross the smallest element dimension in the model.

Implicit schemes remove this upper bound on time step size by solving for dynamic quantities at time $t+\Delta t$ based not only on values at t, but also on these same quantities at $t + \Delta t$. But because they are implicit, nonlinear equations must be solved. In structural problems implicit integration schemes usually give acceptable solutions with time steps typically one or two orders of magnitude larger than the stability limit of simple explicit schemes, but the response prediction will deteriorate as the time step size increases relative to the period of typical modes of response. Thus, the relative economy of the two techniques of integration depends on the stability limit of the explicit scheme, on the ease with which the nonlinear equations can be solved for the implicit operator, on the relative size of time increments that can provide acceptable accuracy with the implicit scheme compared to the stability limit of the explicit scheme, and on the size of the model.

3.2.1 Implicit Dynamic Analysis

A body force at a point, $\mathbf{f}$, may be written as an externally prescribed body force, $\mathbf{F}$, and a d'Alembert force [50]:

$$\mathbf{f} = \mathbf{F} - \rho\,\ddot{\mathbf{u}} \tag{3.1}$$

where ρ is the current density of the material at this point and $\mathbf{u}$ is the displacement of the point. Then the body force term in the virtual work equation has the form [50]

$$\int_V \mathbf{f} \cdot \delta\mathbf{v}\, dV = \int_V \mathbf{F} \cdot \delta\mathbf{v}\, dV - \int_V \rho\, \ddot{\mathbf{u}} \cdot \delta\mathbf{v}\, dV. \tag{3.2}$$

The d'Alembert term may be written more conveniently in terms of the reference volume and reference density, ρ_0, as

$$\int_{V_0} \rho_0\, \ddot{\mathbf{u}} \cdot \delta\mathbf{v}\, dV_0$$

where $\ddot{\mathbf{u}}$ is the acceleration field. When implicit integration is used the equilibrium equations are written at the end of a time step (at time $t + \Delta t$), and $\ddot{\mathbf{u}}$ is calculated from the time integration operator. The interpolator approximates the displacement at a point as

$$\mathbf{u} = \mathbf{N}^N u^N, \tag{3.3}$$

where $\mathbf{N}^N$, $N = 1, 2 \cdots$ up to the total number of variables in the problem, is a set of N vector interpolation functions, and u^N, $N = 1, 2 \cdots$, is a set of nodal displacement. So

$$\ddot{\mathbf{u}} = \mathbf{N}^N \ddot{u}^N, \tag{3.4}$$

provided that $\mathbf{N}^N$ is not displacement dependent. This is the case for most of the elements in ABAQUS. With this interpolation assumption, the d'Alembert force term is

$$-\left(\int_{V_0} \rho_0\, \mathbf{N}^N \cdot \mathbf{N}^M\, dV_0\right) \ddot{u}^M,$$

that is, the consistent mass matrix times the accelerations of the nodal variables. Then the finite element approximation to equilibrium is

$$M^{NM} \ddot{u}^M + I^N - P^N = 0, \tag{3.5}$$

where

$$M^{NM} = \int_{V_0} \rho_0\, \mathbf{N}^N \cdot \mathbf{N}^M\, dV_0 \tag{3.6}$$

is the consistent mass matrix,

$$I^N = \int_{V_0} \boldsymbol{\beta}^N : \boldsymbol{\sigma}\, dV_0 \tag{3.7}$$

is the internal force vector, and

$$P^N = \int_S \mathbf{N}^N \cdot \mathbf{t}\, dS + \int_V \mathbf{N}^N \cdot \mathbf{F}\, dV \tag{3.8}$$

is the external force vector. In this context the terms "matrix" and "vector" refer to matrices and vectors in the space of the nodal variables u^N.

3.2.2 Explicit Dynamic Analysis

The explicit dynamic analysis procedure in ABAQUS/Explicit is based upon the implementation of an explicit integration rule together with the used of diagonal or "lumped" element mass matrices. The equations of motion for the body are integrated using the explicit central difference integration rule

$$\dot{u}^N_{(i+\frac{1}{2})} = \dot{u}^N_{(i-\frac{1}{2})} + \frac{\Delta t_{(i+1)} + \Delta t_{(i)}}{2} \ddot{u}^N_{(i)}, \tag{3.9}$$

$$u^N_{(i+1)} = u^N_{(i)} + \Delta t_{(i+1)} \dot{u}^N_{(i+\frac{1}{2})}, \tag{3.10}$$

where u^N is a degree of freedom (a displacement or rotation component) and the subscript (i) refers to the increment number in an explicit dynamics step [51]. The central difference integration operator is explicit in that the kinematic state may be advanced using known values of $\dot{u}^N_{(i-\frac{1}{2})}$ and $\ddot{u}^N_{(i)}$ from the previous increment. The explicit integration rule is quite simple, but by itself does not provide the computational efficiency associated with the explicit dynamics procedure. The key to the computational efficiency of the explicit procedure is the use of diagonal element mass matrices, because the accelerations at the beginning of the increment may be computed by

$$\ddot{u}^N_{(i)} = (M^{NM})^{-1}(P^M_{(i)} - I^M_{(i)}), \tag{3.11}$$

where M^{NM} is the diagonal lumped mass matrix, P^M is the applied load vector, and I^M is the internal force vector. The explicit procedure requires no iterations and no tangent stiffness matrix.

The explicit procedure integrates through time by using many small time increments. The central difference operator is conditionally stable and the stability limit for the operator (with no damping) is given in terms of the highest eigenvalue in the system as

$$\Delta t <= \frac{2}{\omega_{max}}. \tag{3.12}$$

In ABAQUS/Explicit a small amount of damping is introduced to control high frequency oscillations. With damping, the stable time increment is given by

$$\Delta t \leq \frac{2}{\omega_{max}}(\sqrt{1+\xi^2}-\xi), \tag{3.13}$$

where ξ is the fraction of critical damping in the highest mode. Contrary to usual engineering intuition, introducing damping to the solution reduces the stable time increment.

The computer time involved in running a simulation using explicit time integration with a given mesh is directly proportional to the time period of the event. The stability limit can be rewritten (ignoring damping) in the form

$$\Delta t \leq \min\left(L^{el}\sqrt{\frac{\rho}{\lambda+2\mu}}\right), \tag{3.14}$$

where the minimum is taken over all elements in the mesh, L^{el} is a characteristic length associated with an element, ρ is the density of the material in the element, and λ and μ are the effective Lamé's constants for the material in the element. For linear, non-isotropic elastic materials, this stability limit is further scaled down by a factor which is the square root of the ratio of the effective material stiffness to the maximum material stiffness in one particular direction. Since this effectively means that the time increment can be no larger than the time required to propagate a stress wave across an element, the computer time involved in running a quasi-static analysis is very large, since the cost of the simulation is directly proportional to the number of time increments required, $n = T/\Delta t$ if Δt remains constant, where T is the time period of the event being simulated. Thus,

$$n \approx T \max\left(\frac{1}{L^{el}}\sqrt{\frac{\lambda+2\mu}{\rho}}\right). \tag{3.15}$$

To reduce n, a possible way is to speed up the simulation compared to the time of the actual process — that is, one can artificially reduce the time period of the event, T. This will introduce two possible errors. If the simulation speed is increased too much, the increased inertia forces will change the predicted response. Then not choosing a too large speed–up is the only way to avoid this error. The other error is that some aspects of the problem, other than inertia forces, may be rate dependent. This implies that one cannot change the actual time period of the event being modelled. But we

can see a simple equivalent – artificially increasing the material density ρ by a factor f^2 reduces n to n/f, just like decreasing T to T/f. This concept, called *mass scaling*, reduces the ratio of the event time to the time for wave propagation across an element while leaving the event time fixed, thus allowing treatment of rate dependent material and other behaviours, while having exactly the same effect on inertia forces as speeding up the time of simulation. *Mass scaling* is attractive because it allows people to treat rate dependent problems, such as superplastic forming . But it is not universally valid, and taking it too far will change the solution.

3.2.3 About ABAQUS

ABAQUS is a commercial finite element analysis software, and basically provides two kinds of FEA scheme, ABAQUS/Standard and ABAQUS/Explicit.

ABAQUS/Standard is a general-purpose, production-oriented finite element program designed specifically for advanced analysis applications. A wide variety of problems can be addressed with the available modelling tools. For example, option `*CREEP STRAIN RATE CONTROL` is specially for the control of creep strain rate in superplastic forming analysis.

ABAQUS/Standard uses an implicit analysis scheme, which provides a variety of time-domain and frequency-domain analysis procedures. These procedures are divided into two classes: " general analyses " in which the response may be linear or nonlinear, and " linear perturbation analyses " in which linear response is computed about a general, possibly nonlinear, base state. A single simulation can include multiple analysis types. The general analyses include:

- Static stress/displacement analysis,
- Viscoelastic/viscoplastic response,
- Transient dynamic stress/displacement analysis,
- Transient or steady-state heat transfer analysis,
- Transient or steady-state mass diffusion analysis,
- Coupled problems;

and linear perturbation analyses include:

- Static stress/displacement analysis,
- Dynamic stress/displacement analysis.

ABAQUS/Explicit is a finite element program designed specifically for advanced, nonlinear continuum and structural analysis needs. The program addresses highly nonlinear transient dynamic phenomena and certain nonlinear quasi-static simulations. ABAQUS/Explicit uses explicit time integration for time stepping and includes the following types of analyses:

- Explicit dynamic response with or without adiabatic heating effects.
- Annealing for multi-step forming simulations.

Both ABAQUS/Standard and ABAQUS/Explicit are designed to run on computers ranging from desktop systems running Windows NT or UNIX to departmental servers and supercomputers.

3.3 FE Modelling in Superplastic Forming

Superplastic sheet forming is a process involving large deformation, large strain, nonlinear material behaviour and, usually, deformation dependent boundary conditions [52]. Consequently the numerical analysis of such a highly nonlinear process involves formidable computational problems. Fortunately the superplastic behaviour of metals is characterised by the dependence of the flow stress upon the rate of strain which allows the material to be described as rigid-viscoplastic. Recognition of the similarities between this type of material response and that of a non-Newtonian viscous fluid have enables a "viscous flow" formulation to be developed which circumvents many of the complexities associated with a large deformation solid mechanics based approach.

Two solution procedures, implicit and explicit, have been used to simulate thin sheet SPF processes.

The implicit formulation is derived directly from the simulation of non-Newtonian viscous flows where such an approach is particularly well-suited. It has been shown that the implicit procedure is efficient for 2-D cases. But some problems occur with 3-D structures where it may be difficult to perfectly simulate the contacts using such a formulation [52, 53, 54, 55]. However, most research published in SPF modelling have employed this formulation to predict the final thickness profile of the formed superplastic sheet and to determine the pressure cycle. Bonnet et. al. [52, 56, 55] adopted the thin shell kinematics equations to represent the superplastic phenomenon

of both 2-D and 3-D cases. They built an implicit model which involved flat 3-node membrane elements, and solved for the nodal velocities. Bellet et. al. [57, 58] attempted a membrane isoparametric element approach for the simulation of 3-D cases and a plane-strain element formulation for 2-D circumstance. Rama and Chandra [59, 60] based their work on a continuum element formulation which allowed them to consider the effects of bending and shear stresses in addition to those of membrane. Their study has been validated by pan-forming simulations.

As the size of the meshed model increases, the explicit method provides a major advantage in computational time in comparison to implicit method, whereas its major drawback is that the stable time increment is small in comparison to the actual process. However, for rate dependent issues like SPF, this could be overcome by *mass scaling* which has been specified in section 3.2.2.

3.4 Superplastic Forming Modelling

3.4.1 Geometry and Model

There are several Geometric models being simulated, including 2-dimensional hemispherical dome and flat pan, and 3-dimensional rectangular box.

Hemispherical Dome

The hemispherical dome is one of the simplest shapes in superplastic forming process. Its axisymmetric feature enables 3-D result to be obtained using a 2-D model, and can save considerable computational time. In the later experiments carried out, a dome-shape component with smaller dimensions is also adopted to verify the simulation results.

Figure 3-1 shows the geometry of the hemispherical dome die. The radius of the dome die is 508 mm (20 in), and the fillet radius is 101.6 mm (4 in). The die is modelled as a rigid surface and completely fixed in all degrees of freedom.

Half of the initial disc blank is modelled by 23 nodes and 22 shell elements of type SAX1[1] (see figure 3-2), with radius of 711.2 mm (28 in). Node 1 is in the central of the whole blank and can only move in direction 2 (up and down), whereas node 23 is at the

[1]SAX1 is 2–node thin or thick axisymmetric shell element.

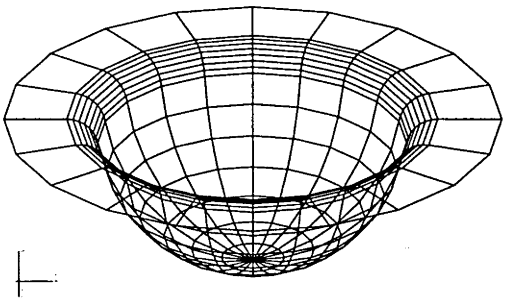

Figure 3-1: The geometry of hemispherical dome die.

edge of the blank and clamped on the flange of the die completely. The first element next to the centre point is element 1, and the last element near the edge is element 22.

Flat Pan

The flat pan is similar to the hemispherical dome, but the corner of the pan gives more complexity. 3-D results also can be achieved by 2-D model. The die of the flat pan is shown in figure 3-3. The pan is 1016 mm (40 in) wide and 508 mm (20 in) deep with fillet radius of 101.6 mm (4 in).

Also, half of the disc blank is modelled by 23 nodes and 22 SAX1 elements (see figure 3-4). Node 1 is located in the central of the blank and moves up and down in direction 2 only. Node 23 is at the edge of the blank and completely fixed in all directions. Element 1 is the one next to the centre point, whereas element 22 is the last one close to the edge.

Rectangular Box

The rectangular box is one of the examples provided by ABAQUS/Standard Example Problems Manual [61]. Its geometry is more intricate than those of hemispherical dome and flat pan, and more closely resembles practical components. A quarter of the box

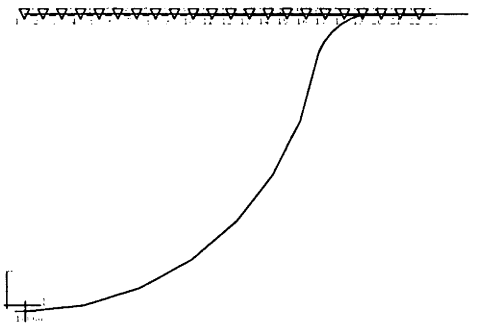

Figure 3-2: Initial position of blank with respect to dome die.

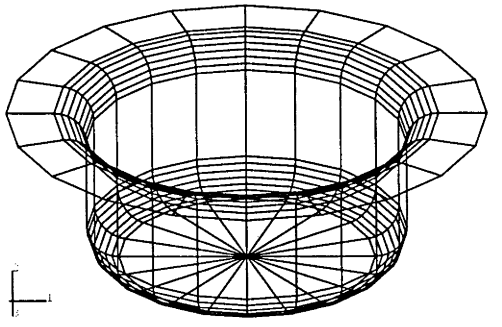

Figure 3-3: The geometry of flat pan die.

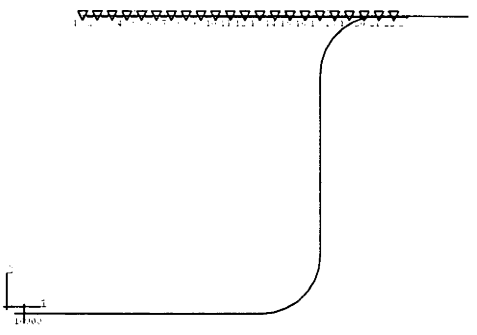

Figure 3-4: Initial position of blank with respect to pan die.

is modelled in order to save computational time.

The final dimensions of the rectangular box are 1321 mm (52 in) long by 813 mm (32 in) wide by 508 mm (20 in) deep with a 50.8 mm (2 in) flange around it. All fillet radii are 101.6 mm (4 in). The female die is modelled as a rigid body, as shown in figure 3-5, and meshed with rigid R3D3[2] element.

A quarter of the blank is modelled using 704 membrane elements of type M3D4R[3], shown in figure 3-6. Two kinds of boundary conditions are applied in the model. The two edges, which coincide with two axes of the box, can only go up and down in direction 2, and the other two are fixed completely.

One thing should be pointed out is that, in order to avoid having points "fall off" the rigid surface during the course of the analysis, more than half or a quarter of the die has been modelled in these three models. In other words, the rigid surface is extended far enough so that contacting nodes will not slide off the master surface.

3.4.2 Material

The material of all the blanks in these three models are assumed to be elastic-viscoplastic, and the properties roughly represent the 2004 (Al-6Cu-0.4Zr-0.3Mg-0.2Si-0.1Ge) based

[2]R3D3 is three-dimensional, 3-node, rigid element.

[3]M3D4R is three-dimensional, 4-node membrane element with reduced integration.

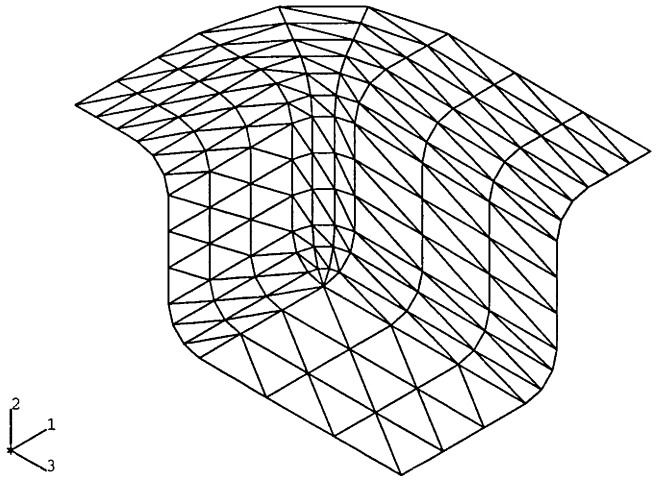

Figure 3-5: The geometry of rectangular box die.

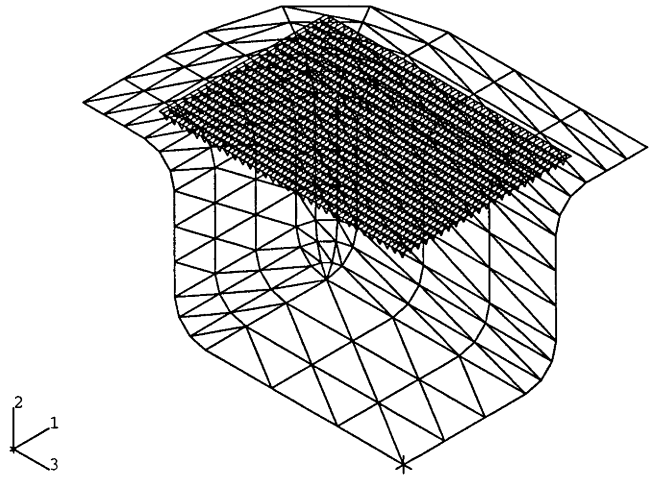

Figure 3-6: Initial position of blank with respect to rectangular box die.

Mechanical property	Value
Temperature range (^oC)	400 - 480
Strain rate range (/s)	0.0005 - 0.01
Stress range (Mpa)	5 - 35
Elongation (%)	400 - 1800
Yield strength (MPa)	220
Young's modulus (GPa)	71
Poisson's ratio	0.34

Table 3.1: Mechanical properties of Supral 100.

commercial superplastic aluminium alloy Supral 100.

Supral 100 is dynamically recrystallising alloy in which the grain size is a function of the initial strain rate during superplastic forming, but is typically 3 to 6 micrometres. The material is warm rolled at 300 ^oC to almost 90% reduction and recovery/recrystallisation is prevented primarily by a dispersion of ZrAl3 particles occupying about 5% by volume at 5 to 10 nm diameter and to a lesser extent by Mg2Si particles.

Optimum superplastic forming temperature of supral 100 is 460 ^oC, but the material can be formed anywhere from 400 to 480 ^oC. The optimum strain rates for deformation are between 10^{-3} to $10^{-2}/s$ and thus forming times are substantially shorter than for other superplastic alloys. Elongations of 1500% are possible but the Supral alloys do cavitate (10% by volume is possible but at commercial strains (300%) 1% is more typical) usually where there are large undissolved primary ZrAl3 particles or undissolved CuAl2. The mechanical properties for Supral 100 are shown in table 3.1.

The optimum strain rate used in ABAQUS analyses is supposed to be 0.02 /sec, and the flow stress σ_f is assumed to depend on the plastic strain rate $\dot{\varepsilon}$ according to

$$\sigma_f = A(\dot{\varepsilon})^{\frac{1}{2}} \tag{3.16}$$

where A is 179.2 MPa (26.0×10^3 lb/in^2), and the time is in seconds.

3.4.3 Loading and Controls

Two analyses can be performed by ABAQUS in the three models, one is with constant loading pressure , and another one is with a pressure schedule automatically adjusted to achieve a maximum strain rate, which is supposed to be 0.02/sec for Supral 100.

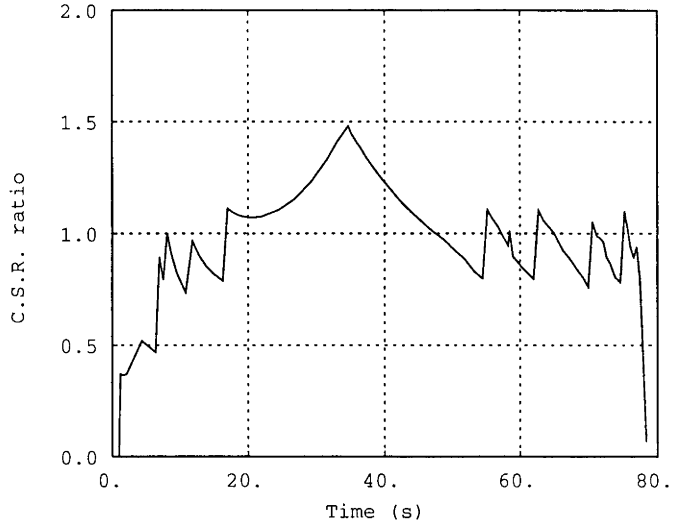

Figure 3-7: History of ratio between maximum creep strain rate and target strain rate.

In the constant load case the pre-stressed blank is, in all these three models, subjected to a rapidly applied external pressure of 68.8 kPa (10 lb/in^2) which is then held constant for a certain period of time, until the component has been formed. In the second case the pre-stressed blank is subjected to a rapidly applied external pressure of 1.38 kPa (0.2 lb/in^2). The pressure schedule is then chosen by ABAQUS.

Constant loading is handy to achieve and control, so it is adopted in the later experiments. But the variation of maximum strain rate of the blank which is undesired, usually, cannot be avoided. Automatic loading fits superplastic forming process very well, and is used in all the simulation works in this project. A history of ratio between maximum creep strain rate and target strain rate of the 3-D box is shown in figure 3-7, and its corresponding automatic loading pressure curve is shown in figure 3-8. They may give readers a general picture about automatic loading control.

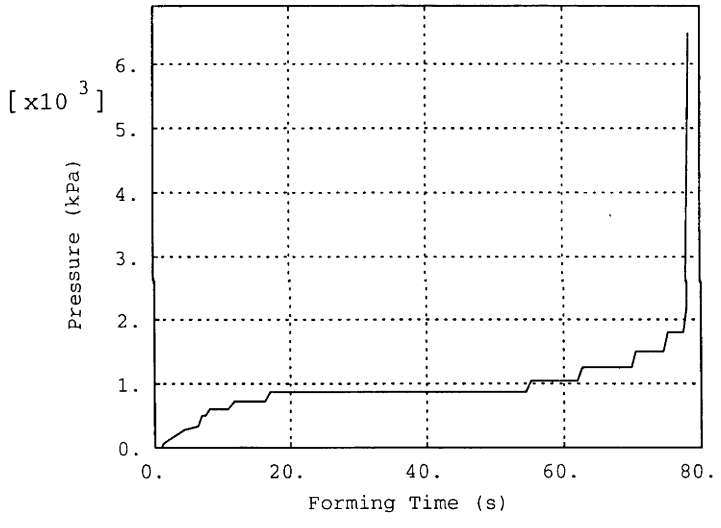

Figure 3-8: Automatic loading pressure for rectangular box (strain rate = 0.02).

Chapter 4

Optimisation Methods

4.1 Introduction

Optimisation can be defined as the science of determining the *best* solution to certain mathematically defined problems, which are often models of physical reality [62]. It is the process by which the optimal solution to a problem, or optimum, is produced [63]. The word *optimum* has come from the Latin word *optimum*, meaning best.

There has been a host of contributions, from Archimedes to the present day, scattered across many disciplines. Many of the earlier ideas, although interesting from a theoretical point of view, were originally of little practical use, as they involved a daunting amount of computational effort. The advent of the computer has helped bring about the unification of optimisation theory into a rapidly growing branch of applied mathematics. The computer provided the means of resolving many of the numerical problems [64].

Optimisation involves the study of optimality criteria for problems, the determination of algorithmic methods of solution, the study of the structure of such methods, and computer experimentation with methods both under trial conditions and on real life problems.

The commonly used methods of optimisation include:

- *Dichotomous* search
- *Fibonacci* search
- *Golden section*

for optimisation with single variable, and

- *Gradient* search and *Newton*'s method
- Contour tangent elimination
- *Simplex* method
- *Davidon*'s method

for multi-variable optimisation.

There are two things which should be stated here. First, minimisation and maximisation are essentially same processes. For any maximisation problem like

$$\max f(x),$$

it is always able to transfer it into minimisation as

$$\min(-f(x)).$$

So only minimisation is discussed in this chapter. Secondly, as D. J. Wilde pointed out [65], multimodal problems having more than one peak have not been studied with any success so far. In other words, all the search methods presented in this chapter only apply for unimodal circumstance. Anyone confronted with such a problem must at present try to isolate the various peaks and explore each of them individually [65]. Fortunately from the author's experiences in optimising the sheet thickness in SPF, there is only one solution of thickness where the criteria converges to. Therefore all the search schemes posed following are applicable.

4.2 Unimodality

4.2.1 Unimodality

In order to present the search method clearly, it is necessary to define unimodality first.

In single variable problem, unimodality is obvious. Functions y of a single variable x which, roughly speaking, have only one valley in the interval to be explored. All the functions pictured in figure 4-1 have this property, which is called *unimodality*. Notice that a unimodal function does not have to be smooth as in figure 4-1(a), or even continuous as in figure 4-1(b); it can be broken, discontinuous, and even undefined in certain intervals as in figure 4-1(c). Thus, the unimodality assumption, not really very restrictive, holds in a large number of practical search problems.

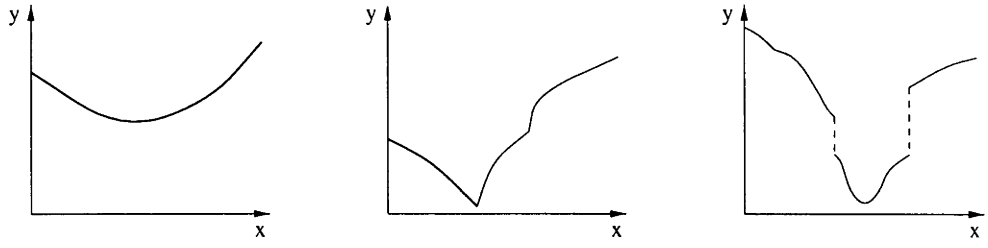

(a) Concave (b) Continuous (c) Arbitrary

Figure 4-1: Unimodal functions.

To define unimodality mathematically, let y^* represent the desired but unknown minimum value of y, and let x^* be the value of x for which this minimum is attained. That is,

$$y^* \equiv \min_x y(x) \tag{4.1}$$

$$y(x^*) \equiv y^* \tag{4.2}$$

Consider two experiments x_1 and x_2, with $x_1 < x_2$, and their outcomes are y_1 and y_2 respectively. Then y is unimodal, if $x_2 < x^*$ implies that $y_1 < y_2$, and if $x_1 > x^*$ implies that $y_1 > y_2$. In other words, if the points are both on the same side of the optimum, then the one nearer the optimum gives the higher value of y. This definition is strong enough for single variable problem to build a measure of search effectiveness, without being so restrictive as to exclude many practical functions behaving discontinuously.

For the problems with multi variables, unimodality is not so simple. The criterion y is a function of the coordinates of the corresponding experiment $\mathbf{x}$, which can all be expressed in terms of the parameter λ as

$$y(x_1(\lambda), x_2(\lambda), \cdots, x_k(\lambda)) = y(\lambda) \tag{4.3}$$

where $0 \leq \lambda \leq 1$. Since y depends only on the single parameter λ, the concept of unimodality of one-dimensional problem can be borrowed. Let m represent the minimum value attained by y as λ passes through its range, and λ^* designate the value of λ at which y equals m. That is

$$m \equiv \min_{0 \leq \lambda \leq 1} y(\lambda) \tag{4.4}$$

and

$$y(\lambda^*) \equiv m \tag{4.5}$$

Let λ_1 and λ_2 (with $\lambda_1 < \lambda_2$) be any two values of the parameter λ in the unit interval. Then, similarly as single variable situation, y is *unimodal* on the path form **a** to **b** if

$$\lambda_2 < \lambda^* \tag{4.6}$$

implies that

$$y(\lambda_1) < y(\lambda_2) \tag{4.7}$$

and if

$$\lambda^* < \lambda_1 \tag{4.8}$$

implies that

$$y(\lambda_1) > y(\lambda_2) \tag{4.9}$$

It is clear now how to define unimodality for a function of k variables. Let $\mathbf{x}^*$ be the point in the experimental region at which y reaches its minimum value y^*

$$y^* = \min_{\mathbf{x}} y(\mathbf{x}) \tag{4.10}$$

and

$$y(\mathbf{x}^*) \equiv y^* \tag{4.11}$$

Then the function $y(\mathbf{x}^*)$ will be described as *unimodal* if for every pair of points **a** and **b** in the experimental region there exists a path from **a** through $\mathbf{x}^*$ to **b** on which y is unimodal. The surface whose contours are exhibited in figure 4-2(a) is unimodal, whereas the one in figure 4-2(b) is not.

4.2.2 Strong Unimodality

A function will be called *strong unimodal* if the straight line running to the summit at $\mathbf{x}^*$ from any point **a** in the experimental region is a falling path. Figure 4-3 shows two response surfaces, one is strong unimodal and the other not.

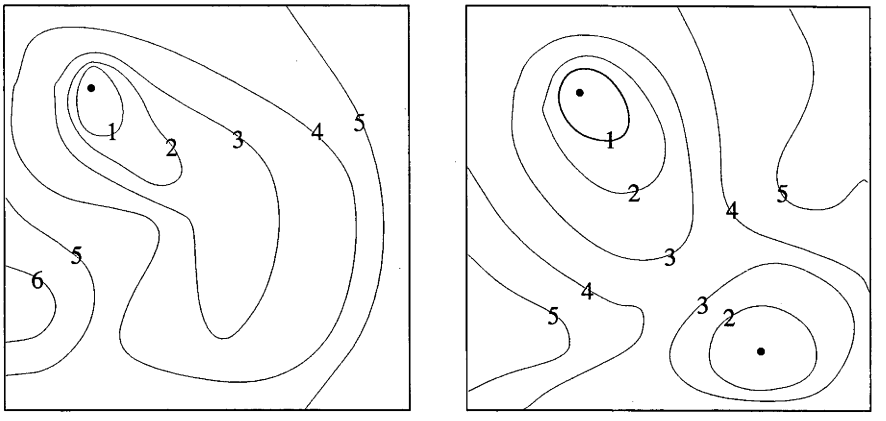

(a) Unimodal function (b) Bimodal function

Figure 4-2: Unimodal and non–unimodal response surfaces.

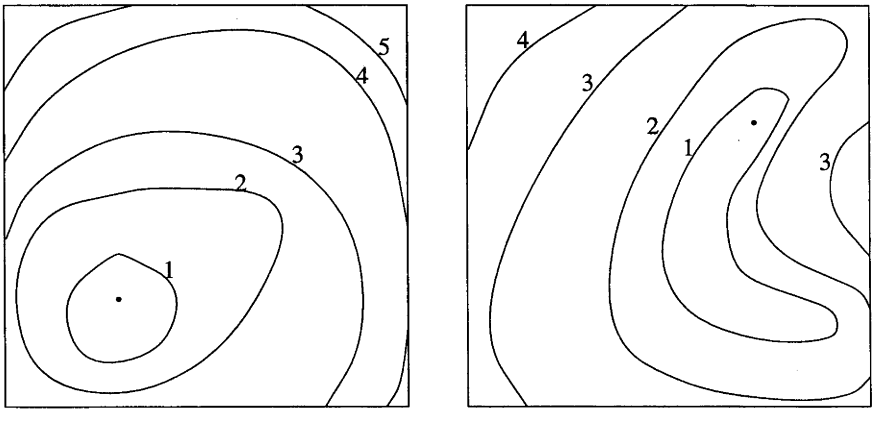

(b) Strong unimodal (a) Unimodal (not strong)

Figure 4-3: Strong unimodal and non–strong unimodal response surfaces.

4.3 Single Variable Optimisation

Simultaneous search and sequential search are two basic search schemes in optimisation. A sequential search allows the investigator to run his experiments one after the other, using information from earlier experiments to decide where to locate later ones, whereas in simultaneous search all experiments must be run at the same time. Naturally, sequential search schemes are much more effective than simultaneous plans and their flexibility pays off heavily, even more than one might imagine. Often one can avoid an inefficient simultaneous search simply by changing one's point of view.

4.3.1 *Dichotomous* Search

The idea of *dichotomous* search is, in the interval of uncertainty $[a, b]$, where $L_1 = a - b$, conducting two experiment at the points

$$x_- = \frac{1}{2}L_1 - \frac{\epsilon}{2} \tag{4.12}$$

$$x_+ = \frac{1}{2}L_1 + \frac{\epsilon}{2} \tag{4.13}$$

where ϵ is minimum permissible separation between experiments (figure 4-4). Then function evaluation $f(x_-) > f(x_+)$ means that the interval $[x_-, b]$ contains the peak; likewise $f(x_-) < f(x_+)$[1] indicates that the minimum locates in $[a, x_+]$. Suppose the first circumstance happens, therefore segment $[x_-, b]$ turns out to be the new interval. The same procedure can be repeated until a satisfactory result is arrived at.

Generally after n experiments (n must be even of course) one can locate the minimum within an interval at length $\frac{1}{2}^{\frac{n}{2}} + (1 - \frac{1}{2}^{\frac{n}{2}})\epsilon$ [65]. Thus the effectiveness of this *dichotomous* search grows exponentially with n. Comparing this to a simultaneous search, in order to reduce to an interval of uncertainty to 1% of its original length would, neglecting ϵ, require 198 simultaneous experiments — a task that could be accomplished after fourteen *dichotomous* trials (table 4.1)

4.3.2 *Fibonacci* Search

When one wants to locate the minimum as accurately as possible, i.e. with the shortest possible interval of uncertainty, but can only afford n experiments, *Fibonacci* search

[1] In extreme circumstance $f(x_-) = f(x_+)$ could happen in theory, but hardly happens in practice. It can therefore be neglected in all the following searches.

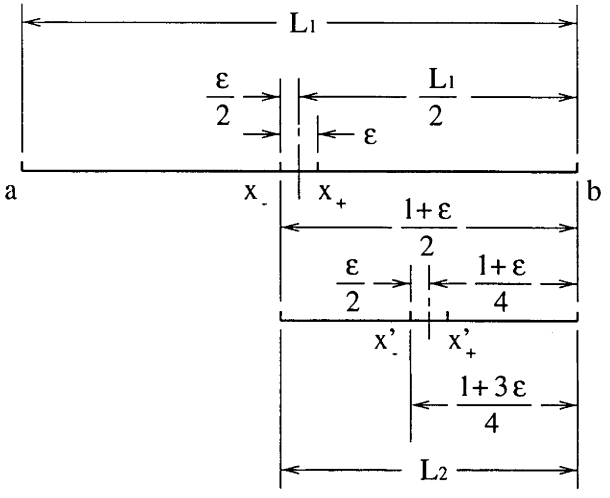

Figure 4-4: Dichotomous search with two experiments.

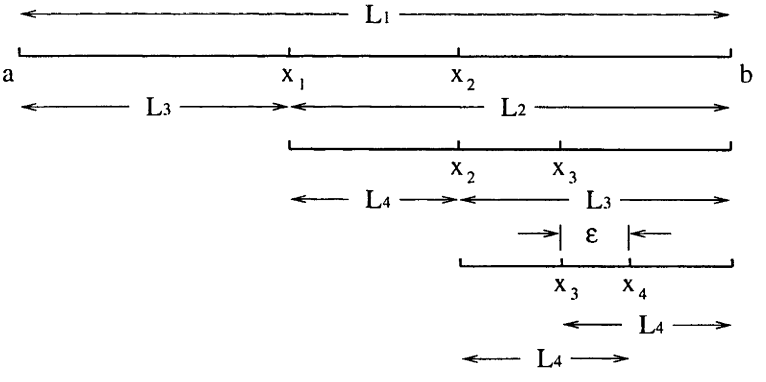

Figure 4-5: *Fibonacci* search with four experiments.

appears to be the best choice.

In order to have general formula for *Fibonacci* search, let us introduce the sequence of numbers F_k, defined as

$$F_0 = F_1 = 1 \tag{4.14}$$

$$F_k = F_{k-1} + F_{k-2} \qquad k = 2, 3, \cdots \tag{4.15}$$

F_k is called the kth *Fibonacci* number.

To start a *Fibonacci* search, the point of the first experiment x_1 is placed L_2 units from one end [2] of the original interval $[a, b]$ whose length is L_1 (figure 4-5), and

[2]It does not matter which end because the second point is placed L_2 units from the other end by the symmetrical rule.

$$L_2 = \frac{F_{n-1}}{F_n} L_1 + \frac{(-1)^n}{F_n} \epsilon, \tag{4.16}$$

where n is number of experiment involved in the search, and ϵ is the minimum permissible separation between experiments.

One then places the second point x_2 within the interval being searching symmetrically with respect to the point x_1. By comparing the function value $f(x_1)$ and $f(x_2)$, part of the interval can be eliminated. Suppose $f(x_2) < f(x_1)$, interval $[a, x_1]$ is therefore removed and $[x_1, b]$ left (figure 4-5). Again one finds the third point x_3 within the new interval symmetrically to point x_2, compares $f(x_2)$ and $f(x_3)$, and removes the invalid interval. By keeping doing this procedure, the interval will, after n experiments, reduce to

$$L_n = \frac{1}{F_n} + \epsilon. \tag{4.17}$$

By this *Fibonacci* search technique an interval of uncertainty can be reduced to less than 1% of its original length after only eleven sequential experiments (table 4.1). As pointed out earlier, this same reduction would require fourteen dichotomous experiments or 198 simultaneous trials.

4.3.3 *Golden Section*

Golden section search is nearly as effective as *Fibonacci* method, but independent of the number of experiments available, in other words it does not require the experiment number n to be specified at the outset.

Before introducing the *Golden section* search, let us define

$$\tau = \frac{1 + \sqrt{5}}{2} = 1.618033989 \cdots \tag{4.18}$$

τ is called *Golden section* ratio.

To perform *Golden section* search, a similar procedure as *Fibonacci* method would be followed. The first point is placed at a distance L_1/τ from one end, where L_1 is the original interval of uncertainty; the second point the same distance from the other end. The results of the two experiments will determine which segment is to be explored further. As usual, this remaining segment will contain one of the previous

Number of experiments	*Dichotomous* search L_0/L_n	*Fibonacci* search L_0/L_n	*Golden section* $(1.62)^{n-1}$
0	1	1	
1	1	1	1
2	2	2	1.62
3	2	3	2.62
4	4	5	4.24
5	4	8	6.85
6	8	13	11.09
7	8	21	17.94
8	16	34	29.0
9	16	55	47.0
10	32	89	76.0
11	32	144	123
12	64	233	199
13	64	377	322
14	128	610	521
15	128	987	843
16	256	1597	1364
17	256	2584	2207
18	512	4181	3570
19	512	6765	5778
20	1024	10946	9349
21	1024	17711	15127
22	2048	28657	24476
23	2048	46368	39602
24	4096	75025	64078
25	4096	121393	103680
26	8192		
27	8192		
28	16384		
29	16384		
30	32768		

Table 4.1: Reduction ratios for various sequential search plans.

trials, and to continue the search one merely places the next experiment symmetrically in the interval. Once begun, this process may be continued as long as desired. After n experiments the interval L_n remaining is given by

$$L_n = \frac{1}{\tau^{n-1}} L_1 \tag{4.19}$$

4.4 Multi-variable Optimisation

4.4.1 Multidimensional Generalisation

It is important to generalise the multivariable problems before specifying the search plans.

Let $y(x_1, x_2, \cdots, x_k)$ be a function of k independent variables, $\mathbf{x}_0 = (x_{01}, x_{02}, \cdots, x_{0k})$ be the original experiment point, and y_0 be its outcome. Define the deviations

$$\Delta x_j = x_j - x_{0j} \qquad \text{for } j = 1, 2, \cdots, k \tag{4.20}$$

$$\Delta y = y - y_0 \tag{4.21}$$

The linear approximation for Δy at $\mathbf{x}_0$ is

$$\Delta y = \sum_{j=1}^{k} \frac{\partial y}{\partial x_j} \Delta x_j \tag{4.22}$$

To evaluate the coefficients $\dfrac{\partial y}{\partial x_j}$ one must perform k experiments (excluding $\mathbf{x}_0$) and solve the k simultaneous equations

$$\Delta y_i = \sum_{j=1}^{k} \Delta x_{ij} \frac{\partial y}{\partial x_j} \qquad \text{for } i = 1, 2, \cdots, k \tag{4.23}$$

for the constants $\dfrac{\partial y}{\partial x_j}$, since the Δx_{ij} and Δy_i are given for each experiment. These computations can be simplified by choosing $\Delta x_{ij} = 0$ for all $i \neq j$, in which case equation 4.23 gives simply

$$\frac{\partial y}{\partial x_j} = \frac{\Delta y_j}{\Delta x_{jj}} \qquad \text{for } j = 1, 2, \cdots, k \tag{4.24}$$

Equation 4.24 indicates that, to evaluate $\dfrac{\partial y}{\partial x_j}$ of the jth variable, one just needs to do a experiment at point $(x_1, x_2, \cdots, x_j + \Delta x_j, \cdots, x_n)$.

Once the $\frac{\partial y}{\partial x_j}$ are known one can state that the combinations of Δx_j giving decreased y must satisfy the inequality

$$\sum_{j=1}^{k} \frac{\partial y}{\partial x_j} \Delta x_j < 0 \tag{4.25}$$

Geometrically speaking, if one considers the $k+1$ dimensional space of y and the $\mathbf{x}$, equation 4.22 describes the k dimensional hyperplane tangent to the response surface at $\mathbf{x}_0$.

4.4.2 Direct Search and Descent Techniques

Direct search and descent techniques are two main classes for optimisation with multivariable.

Direct search techniques are most suitable for simple problems involving a relatively small number of variables [66]. Generally speaking however it is less efficient than descent techniques. Direct search requires only objective function evaluations and does not use partial derivatives. In addition, information accumulated in earlier iterations may be used by some direct search techniques.

Descent techniques differ from direct search methods in a number of respects. One of these is that the amount of information carried over from iteration to iteration. Some of the direct search methods do not use information from previous iterations, while most of the descent techniques carry over and use this information. Furthermore, new directions of descent are generated in each iteration. Most direct search methods, on the other hand, just proceed to probe the objective function along a set of predetermined direction. The descent iterations usually involve more computational work in the evaluation of the gradients than the direct search methods which require only evaluations of the objective function $f(\mathbf{x})$. Also descent search methods may involve, in addition, the evaluation of first and possibly higher order derivatives of the objective function. However as a result of more computation, each step of descent process normally yields considerable improvement of the objective function. Thus, overall computational efficiency of descent techniques is usually high in comparison to that of direct search, and convergence to a solution in relatively fewer steps can be expected.

There are a number of direct search methods, such as:

- pattern search (the method of Hooke and Jeeves [67]),

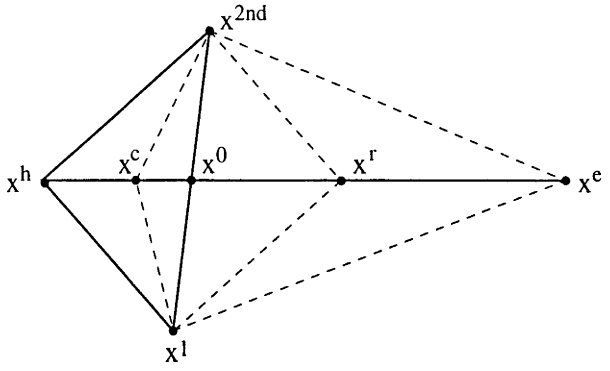

Figure 4-6: The reflection, contraction and expansion operations in *simplex* method.

- the method of rotating coordinates,
- the *simplex* method (by Spendley, Hext and Himsworth [68]) and improved *simplex* method (by Nelder and Mead [69]), and etc.

There are more methods under the category of descent techniques, such as:

- steepest descent (first-order gradient),
- *Newton's* method (second-order gradient),
- least squares,
- conjugate *gradient* methods,
- variable metric methods, and etc.

In the following paragraphs, the *simplex* method (improved by Nelder and Mead) and *gradient* search (first-order gradient) are selected to discuss briefly.

Simplex Method

The *simplex* method is based on the comparison of the objective function values at the $n+1$ vertices of a general simplex in n dimensions and moving this simplex towards the optimum point [69]. There are three basic operations in the movement: reflection, contraction and expansion (figure 4-6).

To minimise the function, $f(\mathbf{x}_i)$ is evaluated at each vertex. Supposing $\mathbf{x}^h$ is the vertex corresponding to the highest value of the objective function:

$$f(\mathbf{x}^h) = \max_i(\mathbf{x}^i) \qquad i = 1, 2, \cdots, n+1; \tag{4.26}$$

$\mathbf{x}^{2nd}$, $\mathbf{x}^{3rd}$, $\cdots$ are the vertices with the second, the third, $\cdots$ highest values of $f(\mathbf{x})$; $\mathbf{x}^l$ is vertex with the lowest value of $f(\mathbf{x})$; and $\mathbf{x}^0$ is the centroid of all $\mathbf{x}^i$ except $i = h$,

given by:

$$\mathbf{x}^0 = \frac{1}{n} \sum_{i=1, i \neq h}^{n+1} \mathbf{x}^i \tag{4.27}$$

Since $f(\mathbf{x}^h)$ is the worst (highest) value the method tries to make a move as far away as possible from $\mathbf{x}^h$ by reflecting the vertex in the centroid of the opposite side of the simplex, that is:

$$\mathbf{x}^r = (1+\alpha)\mathbf{x}^0 - \alpha \mathbf{x}^h \qquad \alpha > 0 \tag{4.28}$$

A new simplex $\mathbf{x}^r$, $\mathbf{x}^{2nd}$, $\mathbf{x}^{3rd}$, $\cdots$, $\mathbf{x}^r$ has been formed. New value $f(\mathbf{x}^r)$ raises two possible cases: $f(\mathbf{x}^r) < f(\mathbf{x}^h)$ or $f(\mathbf{x}^r) > f(\mathbf{x}^h)$. In the first case $f(\mathbf{x}^r)$ is not the worst vertex, and the same reflection procedure can be applied to the new simplex. If, on the other hand, $f(\mathbf{x}^r) > f(\mathbf{x}^h)$ then $\mathbf{x}^r$ gives the worst value of the new simplex so reapplying the reflection method to the new simplex would just reproduce the old one. To get out of this loop a new strategy is employed. The second largest vertex of the new simplex, $\mathbf{x}^{2nd}$, is chosen and the reflection procedure is implemented on it. If the strategy is a success the method proceeds as before. If the strategy fails the vertex $\mathbf{x}^{3rd}$ is selected for reflection. The cycle then continues similarly: if a success is obtained return to the original method, if not try the next largest vertex.

In some circumstances expansion and contraction can be applied so that either the simplex can move faster or the uncertain area can be reduced by shrinking the simplex.

- If $f(\mathbf{x}^r) < f(\mathbf{x}^l)$, expansion operation can be inserted to accelerate the movement of the simplex. As $f(\mathbf{x}^r)$ becomes the lowest vertex, the direction of the reflection is desired and further improvement of the function value may be achieved by expansion, that is

  $$\mathbf{x}^e = \gamma \mathbf{x}^r + (1-\gamma)\mathbf{x}^0 \qquad \gamma > 1 \tag{4.29}$$

  The expansion is successful if $f(\mathbf{x}^e) < f(\mathbf{x}^l)$, and in this case $\mathbf{x}^h$ is replaces by $\mathbf{x}^e$. In the case of failure $\mathbf{x}^h$ is replaces by $\mathbf{x}^r$.

- If $f(\mathbf{x}^r) > f(\mathbf{x}^{2nd})$ and $f(\mathbf{x}^h) > f(\mathbf{x}^{2nd})$, $\mathbf{x}^h$ is replaced by $\mathbf{x}^r$, and contraction move is then employed, that is

  $$\mathbf{x}^c = \beta \mathbf{x}^h + (1-\beta)\mathbf{x}^0 \qquad 1 > \beta > 0 \tag{4.30}$$

Therefore by comparing $\mathbf{x}^c$ and $\mathbf{x}^h$ two possible cases arise . In the case that $f(\mathbf{x}^h) > f(\mathbf{x}^c)$, then $\mathbf{x}^h$ is replaced by $\mathbf{x}^c$ and the procedure is restarted. Otherwise if $f(\mathbf{x}^h) \leq f(\mathbf{x}^c)$, the current simplex is shrunk about the point $\mathbf{x}^l$ as:

$$\mathbf{x}^i_{new} = \frac{1}{2}(\mathbf{x}^i + \mathbf{x}^l) \qquad i = 1, 2, \cdots, n+1 \tag{4.31}$$

and restart the procedure.

Nelder and Mead [69] found that useful values for the coefficients α, γ and β were:

$$\begin{cases} \alpha = 1 \\ \gamma = 2 \\ \beta = 0.5 \end{cases} \tag{4.32}$$

After giving an initial estimate of the minimum $\mathbf{x}^1 = (x_1, x_2, \cdots, x_n)$, an initial simplex is formed using two auxiliary values

$$\begin{cases} p_n = \dfrac{\sqrt{n+1} - 1 + n}{n\sqrt{2}} S \\ q_n = \dfrac{\sqrt{n+1} - 1}{n\sqrt{2}} S \end{cases} \tag{4.33}$$

where S is a scaling factor. The $n+1$ vertices of a regular simplex with edge of length S are given by

$$\begin{cases} \mathbf{x}^1 & = (x_1, x_2, x_3, \cdots, x_n)^T \\ \mathbf{x}^2 & = (p_n + x_1, q_n + x_2, q_n + x_3, \cdots, q_n + x_n)^T \\ \mathbf{x}^3 & = (q_n + x_1, p_n + x_2, q_n + x_3, \cdots, q_n + x_n)^T \\ \vdots & \\ \mathbf{x}^{n+1} & = (q_n + x_1, q_n + x_2, q_n + x_3, \cdots, p_n + x_n)^T \end{cases} \tag{4.34}$$

This construction of the initial simplex assures that its vertices span the full n dimensional space [66].

The simplex method has a wide application as it does not make any assumption about the objective function except that the function is continuous. It may be useful when the locations of minima are needed with a limited accuracy and the final rapid convergence is not essential. However some disadvantages of the method do exist. There

is a possibility that the simplex may collapse into a subspace and therefore no solution in the desired space of all variable will be found. It can also shrink drastically into a steep valley and stop the procedure prematurely. Computational efficiency depends on the choice of the coefficients α, γ and β, and the size of the initial simplex. Criteria for an optimal choice of these values are not known, although $\alpha = 1$, $\gamma = 2$ and $\beta = 0.5$ can be recommended [66].

Gradient Search

The gradient search techniques involve iterations which consist essentially of three parts. First, a direction of descent $\mathbf{s}^k$ in the kth iteration is found, then a descent step-length λ^k is determined, and finally the descent step $\mathbf{x}^{k+1} = \mathbf{x}^k - \lambda^k \mathbf{s}^k$ is performed.

The descent direction is an n dimensional vector

$$\mathbf{s} = (s_1\ s_2\ \cdots\ s_n)^T \tag{4.35}$$

$$= \left(\frac{\partial y}{\partial x_1}\ \frac{\partial y}{\partial x_2}\ \cdots\ \frac{\partial y}{\partial x_n}\right)^T \tag{4.36}$$

If it is not possible to evaluate partial differentiations mathematically, experimental evaluation can be achieved by

$$\frac{\partial y}{\partial x_i} = \frac{f(x_i + \Delta x_i) - f(x_i)}{\Delta x_i} \qquad (\Delta {x_i}^2 > \epsilon^2) \tag{4.37}$$

where ϵ is minimal permissible separation between experiments. Equation 4.37 indicates that, to evaluate the partial differentiation in the ith dimension, one can conduct one more experiment at point $x_i + \Delta x_i$ which must be outside the range $[x_i - \epsilon,\ x_i + \epsilon]$, as far as Δx_i is sufficiently small.

As pointed in section 4.4.1, functions of k independent variables have the linear approximation

$$\Delta y = \sum_{i=1}^{k} \frac{\partial y}{\partial x_i} \Delta x_i \qquad \text{for } i = 1,\ 2,\ \cdots,\ k \tag{4.38}$$

Introducing an arbitrary scalar λ, the gradient line is represented by

$$\Delta x_i = \frac{\partial y}{\partial x_i} \lambda \qquad \text{for } i = 1,\ 2,\ \cdots,\ k \tag{4.39}$$

Equation 4.38 and 4.39 together give

$$\Delta y = \lambda \sum_{i=1}^{k} \left(\frac{\partial y}{\partial x_i}\right)^2 \tag{4.40}$$

Hence Δy changes with λ.

Notice that equation 4.40 only contains one variable λ, single variable search plans preceded in section 4.3 can be adopted to achieve λ_k^*, which gives minimum along the descent direction in the kth iteration. That is

$$f(\mathbf{x}^k - \lambda_k^* \mathbf{s}^k) = \min_{\lambda} f(\mathbf{x}^k - \lambda \mathbf{s}^k) \tag{4.41}$$

where λ_k^* is so called *optimal descent step* [66].

Alternatively one also can employ *non-optimal descent step.* A descent step λ_K is said to be a non-optimal steps if it satisfies

$$f(\mathbf{x}^k - \lambda_K \mathbf{s}^k) \leq f(\mathbf{x}^k) \tag{4.42}$$

instead of equation 4.41. That means, any value of λ could be adopted, as far as function value at the new point is no larger than the previous one. Of course in practice one alway chooses a value of λ according to his/her experiences, so that the function converges rapidly.

Contrary to one's intuition, non-optimal descent steps will lead to better efficiency in the most cases. This is correct in the sense that usually more computation would be required to find optimal λ_k^* satisfying 4.41 than just 4.42. Jacoby pointed out that "Experience indicates, however, that overall computational efficiency is frequently improved when non-optimal steps are used" [66].

By now it is easy to calculate the new point by

$$\mathbf{x}^{k+1} = \mathbf{x}^k - \lambda^k \mathbf{s}^k \tag{4.43}$$

Positive values of λ generate the line of steepest descent. Conversely, negative values of λ give the line of steepest ascent.

Repeating the above procedure enables one to approach the true minimum continuously. In theory one most likely gets closer and closer to the concave point infinitely, but will not be able to "arrive" the real point. However in practice, it will be considered that the minimum is "found" when the point is located in an acceptable small area to the experimenter.

Figure 4-7 (a) shows the convergent track by gradient search with optimal λ_k^*, i.e. for every single iteration step one always optimises λ so that it gives the minimal output y. Gradient search convergent track with non-optimal λ_K is shown in figure 4-7 (b).

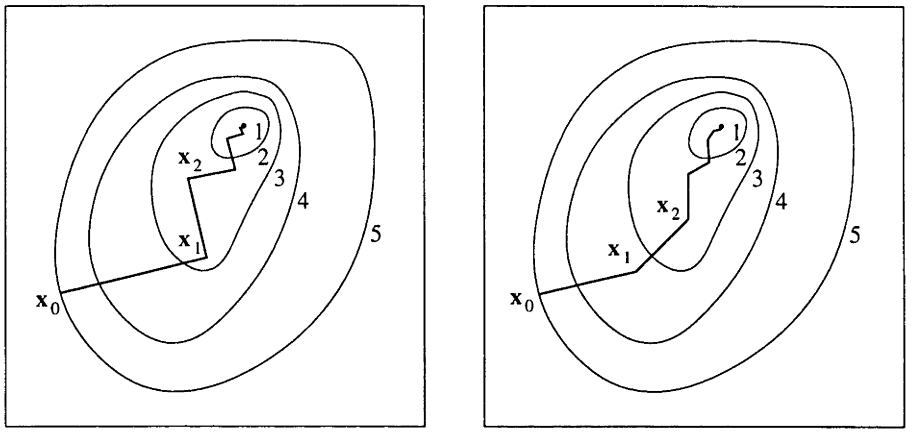

(a) Gradient search with optimal λ (b) Gradient search with constant λ

Figure 4-7: Gradient search tracks.

The gradient search technique is a simple technique involving relatively little computational work per step. Each iteration is independent of the previous ones. The method may converge to a solution even from a poor initial approximation for either strong or non-strong unimodal problems. Unfortunately the method has several shortcomings. Very short steps may be produced, accompanied by sharp changes in the gradient. This is frequently referred to as "zigzagging" and implies slow convergence and low computational efficiency in spite of the small amount of work per step. Furthermore, the gradient search depends on the variable scaling. It has been known that this method could be unstable with respect to small perturbations which may be rounding error, inaccuracy and etc. in the experiments.

However, due to its attractive features, gradient search technique is adopted in this thesis as one of the methods for the SPF thickness optimisation.

Chapter 5

Sheet Optimisation

The goal of this chapter is to optimise the initial sheet thickness profile in superplastic forming process so that a desired final product thickness profile can be achieved. FEA simulations of a hemispherical dome, flat pan and 3-D box, whose geometric models and material properties have been described in section 3.4, are implemented by using ABAQUS/Standard.

5.1 Introduction

Superplastic forming is a very non-linear process. The relation between the thickness profiles of the sheet and its formed component is very complex, especially for the components with complicated geometric shapes. The basic mathematic model for a particular geometry, however, could be

$$\mathbf{t} = f(\mathbf{T}), \tag{5.1}$$

where $\mathbf{t}$ is the component thickness profile after forming, and $\mathbf{T}$ is the sheet thickness profile before forming.

J. Cheng has proposed an analytical procedure to design the initial sheet thickness profile [12], as mentioned in section 2.2.2. However the difficulty of this kind of method on obtaining analytical solution for those components with complex geometries, limits its applicable areas. Therefore a trial-and-error approach has to be employed in order to solve practical problems.

The trial-and-error method is essentially an optimisation process in which one can

apply some strategies to approach the best point. Therefore after defining a proper criteria, optimisation methods can be employed.

5.2 Optimisation Criteria

The original thickness profile of a section is a continuous curve. However it is represented by a series of values at discrete nodes with prescribed intervals in FE model. This operation makes it possible to treat the SPF as a multi-input/output process, that is:

$$\mathbf{t}(t_1, t_2, \cdots, t_n) = f(\mathbf{T}(T_1, T_2, \cdots, T_n)) \tag{5.2}$$

where $\mathbf{t}(t_1, t_2, \cdots, t_n)$ and $\mathbf{T}(T_1, T_2, \cdots, T_n)$ are the component thickness profile (output) and sheet thickness profile (input) respectively, and n is the total number of the nodes involved in the forming process.

Directly relating inputs to outputs is difficult as there is strong non-linearity. Therefore it is necessary to define a single optimisation criterion Y based on the thickness output $\mathbf{t}$ of all nodes.

There are a number of ways in which the single criterion can be defined by integrating the information of all nodes.

First, one simple way to do it is to choose the largest absolute nodal thickness error as the single criterion, that is

$$Y = max(|t_i - t^*|) \qquad for \quad i = 1, 2, \cdots, n \tag{5.3}$$

where t_i is the ith node thickness of the formed component, and t^* is the required thickness of the component[1]. The biggest difference between component node thicknesses and its target value is employed as the criterion. Other absolute nodal errors will not be beyond the criterion. If the criterion equals *zero*, all node thicknesses of the component should be t^*.

Second, the criterion can be defined as the mean square error of the component thickness:

$$Y = \frac{1}{n}\sum_{i=1}^{n}(t_i - t^*)^2 \tag{5.4}$$

[1]It is assumed here that the target component thickness t^* is all the same for each of the node. For required variant component profile, t_i^* is the target component thickness for the ith node.

If Y is *zero*, all nodes should equal to t^*.

These criterion definition all have their unique characteristics. As the definition by equation 5.4 can give us a relatively clear scope about the nodal errors, it is more suitable for the optimisation. Hence the mean square error will be adopted as the optimisation criterion in the following discussion.

5.3 Gradient Search Method

5.3.1 Implementation of Gradient Search Method

After defining the criteria Y (output), we can apply a gradient search technique to the optimisation of sheet thickness in SPF.

Recall that the gradient search, which has been demonstrated in section 4.4.2, takes the form:

$$\mathbf{T}^{(k+1)} = \mathbf{T}^{(k)} - \lambda^{(k)}\mathbf{s}^{(k)} \tag{5.5}$$

where $\mathbf{T}$ is the sheet thickness, k is the iteration time, λ is the step-length and $\mathbf{s}$ is the descent direction.

Suppose there are n nodes in the sheet model, therefore the descent direction $\mathbf{s}$ is

an n dimensional vector:

$$\begin{aligned}
\mathbf{s} &= \frac{\partial Y}{\partial \mathbf{T}} \\
&= \left[\frac{\partial Y}{\partial T_1} \quad \frac{\partial Y}{\partial T_2} \quad \cdots \quad \frac{\partial Y}{\partial T_n}\right]^T \\
&= \left[\frac{\partial Y}{\partial \mathbf{t}}\frac{\partial \mathbf{t}}{\partial T_1} \quad \frac{\partial Y}{\partial \mathbf{t}}\frac{\partial \mathbf{t}}{\partial T_2} \quad \cdots \quad \frac{\partial Y}{\partial \mathbf{t}}\frac{\partial \mathbf{t}}{\partial T_n}\right]^T \\
&= \begin{bmatrix}
\frac{\partial Y}{\partial t_1}\frac{\partial t_1}{\partial T_1} + \frac{\partial Y}{\partial t_2}\frac{\partial t_2}{\partial T_1} + \cdots + \frac{\partial Y}{\partial t_n}\frac{\partial t_n}{\partial T_1} \\
\frac{\partial Y}{\partial t_1}\frac{\partial t_1}{\partial T_2} + \frac{\partial Y}{\partial t_2}\frac{\partial t_2}{\partial T_2} + \cdots + \frac{\partial Y}{\partial t_n}\frac{\partial t_n}{\partial T_2} \\
\vdots \\
\frac{\partial Y}{\partial t_1}\frac{\partial t_1}{\partial T_n} + \frac{\partial Y}{\partial t_2}\frac{\partial t_2}{\partial T_n} + \cdots + \frac{\partial Y}{\partial t_n}\frac{\partial t_n}{\partial T_n}
\end{bmatrix} \\
&= \begin{bmatrix}
\frac{\partial t_1}{\partial T_1} & \frac{\partial t_2}{\partial T_1} & \cdots & \frac{\partial t_n}{\partial T_1} \\
\frac{\partial t_1}{\partial T_2} & \frac{\partial t_2}{\partial T_2} & \cdots & \frac{\partial t_n}{\partial T_2} \\
\vdots & & & \\
\frac{\partial t_1}{\partial T_n} & \frac{\partial t_2}{\partial T_n} & \cdots & \frac{\partial t_n}{\partial T_n}
\end{bmatrix}
\begin{bmatrix}
\frac{\partial Y}{\partial t_1} \\
\frac{\partial Y}{\partial t_2} \\
\vdots \\
\frac{\partial Y}{\partial t_n}
\end{bmatrix} \\
&= \frac{\partial \mathbf{t}}{\partial \mathbf{T}}\frac{\partial Y}{\partial \mathbf{t}} \\
&= \mathbf{RE}
\end{aligned} \tag{5.6}$$

where $\mathbf{R} = \dfrac{\partial \mathbf{t}}{\partial \mathbf{T}}$ and $\mathbf{E} = \dfrac{\partial Y}{\partial \mathbf{t}}$.

As the explicit relationship between Y and $\mathbf{t}$ has been known from equation 5.4, we can then rewrite the column matrix $\mathbf{E}$ into:

$$\begin{aligned}
\mathbf{E} &= \left[\frac{\partial Y}{\partial t_1} \quad \frac{\partial Y}{\partial t_2} \quad \cdots \quad \frac{\partial Y}{\partial t_n}\right]^T \\
&= \frac{2}{n}\left[t_1 - t^* \quad t_2 - t^* \quad \cdots \quad t_n - t^*\right]^T \\
&= \frac{2}{n}(\mathbf{t} - \mathbf{t}^*)
\end{aligned} \tag{5.7}$$

Matrix $\mathbf{E}$ represents the error of the current component thickness $\mathbf{t}$ with respect to the target component thickness t^*, and $\mathbf{t}$ can be handily achieved by conducting a simulation at the point $\mathbf{T}^{(k)}$ in the kth iteration.

To derive the $n \times n$ matrix $\mathbf{R}$, simulations have to be held as many as n time, as it is impossible to evaluate partial differentiations analytically in this case. Suppose that, in the ith iteration, we change the ith sheet node thickness T_i into $(1+\delta)T_i$, where δ is a number whose absolute value is sufficiently small, and hold all the other node thicknesses, the component thickness will change to:

$$\mathbf{t}|_{(1+\delta)T_i} = \left[t_1|_{(1+\delta)T_i} \quad t_2|_{(1+\delta)T_i} \quad \cdots \quad t_n|_{(1+\delta)T_i}\right] \tag{5.8}$$

therefore the ith row R_i in the matrix $\mathbf{R}$, where R_i is the the partial differentiation of component thickness with respect to the ith node sheet thickness T_i, is:

$$\begin{aligned} R_i &= \frac{\partial \mathbf{t}}{\partial T_i} \\ &= \frac{\mathbf{t}|_{(1+\delta)T_i} - \mathbf{t}}{\delta T_i} \\ &= \left[\frac{t_1|_{(1+\delta)T_i} - t_1}{\delta T_i} \quad \frac{t_2|_{(1+\delta)T_i} - t_2}{\delta T_i} \quad \cdots \quad \frac{t_n|_{(1+\delta)T_i} - t_n}{\delta T_i}\right] \end{aligned} \tag{5.9}$$

After conducting the calculations of the partial differentiations of component thickness with respect to all the n nodal sheet thicknesses, matrix $\mathbf{R}$ can then be obtained.

As discussed in section 4.4.2, the positive values of λ generate the line of steepest descent. Single variable search plans could be applied to achieve an optimal λ^* for every iteration. Although optimised λ^* will lead to the fastest convergence, the process of λ^* optimisation itself involves considerable calculations. Based on this point, λ with constant value will be applied in later optimisation.

With known values of sheet thickness $\mathbf{T}^{(k)}$, constant step length λ and descent direction $\mathbf{s}^{(k)}$, the new sheet thickness $\mathbf{T}^{(k+1)}$ can be obtained by

$$\begin{aligned} \mathbf{T}^{(k+1)} &= \mathbf{T}^{(k)} - \lambda \mathbf{s}^{(k)} \\ &= \mathbf{T}^{(k)} - \lambda \mathbf{R}\mathbf{E} \\ &= \mathbf{T}^{(k)} - \frac{2\lambda}{n}\mathbf{R}(\mathbf{t} - \mathbf{t}^*) \end{aligned} \tag{5.10}$$

As λ has no physical meaning but a scalar, the above equation could be simplified as

$$\mathbf{T}^{(k+1)} = \mathbf{T}^{(k)} - \lambda \mathbf{R}(\mathbf{t} - \mathbf{t}^*) \tag{5.11}$$

The following optimisation of gradient search will be implemented according to equation 5.11.

This process should be repeated until certain criterion requirement is satisfied.

5.3.2 Sheet Thickness Optimisation by Gradient Search Method

The ABAQUS simulations involved in this section were based on the models of hemispherical dome and flat pan, and their geometries and material properties have been specified in section 3.4. In all these simulations, the automatic loading pressure scheme was adopted.

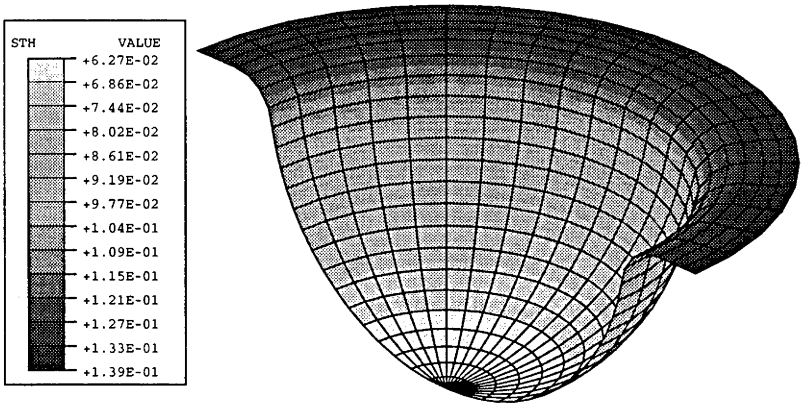

Figure 5-1: The formed dome thickness distribution, using 3.81 mm (0.15 in) thick sheet.

In these two models, the target component thickness t^* was 2.54mm (0.1 inch). The sheet thicknesses, where the simulations started, were of constant thicknesses with which the volume of the sheet was same as the volume of the component with desired thickness. Better initial thicknesses could be applied in practice to save the iteration time. However the goal of this section was to validate the method itself. Little effort was expended in improving the initial sheet thickness.

Hemispherical Dome

The thickness optimisation of the hemispherical dome started with a constant sheet thickness, 3.81 mm (0.15 in), which led a uneven thickness distribution of formed dome (figure 5-1[2]). 15 iterations were repeated using the gradient search algorithm.

The criterion convergence of the dome model with a series values of the step length λ using gradient search method, is shown in figure 5-2 and 5-3. The curves in these two figures start at the same point where the criterion is 0.498 mm^2. This is because the initial conditions were all the same.

In figure 5-2, the convergence tracks of the criterion with different λ are smooth and

[2]The unit of the legend in this figure is inch. And this is applicable to all following such kind of plots by ABAQUS/Post.

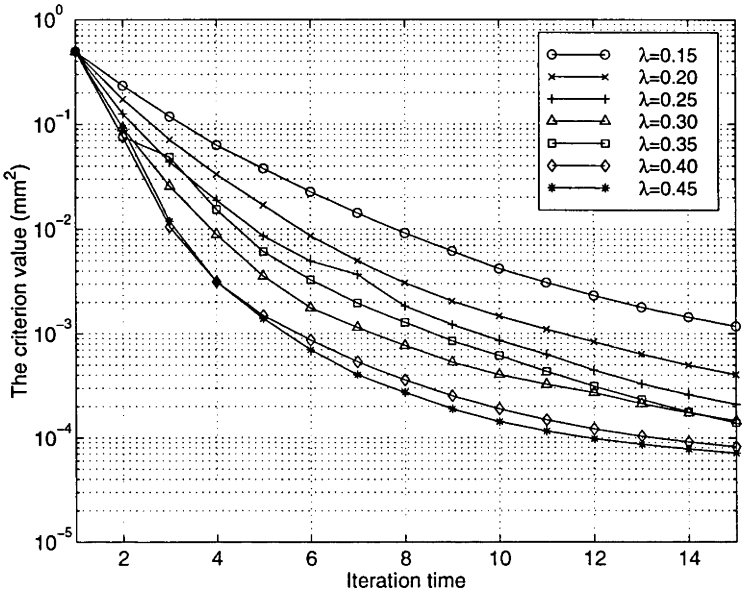

Figure 5-2: Criterion convergences of hemispherical dome model by gradient search method with lower values of λ.

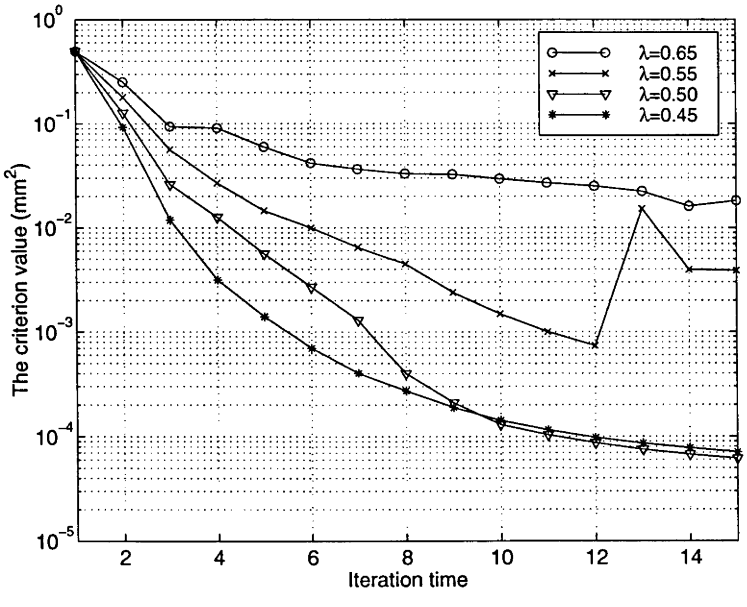

Figure 5-3: Criterion convergence of hemispherical dome model by gradient search method with higher values of λ.

evenly distributed in the semi-logarithmetic coordinate, except the one with $\lambda = 0.25$ whose third difference is not as big as the others. It is easy to find out in this figure that larger value of λ leads to a faster criterion convergence. The best convergence track, which reaches 7.11×10^{-5} mm^2 at the fifteenth iteration, is of $\lambda = 0.45$.

However a different scene is presented in figure 5-3. The criterion convergences follow zigzag routes except the one of $\lambda = 0.45$. The convergent speed decreases greatly when λ increases. Also there is a big "back jump" at the thirteenth iteration when $\lambda = 0.55$, which is not seen in the last figure. The best performance is with $\lambda = 0.45$, although the final point of $\lambda = 0.5$ is slightly lower than that of $\lambda = 0.45$.

The final optimised sheet thickness profiles, when λ is 0.35, 0.40, 0.45 and 0.50, are displayed in figure 5-4. Their correspondent formed dome thickness profiles are exhibited in figure 5-5. The optimised sheet thickness profiles in figure 5-4 are so alike that they almost coincide to each other. These profiles start from about 4.52mm at the central point, node 1, and gradually decrease to about 3.13mm at the edge. There are a convex shape near the central and a concave shape near the edge, due to the boundary conditions applied on both centre and edge nodes. Good consistency is also seen in figure 5-5 where all the dome thickness profiles overlap to each other. All these profiles are located in a small band 2.54 ± 0.02mm. Relatively large fluctuations exist around both the central and edge points, as a result of the odd sheet thicknesses in these area.

Figure 5-6 shows the dome thickness distribution using optimised sheet thickness profile after 15 gradient search iterations ($\lambda = 0.45$).

Figure 5-7 shows how the sheet thickness profile was optimised within the 15 gradient search iterations ($\lambda = 0.45$). And the correspondent convergence of the dome thickness profile within the 15 gradient search iterations, is shown in figure 5-8. It can be seen that there were significant fluctuations in the first several iterations in both of the figures, and no large variation occured afterwards.

Flat Pan

Pan shape is relative complex, comparing with the shape of dome. Its thickness optimisation started with a constant sheet thickness, 5.08 mm (0.2 inch). Figure 5-9 shows the formed pan thickness distribution using this constant thickness. Fifteen iterations

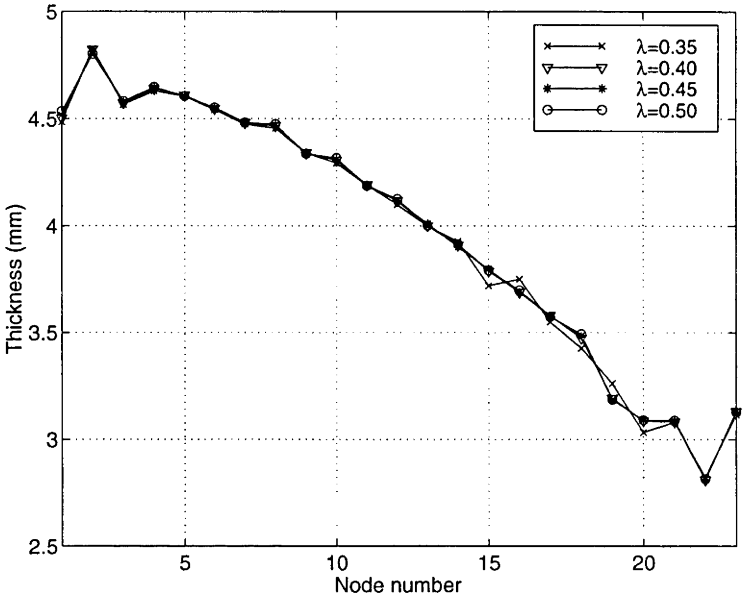

Figure 5-4: The final optimised sheet thickness profiles of hemispherical dome after 15 iterations using gradient search method, when $\lambda = 0.35, 0.40, 0.45$ and 0.50.

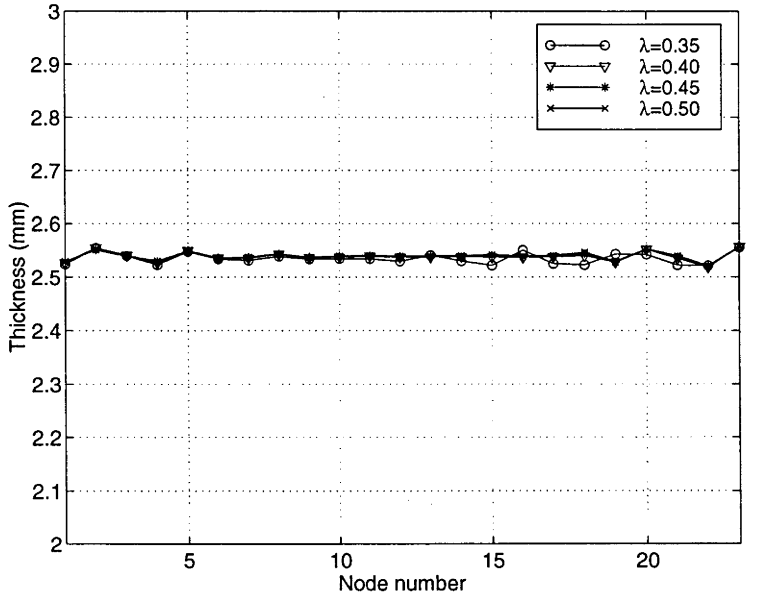

Figure 5-5: The formed dome thickness profiles using the optimised sheet thickness profiles in figure 5-4.

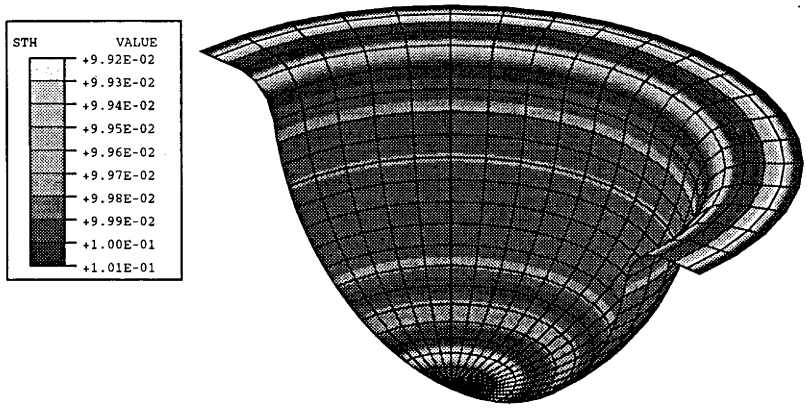

Figure 5-6: Dome thickness distribution using optimised sheet thickness profile after 15 gradient search iterations ($\lambda = 0.45$).

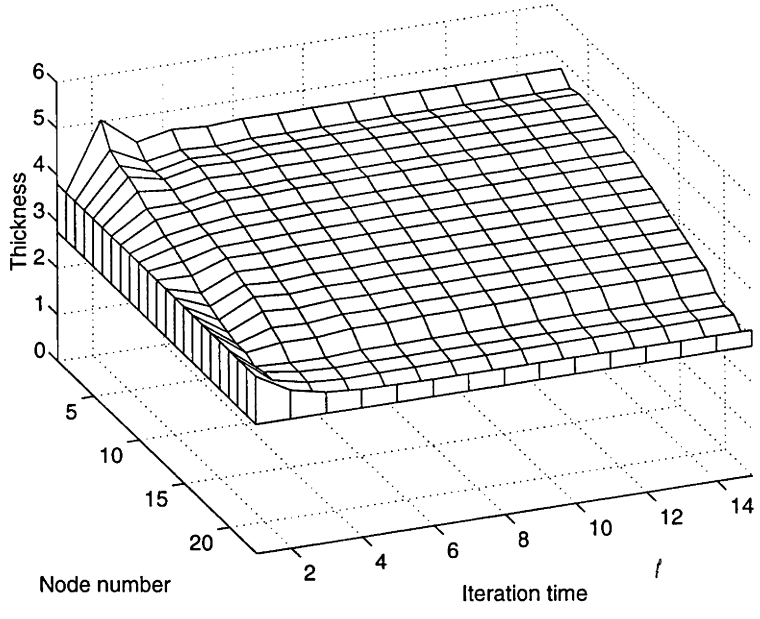

Figure 5-7: The variation of dome sheet thickness profile within 15 iterations using gradient search method ($\lambda = 0.45$).

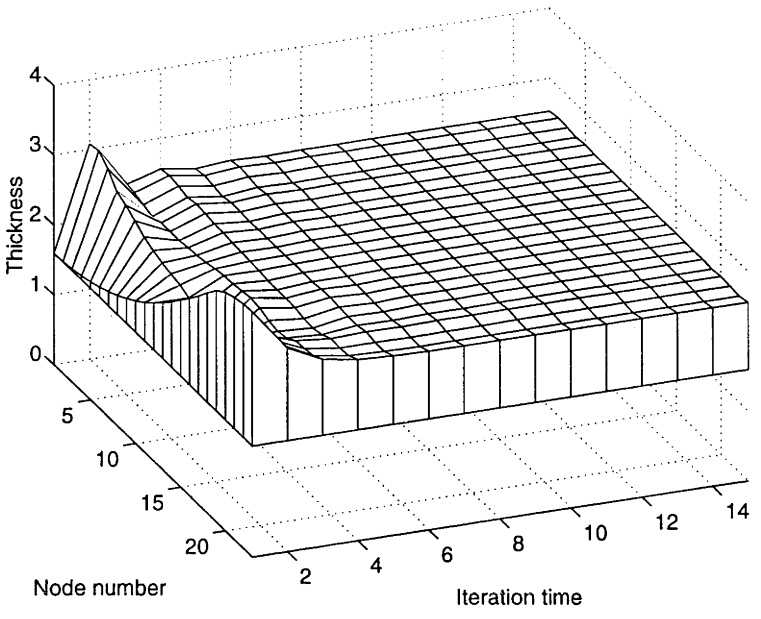

Figure 5-8: The convergence of dome cross-section thickness profile within 15 iterations using gradient search method ($\lambda = 0.45$).

were then performed using gradient search algorithm.

Figure 5-10 and 5-11 show the the criterion convergences of pan model by a set of step length λ. All the curves start at the same point where the criterion is 1.57 mm^2.

In figure 5-10, the convergence speed increases while λ increases. The four curves are generally smooth. The best convergence is made by $\lambda = 0.2$ at the fifteenth iteration where the criterion is 1.403×10^{-3} mm^2.

However in figure 5-11, the curves are disordered and zigzag, except that of $\lambda = 0.2$. No convergence is achieved when $\lambda = 0.35$ and 0.4. Convergences are achieved in the first 6 iterations, when $\lambda = 0.25$, 0.30, but no further drop of the curves in the rest iterations. The best performance in this figure is done by $\lambda = 0.2$ whose convergence curve is steep and smooth.

The optimised sheet thickness profiles and their correspondent formed pan thickness profiles are exhibited in figure 5-12 and 5-13 respectively[3].

The sheet thickness curves in figure 5-12 are similar to each other. They start from about 5.6mm at node 1, and remain in the range of 5.7 $\sim$ 6.0mm in the first 10 nodes.

[3]Because the criterion convergence of $\lambda = 0.25$ reaches its trough at the tenth iteration within the 15 iterations, the sheet thickness profile of the tenth iteration and its correspondent formed pan thickness will be considered as the optimised ones.

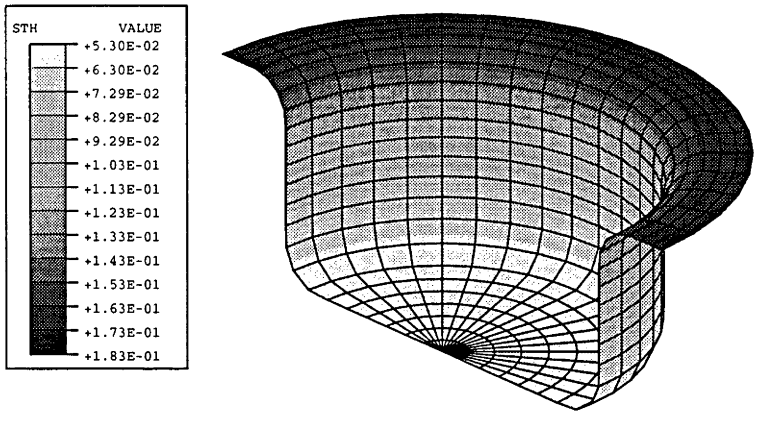

Figure 5-9: Pan thickness distribution, using 5.08 mm thick sheet.

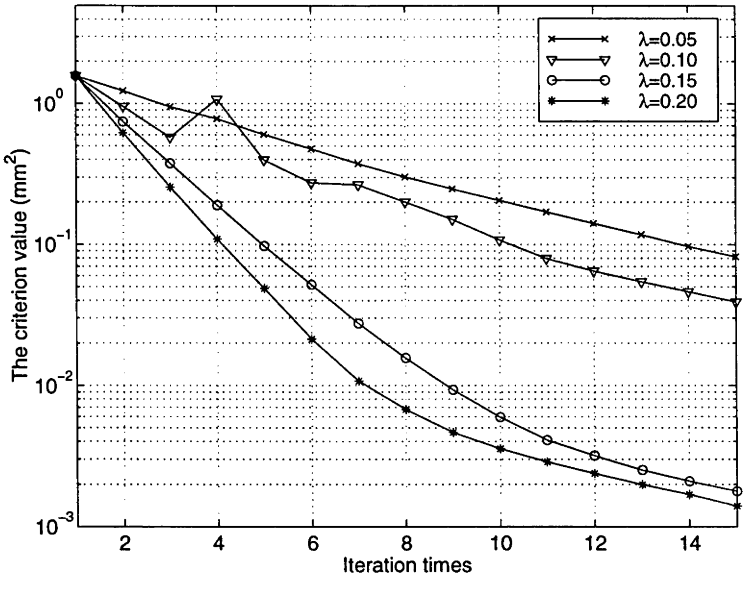

Figure 5-10: Criterion convergences of flat pan model by gradient search method with lower values of λ.

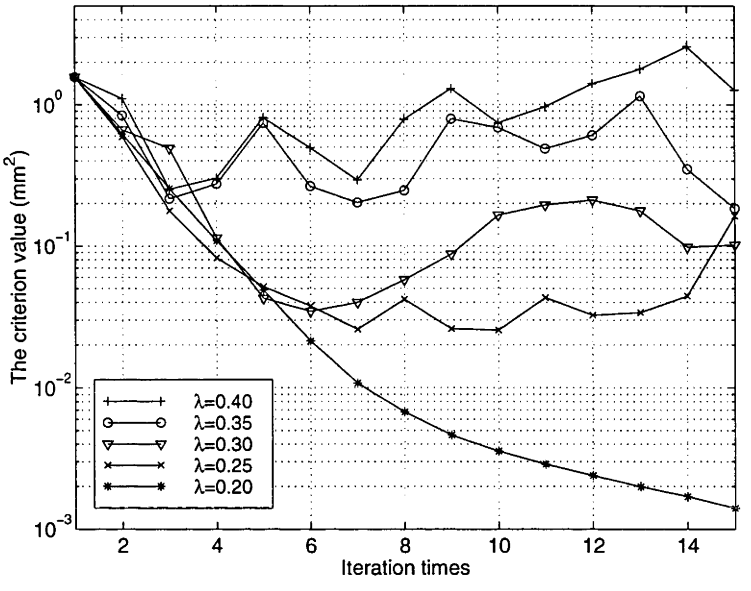

Figure 5-11: Criterion convergence of flat pan model by gradient search method with higher values of λ.

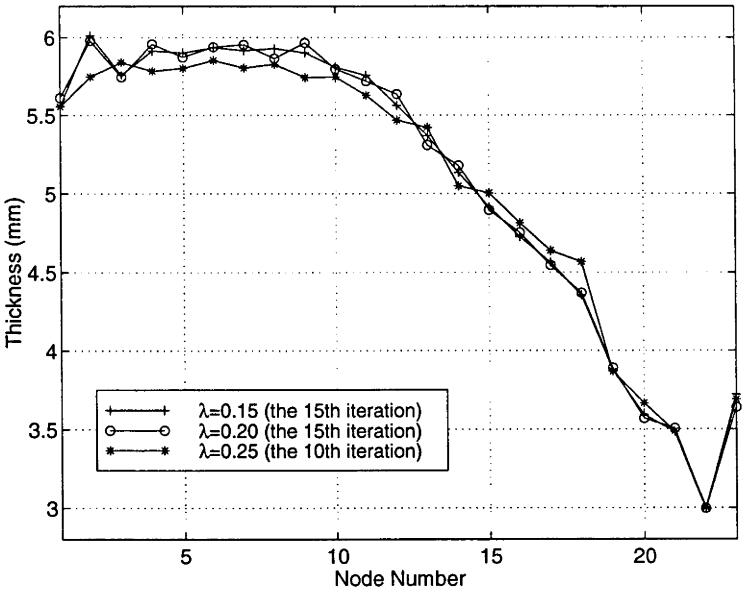

Figure 5-12: The final optimised sheet thickness profiles of flat pan using gradient search method, when $\lambda = 0.15$, 0.2 and 0.25.

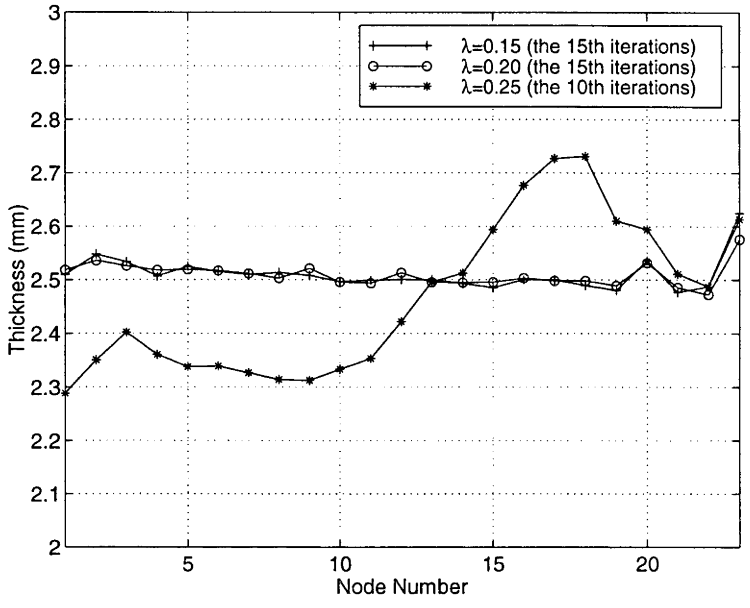

Figure 5-13: The formed dome thickness profiles using the optimised sheet thickness profiles in figure 5-12.

Then from node 10, the profiles drop down almost linearly to 3mm at node 22 and jump up to 3.7mm at node 23. By intuitive observation, it can be seen that the profiles of $\lambda = 0.15$, 0.2 are quite consistent, whereas the curve of $\lambda = 0.25$ is lower than the other two before node 13, and higher in the rest of the nodes.

The formed pan thickness profiles in figure 5-13, when $\lambda = 0.2$ and 0.25, are quite close because of the similarity of their sheet thickness profiles in figure 5-12. These two curves scatter in a narrow band $2.47 \sim 2.55$ mm, except at node 23. However the pan thickness profile of $\lambda = 0.25$ inherits the feature of its sheet profile, and is lower than the other two before node 13 and higher in the rest part. Its distribution interval is as large as $2.29 \sim 2.74$ mm.

The pan thickness distribution, using the optimised sheet thickness profile by gradient search method ($\lambda = 0.2$), is displayed in figure 5-14.

The optimisation of sheet thickness and the convergence of its correspondent pan thickness profile within 15 gradient search iterations ($\lambda = 0.2$) are exhibited in figure 5-15 and 5-16 respectively.

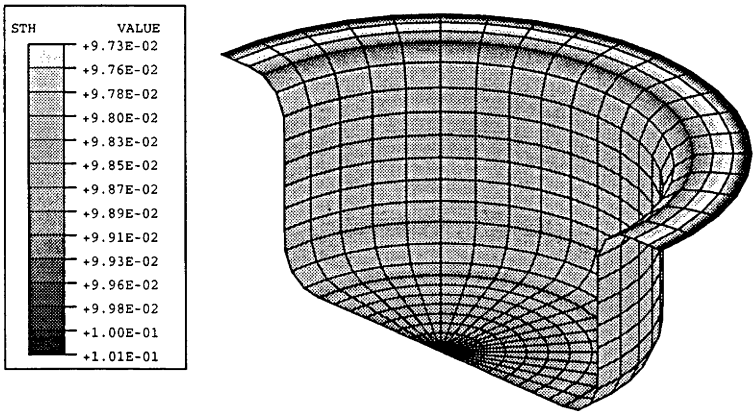

Figure 5-14: Pan thickness distribution using optimised sheet thickness profile by 15 gradient search iterations ($\lambda = 0.2$).

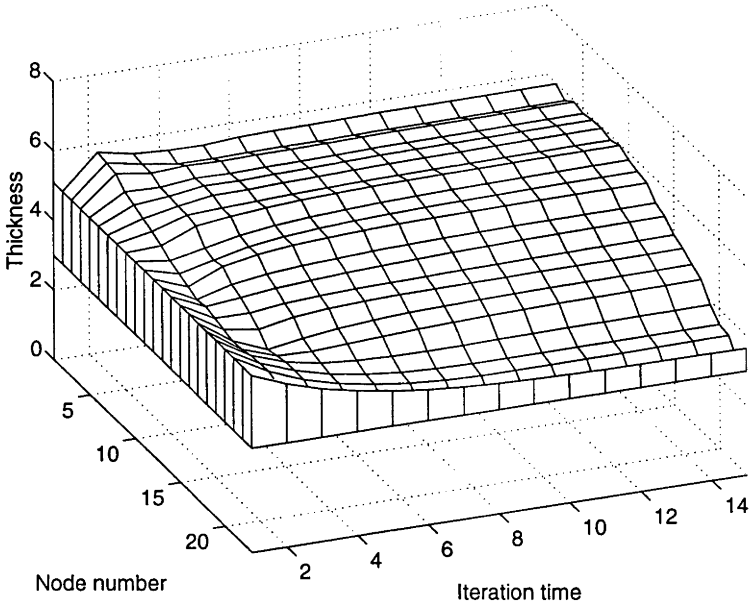

Figure 5-15: The changes of pan sheet thickness profile within 15 iterations using gradient search method ($\lambda = 0.2$).

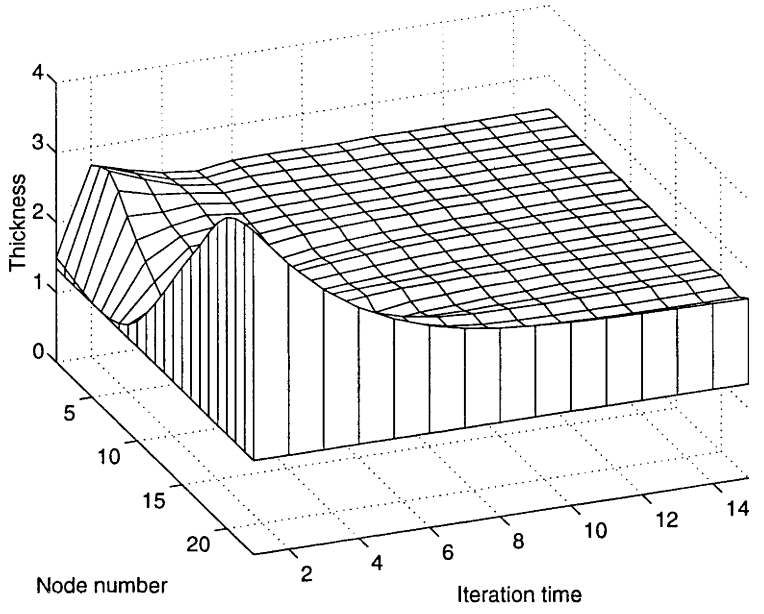

Figure 5-16: The convergence of pan cross-section thickness profile within 15 iterations using gradient search method ($\lambda = 0.2$).

5.3.3 Summary

Some useful hints can be drawn from the sheet thickness optimisation of both dome and pan shapes using gradient search method.

Firstly, the gradient search method is a feasible method in the sheet thickness optimisation of SPF. Reasonable good convergences can be achieved by applying different values of λ for different cases. Normally the convergence curves exhibit a shallow concave shape which means that the convergence speed decreases slightly while iteration time increases.

Secondly, the step length λ plays an important role in gradient search. An optimal constant λ^*, which leads to a steepest smooth convergence track, exists. When $\lambda \leq \lambda^*$, larger values of λ lead to faster convergences and the convergence curves are generally smooth; whereas faster convergences can be obtained by smaller λ when $\lambda \geq \lambda^*$, but oscillatory convergent lines become typical. Also for a simple shape model like the hemispherical dome, λ^* is large than the one of a complex shape like flat pan. λ^* values in these two cases are less than 1.

Finally, computational efficiency[4] is brought on the focus. For a single ABAQUS

[4]The calculation of the computational efficiency is based on the computer model SiliconGraphics R8000.

execution of dome and pan models which both contained 23 nodes, the computation times were about 30 seconds and 55 seconds respectively. For each gradient search iteration, there were $23+1$ ABAQUS executions which took about 12 and 22 minutes for the dome and pan respectively. Therefore for 15 iterations, the total times used for the dome and pan were about 3 hours, and 5.5 hours respectively. However if gradient search is employed in the thickness optimisation of the 3-D box model which contains 759 nodes, 15 gradient search iterations will take about 2.3 years, which is obviously impractical.

5.4 Proportional Control Method

The proportional control method has been specially designed for the purpose of SPF sheet thickness optimisation.

From the intuition of the observation of the SPF process and the simulation process, it is easy to find out that, for the point whose component thickness value is less than the required one, it would be preferable to have a thicker sheet thickness at that point; on the other hand, a thinner sheet thickness is preferred at the point which has a higher component thickness value. Proportional control method is developed based on this consideration.

5.4.1 Implementation of Proportional Control Method

The substance of proportional control method is to correct the sheet thickness of the ith node using a proportion of the error occured at this node, which is the difference between the component thickness t_i and the target component thickness t^*. Although this change of sheet thickness will, more or less, lead to the variations of component thicknesses at other nodes, the ith node will take the most of the advantage.

Suppose there are n nodes in a finite element model. The proportional control takes the form which is, for the ith node:

$$T_i^{(k+1)} = T_i^{(k)} - pe_i \tag{5.12}$$

where T_i is the ith node sheet thickness, k is the iteration time, p is proportion control parameter, e_i is the difference between the ith node component thickness t_i and the target component thickness t^*, that is $e_i = t_i - t^*$. If $t_i > t^*$, $T_i^{(k+1)}$ will be less than

its previous value $T_i^{(k)}$ by equation 5.12. Conversely, $T_i^{(k+1)}$ will be larger than $T_i^{(k)}$, if $t_i < t^*$.

From equation 5.12, we can see that the proportional control gives the feedback to a node directly for the error occuring at that node. Also it is worth noting that, from the physical intuition, obviously p is a non-negative number.

5.4.2 Sheet Thickness Optimisation by Proportional Control Method

The models involved in this section include hemispherical dome, flat pan and 3-D box, whose geometries and material properties have been specified in section 3.4. The first two models have been adopted in section 5.3.2. Automatic loading pressure scheme is once again used in all the simulations. The target component thickness of hemispherical dome and flat pan is 2.54mm (0.1 inch), and the one of 3-D box is 1.778mm (0.07 inch).

Hemispherical Dome

The thickness optimisation of the hemispherical dome still started with the constant sheet thickness 3.81mm (0.15 inch). Its correspondent formed dome thickness distribution has been shown in figure 5-1. The total iteration time is 15.

Figure 5-17 and 5-18 show the criterion convergences of dome model by a set of proportional control parameter p.

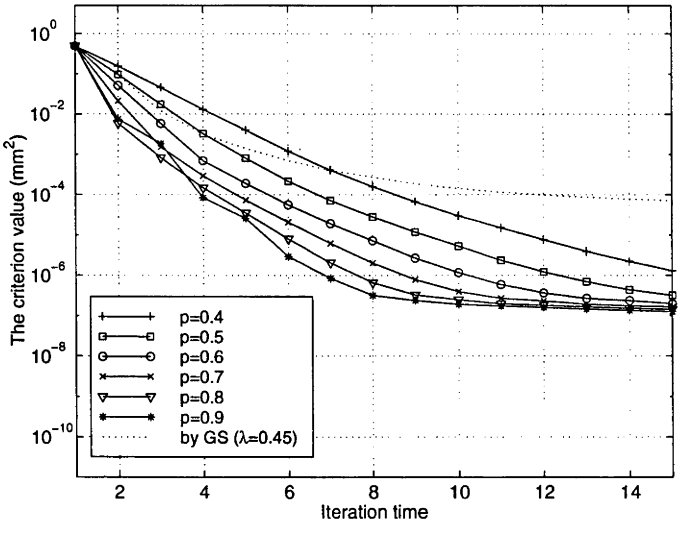

Figure 5-17: Criterion convergences of hemispherical dome model by proportional control method with lower values of p.

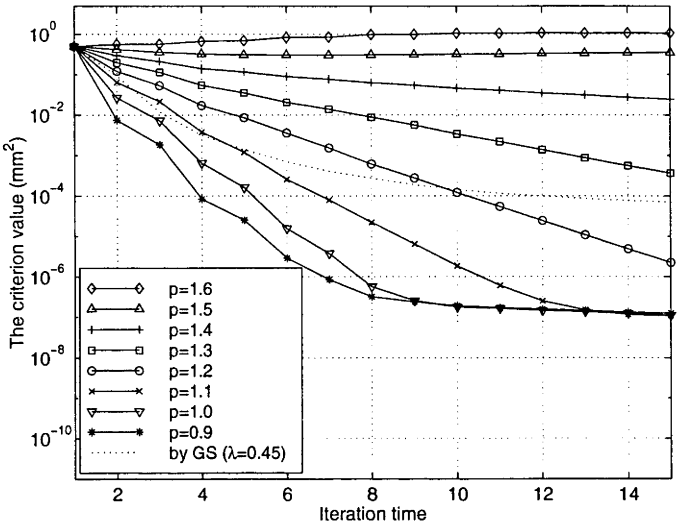

Figure 5-18: Criterion convergences of hemispherical dome model by proportional control method with higher values of p.

The convergence curves in these two figures are generally smooth and evenly distributed in the semi-logarithmetic coordinates. In figure 5-17 criterion convergent speed increases when p value rises. All the curves appear to be shallow concave shape which indicates that the convergent speeds slightly deceased while the criterion was converging. However, for $p = 0.7, 0.8, 0.9$, further convergence almost stopped when the criterion reached the area $1.5 \times 10^{-7} \sim 3.2 \times 10^{-7}$ mm^2. The reason is that the criterion is so small that , within the numerical stability of the algorithm used, it is regarded as *zero*. The smallest value of criterion, 1.25×10^{-7} mm^2, in this figure was achieved by $p = 0.9$ in the fifteenth iteration.

The convergent tracks appear to be straight lines in figure 5-18 except those of $p = 0.9$. Even distribution can also be seen in this figure. The convergent speed decreased when p value increased. It is worth noting that the convergent line of $p = 1.5$ is extremely flat and the line of $p = 1.6$ is, even slightly increasing upwards. These indicate that excessively large values of p can lead to extensive fluctuation of nodal thicknesses so that there is no criterion reduction achieved. Just like the figure 5-17, little convergence was achieved when the criterion reached the area $1.5 \times 10^{-7} \sim 3.2 \times 10^{-7}$ mm^2. Although the lowest criterion value, 1.08×10^{-7} mm^2, was obtained in the fifteenth iteration when $p = 1.1$, the best overall performance was acquired by $p = 0.9$ so far as concerns convergent speed. The criterion convergent curve by gradient

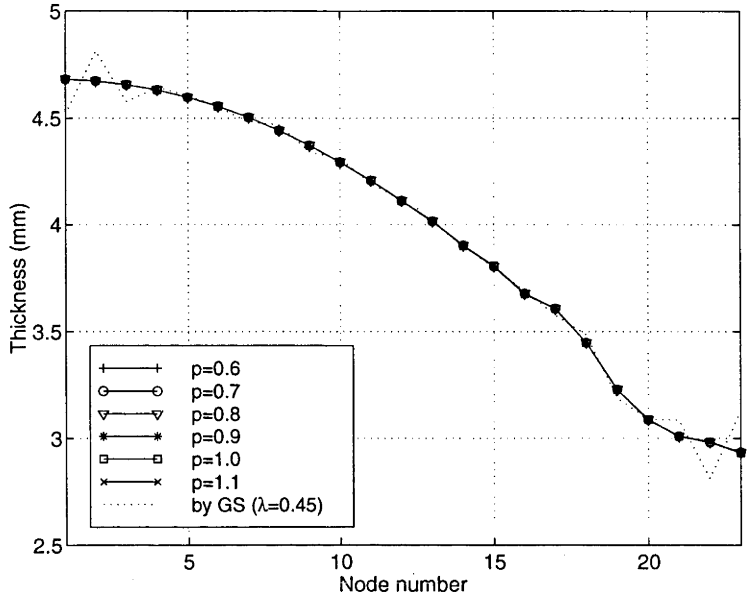

Figure 5-19: The final optimised sheet thickness profiles of hemispherical dome after 15 iterations using proportional control method, when $p = 0.35$, 0.40, 0.45 and 0.50.

search ($\lambda = 0.45$) is displayed for contrast.

The final optimised sheet thickness profiles, with $p = 0.6$, 0.7, 0.8, 0.9, 1.0 and 1.1, are exhibited in figure 5-19, where the optimised sheet thickness profile using gradient search method is also displayed for the sake of contrast. All the solid lines coincide with each other so close that it seems only one curve appearing in the plot. They start at the dome centre with thickness 4.68mm and gradually go down to 2.93mm at dome edge. The dotted profile by gradient search is consistent with solid lines except at the beginning and end.

Overlaps of solid lines are also seen in figure 5-20 where the formed dome thickness profiles, using the optimised sheet thicknesses in figure 5-19, are shown. All the solid profiles exactly locate on the line where thickness is 2.54mm, and are quite flat in the first 12 nodes whereas slight waves appearing in the rest of the nodes. Further more all the solid lines distribute in a very narrow band, 2.54 ± 0.001mm. The large fluctuations of the dotted dome thickness profile generated by gradient search is due to the vertical axis being finely scaled.

The dome thickness distribution, using the optimised sheet thickness profile by proportional control method, is displayed in figure 5-21.

Figure 5-22 shows how the sheet thickness profile was optimised within the 15 pro-

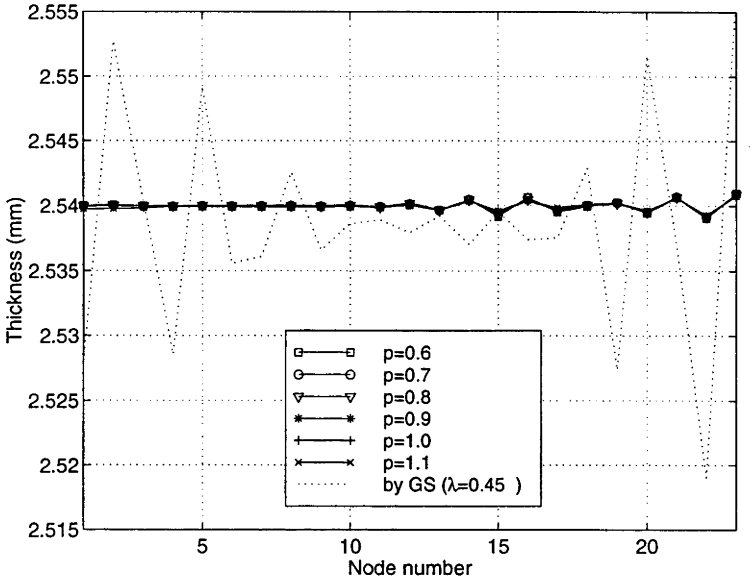

Figure 5-20: The formed dome thickness profiles using the optimised sheet thickness profiles in figure 5-19.

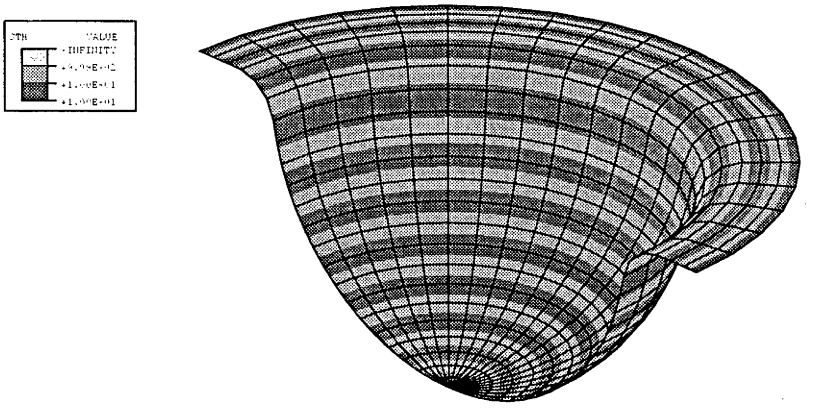

Figure 5-21: Dome thickness distribution using optimised sheet thickness profile by 15 proportional control iterations ($p = 0.9$).

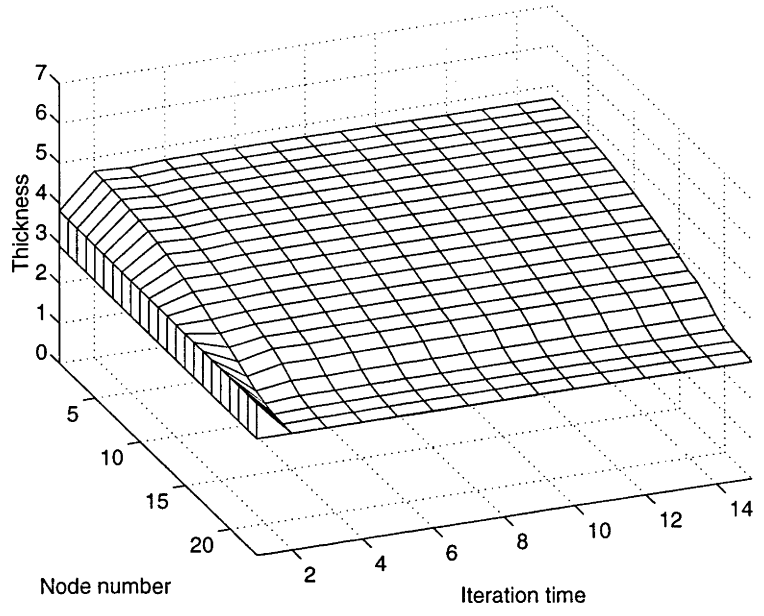

Figure 5-22: The changes of dome sheet thickness profile within 15 iterations using proportional control method ($p = 0.9$).

portional control iterations, when $p = 0.9$. And the convergence of the dome thickness profile with in the 15 proportional control iterations, is also shown in figure 5-23. In these two figures large fluctuations only occured at the first couple of iterations.

Flat Pan

The thickness optimisation of flat pan commences with the sheet thickness 5.04 mm (0.2 in), and the correspondent formed pan thickness distribution has been shown in figure 5-9. The total iteration time applied was 20 instead of 15.

The criterion convergences of the flat pan by a series values of proportional control parameter p are exhibited in figure 5-24 and 5-25.

The convergence speed slightly decreased when p decreased in figure 5-24 in which $p \leq 0.8$. The convergent curves are not as smooth as those of the hemispherical dome, especially in the first 10 iterations. Significant convergences stopped when the criterion was less than 1×10^{-6} mm^2. The shallow concave shapes of these curves indicate that the convergent speed slightly decreased while the iteration time was increasing. On the other hand straight lines emerge again in figure 5-25 in which $p \geq 0.8$. The shape of the tracks of $p = 0.8, 0.9$ are zigzag in the first 10 iterations, but the other two are not. Also there was little further criterion convergence achieved after the criterion arrived

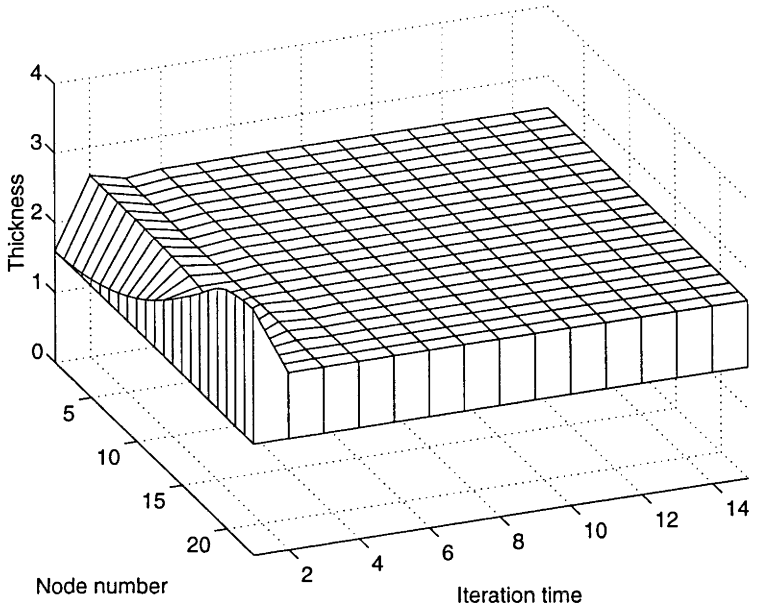

Figure 5-23: The convergence of dome cross-section thickness profile within 15 iterations using proportional control method ($p = 0.9$).

at 1×10^6 mm^2. The criterion convergent curve by gradient search ($\lambda = 0.2$) is plotted as dotted line for comparison.

Figure 5-26 shows the final optimised sheet thickness profiles, when $p = 0.5$, 0.6, 0.7, 0.8 and 0.9. The solid lines, just like those of the dome, coincide with each other. They start from thickness 5.86mm at node 1, slightly go up to 6.02mm at node 7, and then gradually come down to 3.25 at the end node. Form the dotted line which is the optimised sheet thickness profile by gradient search ($\lambda = 0.2$), one can see that the optimised sheet thickness profiles by proportional control and gradient search are close. However, relatively large differences exist in both central and edge areas.

In figure 5-27, the solid lines represent the formed pan cross-section thickness profiles, and locate exactly on the line of 2.54mm which was the target value. These profiles are very flat in the first 10 nodes whereas there are slight waves on the rest nodes. The distribution of the pan thicknesses scatter in a pretty small region, 2.54 ± 0.023 mm. The fluctuating dotted line represents the dome thickness profile using the optimised sheet thickness by gradient search ($\lambda = 0.2$), and it distributes in a much wider range.

The pan thickness distribution, using the optimised sheet thickness profile by proportional control method, is displayed in figure 5-28.

Figure 5-29 shows how the sheet thickness profile of pan was optimised from original

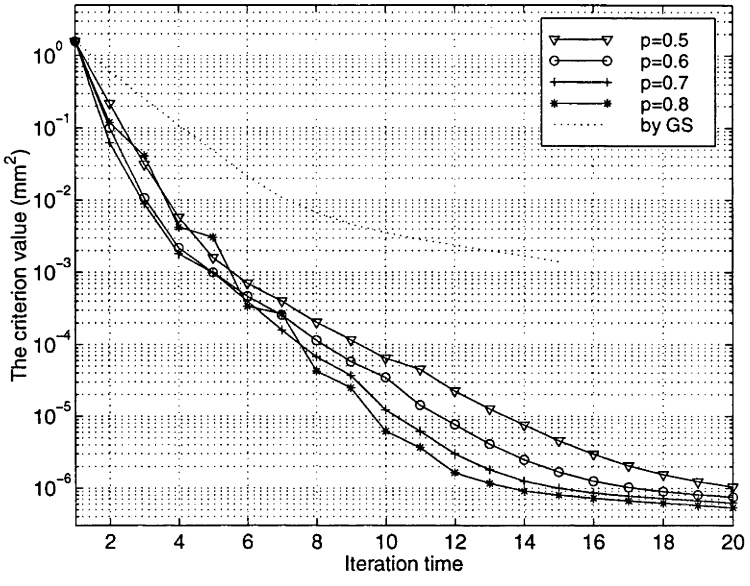

Figure 5-24: Criterion convergences of flat pan model by proportional control method with lower values of p.

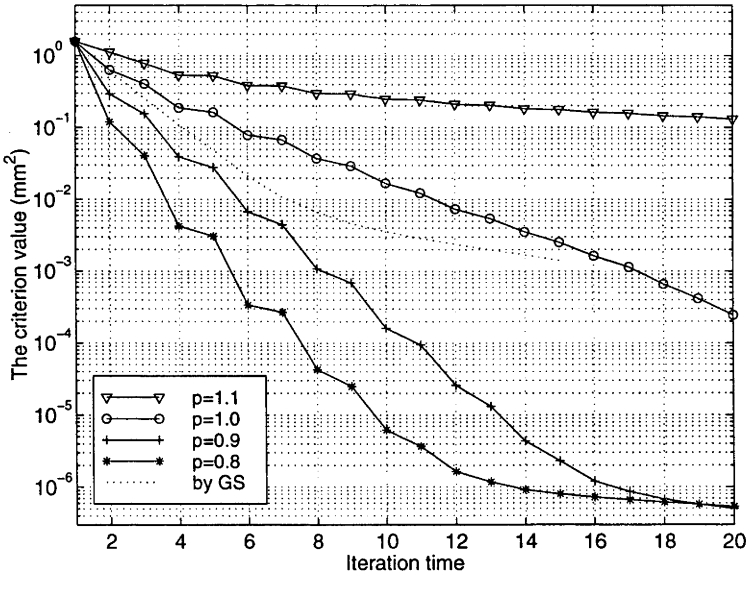

Figure 5-25: Criterion convergences of flat pan model by proportional control method with higher values of p.

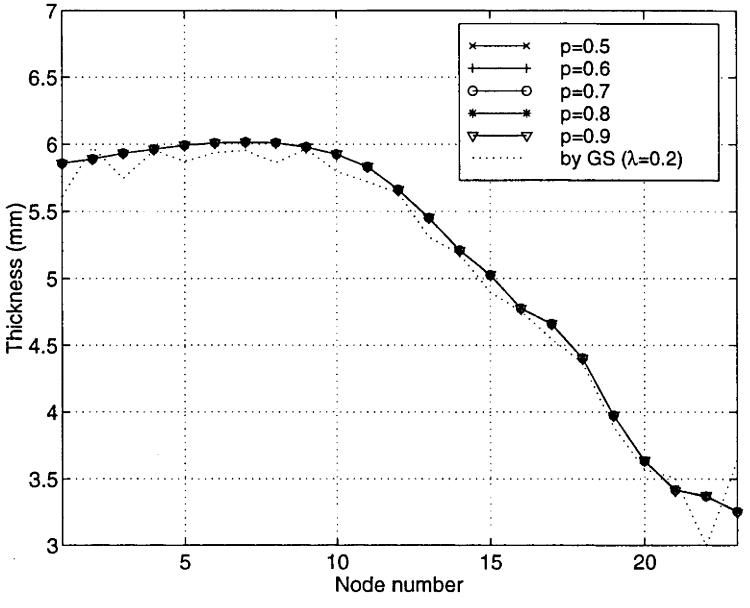

Figure 5-26: The final optimised sheet thickness profiles of flat pan after 20 iterations using proportional control method, when $p = 0.5$, 0.6, 0.7, 0.8 and 0.9.

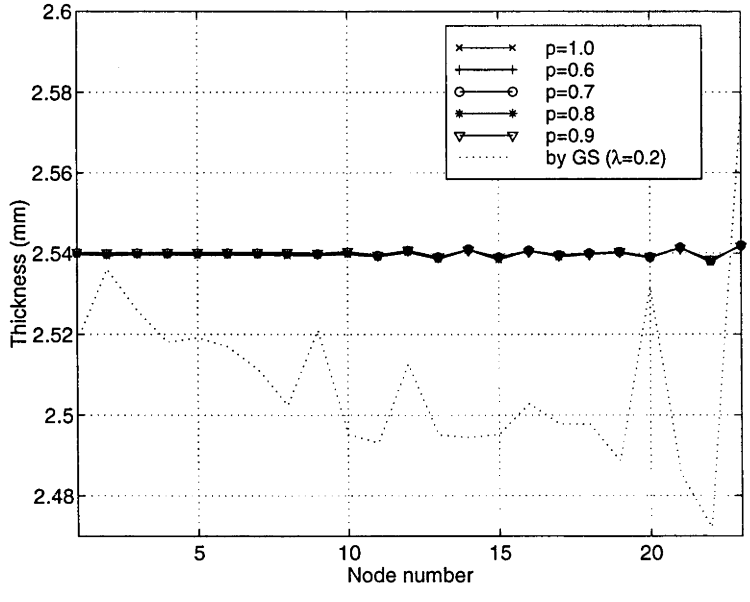

Figure 5-27: The formed pan thickness profiles using the optimised sheet thickness profiles in figure 5-26.

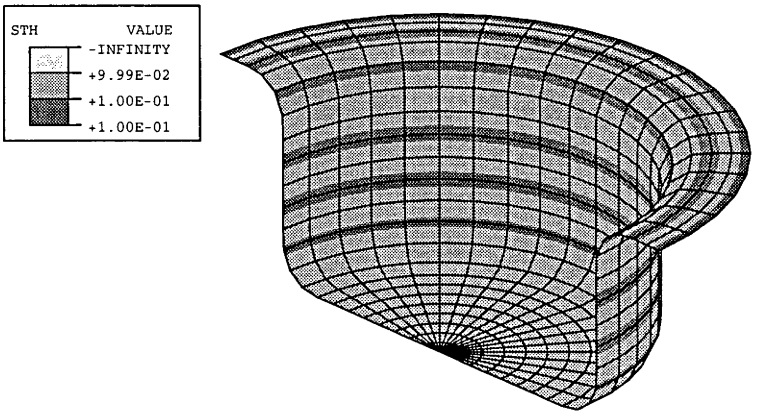

Figure 5-28: Pan thickness distribution using optimised sheet thickness profile by 15 proportional control iterations ($p = 0.9$).

constant shape to the final optimised one within the 20 proportional control iterations. And the convergence of the pan thickness profile within the 20 proportional control iterations, is also shown in figure 5-30. Large fluctuations occured in the first several iterations in both of the two figures, and there was no significant change in the following iterations.

3-D box

This 3-D box is more like a practical application. The thickness optimisation of the 3-D box started with constant thickness 3.175 mm (0.125 in) and aimed at the target component thickness 1.778 mm (0.07 in). The proportional control algorithm was repeated for 15 times which took about 24 hours. The thickness distribution of a quarter of formed box using 3.175 mm thick sheet is displayed in figure 5-31.

The criterion convergence of the 3-D box by a set of values of proportional control parameter p are displayed in figure 5-32 where the same scene as those in the criterion convergent plottings of the dome and pan are presented again. The fastest convergence was achieved with $p = 0.8$. When $p > 0.8$, the convergent speed (dotted lines) dropped quickly while p increased. On the other hand, decrease of p led to slight decline of

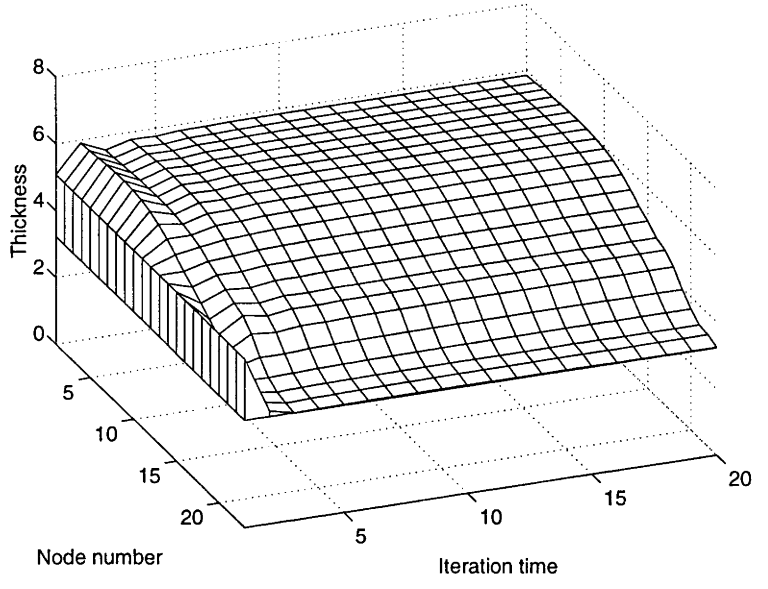

Figure 5-29: The changes of pan sheet thickness profile within 20 iterations using proportional control method ($p = 0.8$).

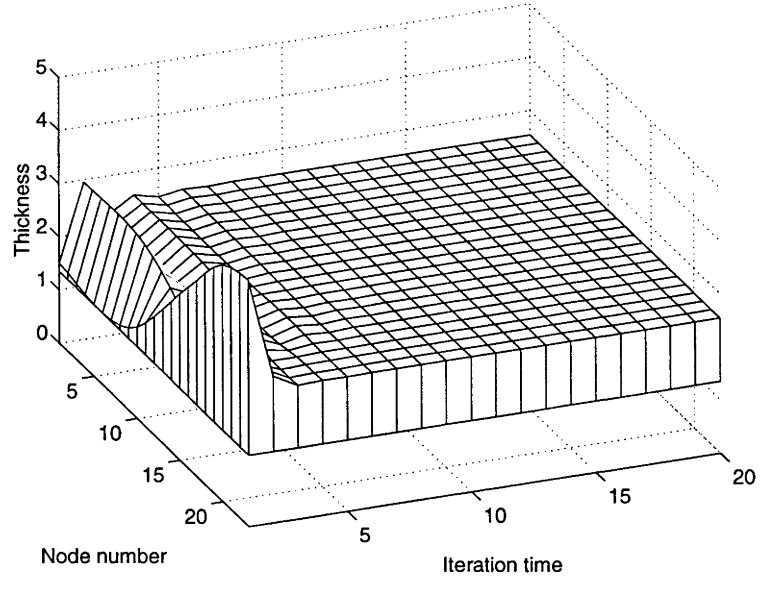

Figure 5-30: The convergence of pan cross-section thickness profile within 20 iterations using proportional control method ($p = 0.8$).

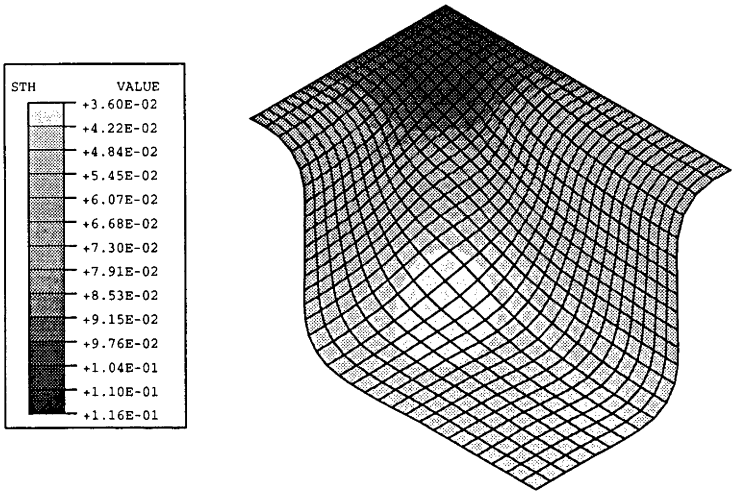

Figure 5-31: 3-D box thickness distribution, using 3.175 mm (0.125 in) thick sheet.

criterion convergent speed when $p < 0.8$. The convergence of $p = 0.7$, 0.8 followed straight tracks in the semi-logarithmetic coordinate, but further convergence stopped when the criterion arrived at 1×10^{-6} mm^2, whereas concave convergent curves became typical when $p = 0.9$, 1.0 and 1.1.

The formed box thickness, in figure 5-33, using the optimised sheet thickness profile ($p = 0.8$) is very close to constant as all the nodal thicknesses are located in a narrow band 1.778 ± 0.00254 mm. The final optimised sheet thickness profile of the 3-D box is plotted in figure 5-34.

5.4.3 Summary

Good thickness optimisation performances in SPF are achieved by the proposed proportional control method in the models of hemispherical dome, flat pan and 3-D box. The proportional control parameter p is of the utmost important for the criterion convergence speed. There exists an optimal value of p^* which can lead to the fastest criterion convergence for each particular model. When $p < p^*$, the convergent speed decreases slowly while p is declining. Conversely, when $p > p^*$, the convergent speed decreases quickly while p is increasing. The optimal p^* of the dome, pan and box are 0.9, 0.8 and 0.8 respectively, and these values are close. Further more there is a particular p^*

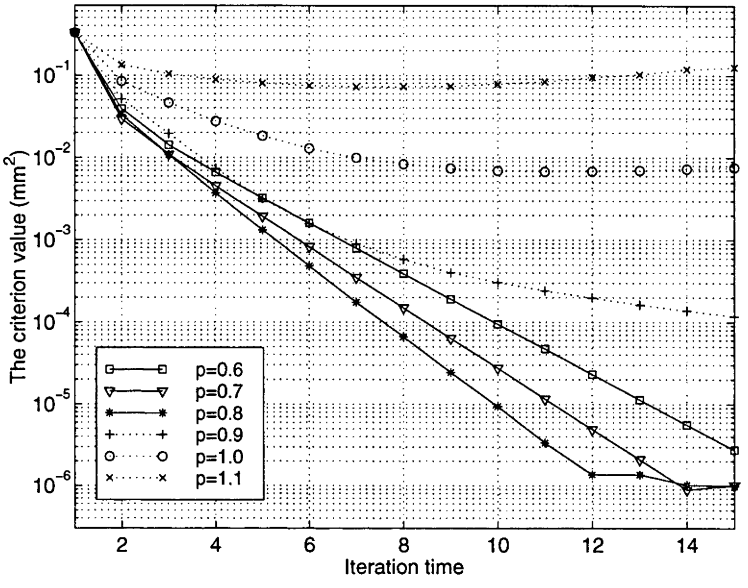

Figure 5-32: Criterion convergences of 3-D box model by proportional control method.

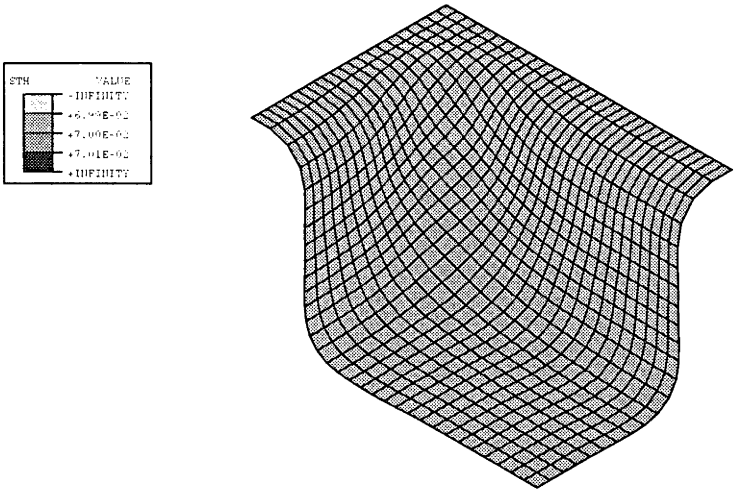

Figure 5-33: 3-D box thickness distribution using the optimised thickness profile obtained after 15 proportional control iterations ($p = 0.8$).

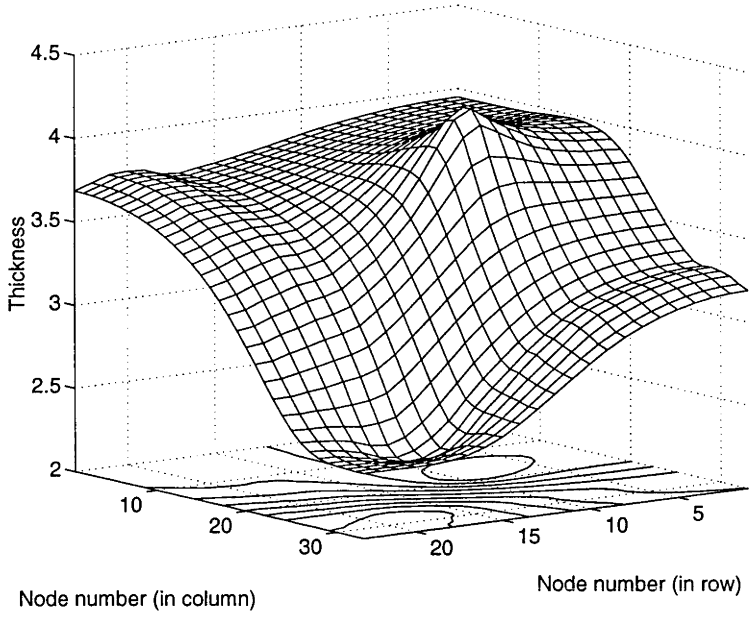

Figure 5-34: A quarter of final optimised sheet thickness profile of 3-D box after 15 proportional control iterations ($p = 0.8$). The node in (1, 1) is correspondent to the central node of the box.

for each case, good criterion convergence can be obtained when p is between 0.5 to 0.9, and this indicates that applicable area of p is wide.

Most of the optimised sheet thickness profiles and their correspondent formed component thickness profiles are so close to each other in these three models, that only one curve appears on the plot. Their difference can hardly be seen without fine-scaled axes.

Generally there are no significant "jump" appearing on the convergent curves. However further convergence becomes very slow once the criterion arrives to a certain small value, normally between $10^{-6} \sim 10^{-7}$ mm^2 for these three models.

Economic computations can be achieved by applying proportional control method. 15 iterations of dome model and 20 iterations of pan model took about 7.5 minutes and 18 minutes respectively. The model of 3-D box took about 24 hours for 15 runnings. However the criterion converged to excessive small values in these three models. Acceptable results may come out even after several iterations depending on the requirement of the accuracy. Therefore computational time could be further cut down.

Chapter 6

Experimental Works

This chapter demonstrates the experiments involved in this project. The purpose of these experiments is to validate the simulations of ABAQUS and the optimisation of the sheet thickness of SPF. This was achieved by the development of a dome blowing rig used to superplastically deform Sn-Pb sheets. The nature of the material allowed deformation to take place at temperatures just above room temperature. This greatly simplified the experiments. In addition hot water under mains pressure was sufficient to form the domes.

6.1 Material

The superplasticity of Sn-Pb alloys has been widely studied [70, 71, 72] in the past twenty years. Unlike aluminium and titanium alloys, Sn-Pb alloy exhibits good superplasticity even at the room temperature. This material characteristic minimises the costs of experimental facilities over Al/Ti alloys which require high forming temperatures.

6.1.1 Material Properties

Sn-Pb eutectic alloy, which was used in the experiments, is vacuum extruded as a bar shape and is primarily used as solder. The composition of the eutectic Sn-Pb alloy bar (1kg) provided by the supplier [1] is listed in table 6.1. The properties provided by the supplier is listed in table 6.2

[1] These eutectic Sn-Pb bars were sold by MULTICORE SOLDERS (AUSTRALIA) PTY. LTD.

Element	Percentage (B/N 0203) (%)	AS1834.1 (%)	BS219 (%)
Tin	63.000	62.64	63.64
Silver	0.0010	–	–
Arsenic	0.0080	0.03max	0.03max
Bismuth	0.0030	0.10max	0.10max
Cadmium	0.0002	0.005max	0.005max
Copper	0.0020	0.08max	0.08max
Iron	0.0020	0.02max	0.02max
Nickel	0.0010	–	–
Antimony	0.0060	0.20max	0.20max
Zinc	0.0002	0.003max	0.003max
Aluminium	0.0005	0.001max	0.001max
Lead	remainder	remainder	remainder

Table 6.1: A typical analysis of Sn-Pb eutectic alloy (1kg bar) with comparison to the Australian Standard for solder AS1834.1 and the British Standard BS219.

Material property	Value
Solidus temperature (^oC)	183
Liquidus temperature (^oC)	183
Density (g/cc)	8.4
Ultimate tensile strength (MPa)	67

Table 6.2: Material properties of eutectic Sn-Pb alloy (1kg bar).

Material property	Value
Young's modulus E (MPa)	10
Poisson's ratio ν	0.34
coefficient A (MPa)	50

Table 6.3: Estimated material properties of eutectic Sn-Pb alloy.

However there is very little information available for other properties, such as Young's modulus E, Poisson's ratio ν, strain rate sensitivity m, the coefficient A in equation 3.16 and the friction coefficient μ of Sn-Pb and perspex surface interaction. These properties are required in ABAQUS simulations.

ABAQUS simulations have been run with different values of Young's modulus E, Poisson's ratio ν and the coefficient A covering the possible forming domains. These changes led to little difference in the dome section thickness profiles. This indicates that reasonable estimations of these properties are acceptable in the simulation of the experiment model. Values for these properties are defined in table 6.3.

Significant changes of dome section thickness profiles, however, do exist while the strain rate sensitivity m and the friction coefficient μ are varying. These two properties will be selected by matching simulation results to the results from pilot experiments carried out.

6.1.2 Material Preparation and Tensile Test

Six Sn-Pb eutectic alloy ingots were prepared by melting 1kg bars in air at above 200^oC, air-casting into a heated aluminium mould with dimensions 110 × 110mm, and then air-cooling down to room temperature. The thicknesses of these ingots were about 10mm.

These ingots were then rolled into 2 ± 0.02mm thick sheets. Table 6.4 shows the thickness reductions of each ingot in the rolling process.

Figure 6-1 shows the rolled sheet microstructure. It can be seen clearly from the picture that there are two phases, lighter phase and darker phase which are lead-rich and tin-rich respectively. The grain size is approximately 5μm which is in keeping with the requirement of superplastic material.

In order to verify the superplasticity of the Sn-Pb alloy prepared, a series of tensile

No. of rolling time	Ingot 1	Ingot 2	Ingot 3	Ingot 4	Ingot 5	Ingot 6
1	8.30	9.20	10.15	9.40	9.60	9.80
2	7.75	8.60	9.60	9.00	8.10	9.10
3	7.25	8.10	9.00	8.30	7.40	8.40
4	6.75	7.70	8.30	7.70	6.80	7.80
5	6.25	7.20	7.60	7.00	6.10	7.10
6	5.75	6.70	7.10	6.30	5.40	6.40
7	5.27	6.20	6.60	5.60	4.70	5.70
8	4.75	5.70	6.00	4.90	4.00	5.00
9	4.30	5.20	5.50	4.20	3.30	4.30
10	3.80	4.70	5.00	3.50	2.60	3.60
11	3.30	4.20	4.50	2.80	2.00	3.00
12	2.65	3.70	4.00	2.30		2.50
13	2.00	3.20	3.50	2.00		2.00
14		2.60	3.00			
15		2.00	2.50			
16			2.00			

Table 6.4: The thickness reductions of ingots in the rolling process.

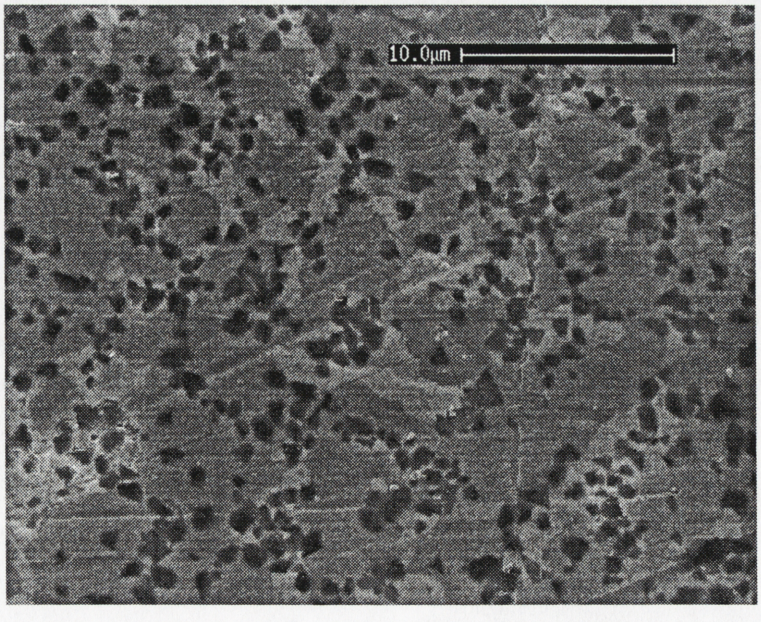

Figure 6-1: The microstructure of rolled sheet. The darker phase is tin-rich.

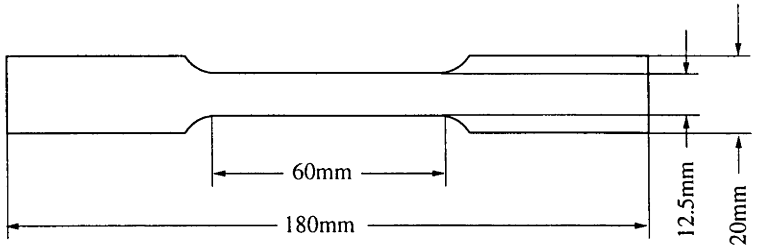

Figure 6-2: Sn-Pb eutectic alloy tensile test specimen (2 mm thick).

test was conducted before the dome forming. The dimension of the undeformed test specimen is shown in figure 6-2. Three specimens which were deformed at different conditions are shown in figure 6-3. The specimen in figure 6-2(b) experienced both day time and night conditions in an environment without air conditioning so that the test temperature was scattered over a relatively wide range. The specimen in figure 6-2(c) was heated by a 100 watts table lamp while testing. However the temperature varied over the specimen length because of the variation in distance from the material to the bulb. From these photos one can see that the temperature and strain rate played the important roles in superplastic forming.

6.2 Experiment Set-up

6.2.1 Geometry Model of Forming Die and Forming Sheet

The geometry of the forming die is similar to the hemispherical dome adopted in the ABAQUS simulation in the last chapter but smaller. Figure 6-4 demonstrates the geometric shape of the forming die. The radius of the dome is 40mm with 8mm fillet radius.

The blank sheet was 120mm square with 2 ± 0.02mm constant thickness, and 5mm square grid was drawn on the surface for intuitive observation. In the case where constant final component thickness was required, surface milling by CNC machine was employed to achieve the optimised sheet thickness profile. Clamping was applied at the concentric circle whose radius was 55mm.

Half of the sheet was modelled by 23 nodes with equal intervals in ABAQUS simulation. Node 1 was the centre of the sheet and node 23 was the clamping point. The material outside of the clamping point was omitted as no stress occured in that part

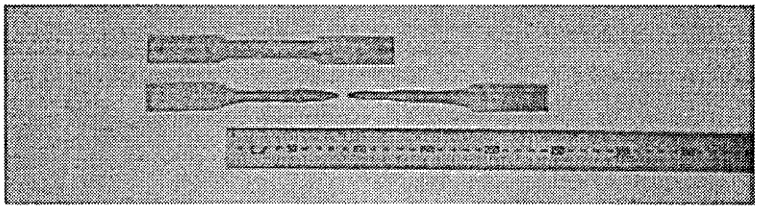

(a)

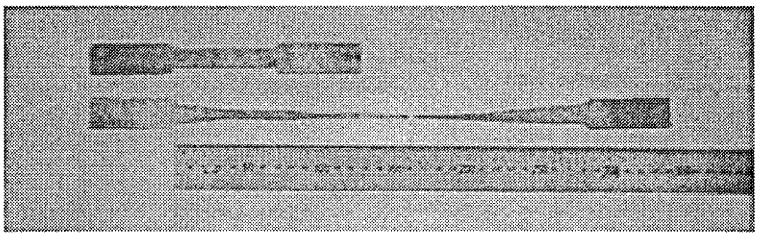

(b)

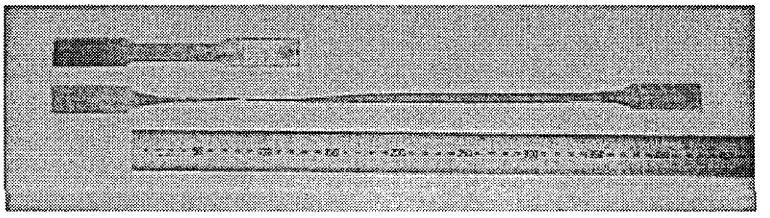

(c)

Figure 6-3: Three deformed Sn-Pb eutectic alloy specimens. (a) Formed with crosshead speed 60mm/hour at about 18^oC to an elongation of 187%. (b) Formed with crosshead speed 12mm/hour at $11 \sim 18^oC$ to an elongation of 443%. (c) Formed with crosshead speed 5mm/hour at $29 \sim 35^oC$ to an elongation of 602%.

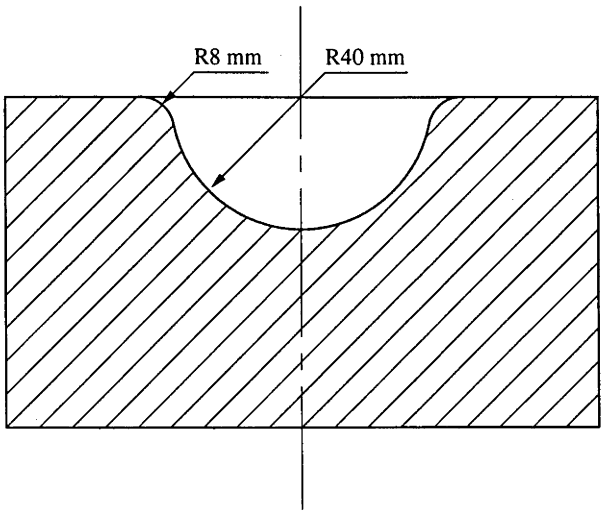

Figure 6-4: The geometric shape of the forming die.

during the forming process.

6.2.2 Experimental Rig and Experiment Procedure

The experimental rig set includes three parts, the water temperature control circuit, the forming pressure control circuit and the pressure forming die set (figure 6-5).

The function of part I is to control the water temperature at which the forming is conducted. Cold mains water flow comes into part I at point A with the main pressure P_0 which is up to 1000 kPa. Part of the main water flow goes into the hot water heater where the water is heated up to 82^oC, and then goes through internal tube of the concentric tube-in-tube heat exchanger. The other part of the main water flows through the external tube of the heat exchanger in from the counter direction. The hot water is then cooled down in the heat exchanger. The cold water flow in the external tube is adjusted by needle valve 1, so that the temperature of the hot water can be set to a stable value in a certain range. Trivial heat loss does occur while hot water is flowing through part II and part III. However this loss will not lead to much of a difference of the forming process. It is worth noting that the temperature measuring point is at the end of one of the outlet hoses of part II as shown in the figure 6-5. Because this point is nearly immediately after the form die set, its temperature can be regarded as the forming temperature.

Part II is used to control the forming pressure applied to the sheet. There are two routes where the hot water can flow though, one is through part III and the other is through needle valve 3. Moderate water flow is required to go through part III. This is because less water flow will not keep the sheet at the desired temperature, on the other hand over flow is a waste of water resource. Desired pressure P_1 can be achieved by adjusting needle valve 3, and the value of P_1 can be read from the pressure gauge.

Part III is the pressure forming die set where the sheet is formed into the configuration of the domed die. Figure 6-6 shows the details of the part III, including inlet and outlet connection, pressure head, forming sheet, domed mould cavity, depth probe and bolts and nuts. The aluminium pressure head is connected to the domed mould cavity block by eight sets of M10 bolt and nut, and the forming sheet is clamped in between. There are three ring-shape teeth on the down side of the pressure head. When the nuts are tighten up, these teeth will "bite" into the Sn-Pb sheet which is much softer than

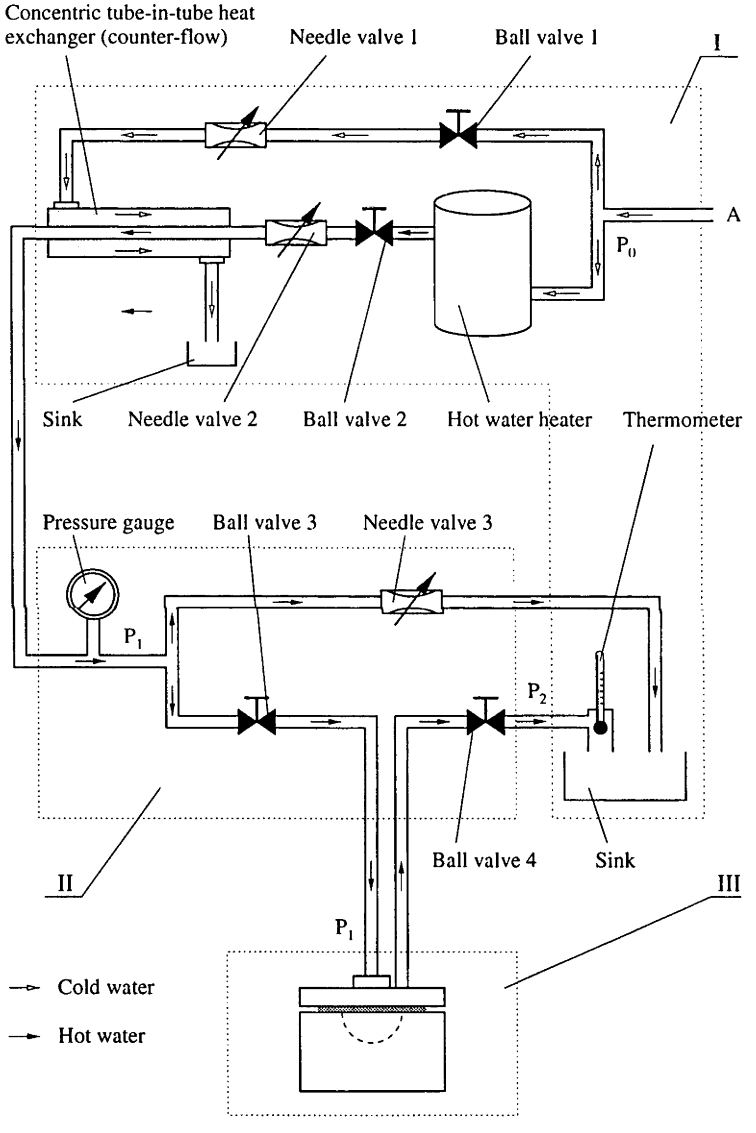

Figure 6-5: Schematic diagram of experimental rig set. Part I is the water temperature control circuit, part II is the forming pressure control circuit, and part III is the pressure forming die set.

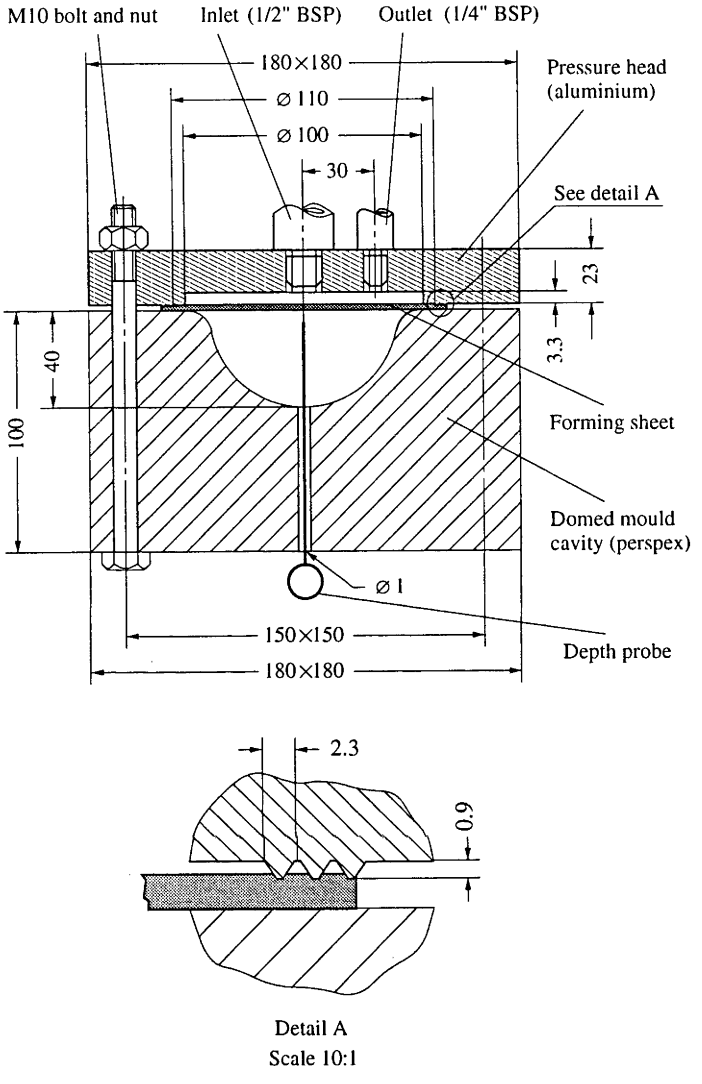

Figure 6-6: The detail of pressure forming die set.

aluminium. There are two purposes for these teeth: first the teeth will hold the sheet in place, and this is equivalent to the boundary condition applied in FEA model in ABAQUS; the second use is to seal up the chamber enclosed by the pressure head and the forming sheet. The domed mould cavity is made of perspex block. Its surface is polished so that the forming process can be observed through the block. There is a $\phi 1$ mm bleeding hole at the centre of the cavity. A depth probe is inserted into this hole to measure the deflection of the sheet.

Two procedures, rig pre-heating and sheet forming, are followed in the forming process.

Although it is widely accepted that Sn-Pb exhibits superplasticity at room tem-

perature, better and quicker forming process can be expected by applying higher temperature in this experiment. Limited by the condition of the hot water heater, the temperatures applied in the experiments are between $70 \sim 75^oC$. This temperature range is higher than room temperature ranging from 20^oC to 30^oC. So pre-heating rig has to be done in order to maintain the forming conditions steady. At the beginning of a experiment, needle valve 1 and ball valve 1 are kept close. Then moderate hot water flowing through the part II and III of the rig is obtained by adjusting needle valve 2, while all the other valves in the hot water route are opened. There is no significant pressure in the forming die set at this stage. When the temperature reading is approaching to the required temperature, ball valve 1 is fully opened and needle valve 1 is adjusted until the temperature just stays in the desired scale.

After pre-heating the rig set, ball valve 4 is set to be half open, whereas needle valve 2 is fully opened. Then needle valve 3 is tuned downward until back pressure accumulated in the part III reaches the required value. Hence the sheet is in the required forming conditions. Slight drifts of temperature and pressure can be corrected by tuning up needle valve 1 and 3 respectively. The sheet is slowly inflated into the configuration of the forming die by pressured water. This process lasted from 20 minutes up to two and half hours, depending on the pressure, the temperature and the sheet thickness profile. The air in the chamber enclosed by the sheet and the domed cavity is bled off through the bleeding hole during forming. The deformation of the centre point of the sheet can be measured by inserting a depth probe into the bleeding hole. The completion of the forming process can be determined by either the depth of the probe or observation.

To terminate the forming process, ball valve 1 and 2 are turned off. It is preferable to store the formed dome shape component in a cool environment to avoid further significant creep deformation.

The physical experimental rig set, including the pressure forming die set and the pressure control circuit, can be seen in figure 6-7.

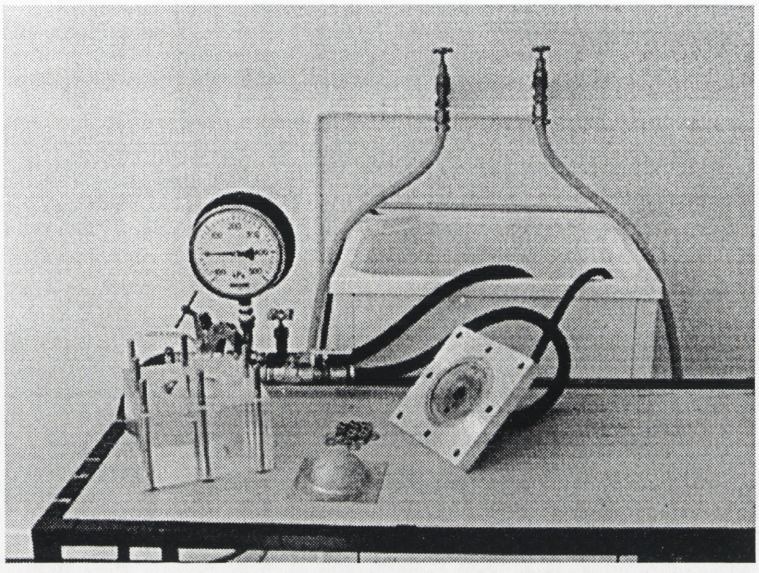

Figure 6-7: The disassembled pressure forming die set with a formed dome and the pressure control circuit set.

6.3 Experiments and Results

6.3.1 Pilot Experiments

The pilot experiments were conducted before the formal experiments start. Figure 6-8 shows four dome height increment curves with respect to time. All these four curves have similar trends despite of the different forming conditions. The dome height increased very fast at the beginning because of the high stress occuring at this stage. Then a much slower speed of the dome height increment was used until the dome was about 27 mm high. Finally the speed increased slightly and remained till the end of the process. From this figure we can see that higher pressure and higher temperature accelerate the forming process. Based on these pilot experiments, temperature $72 \sim 74^oC$ and pressure 300 kPa were chosen as the typical forming conditions for the following experiments.

Figure 6-9 shows a formed dome. The smoothness of the formed domes was similar, except the one formed at 62^oC and 150 kPa which had obvious surface imperfections.

6.3.2 Formal Experiments

There were two kinds of sheet thickness profile involved in the formal experiments, 2 mm constant thickness and the optimised thickness by which 1 mm constant dome

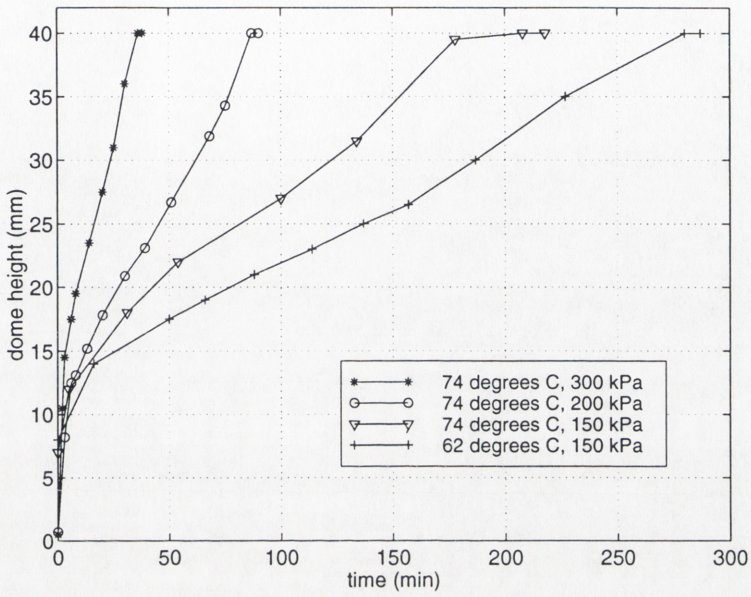

Figure 6-8: Dome height increment with respect to time. The initial sheet thicknesses are 2 mm.

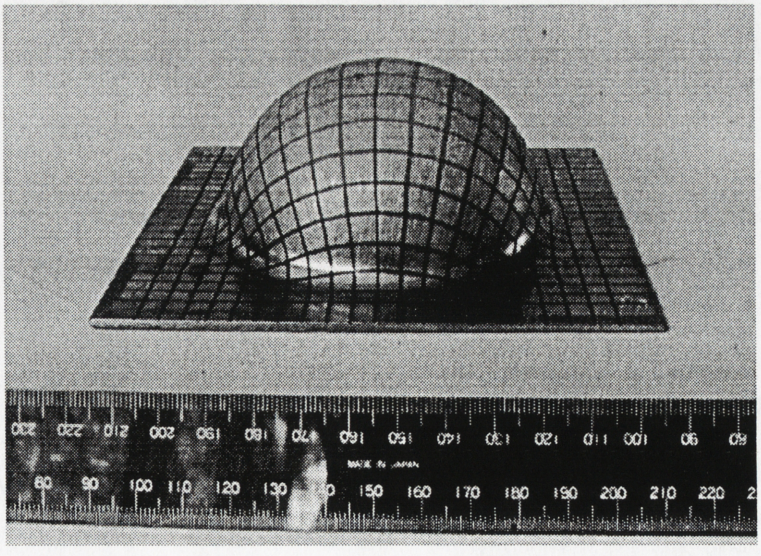

Figure 6-9: A whole formed dome.

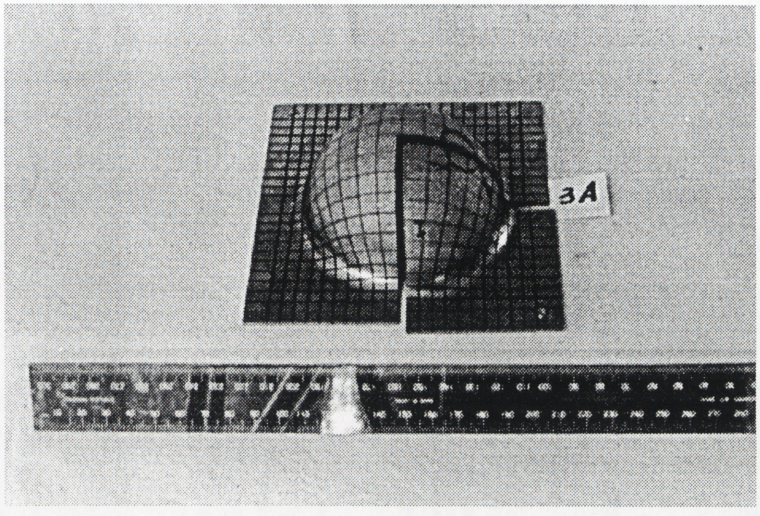

Figure 6-10: A dome cut by EDM.

thickness was expected.

Because the Sn-Pb alloy sheet is too soft to undertake the clamping force, it was glued onto a flat aluminium block which was held on the work bench of the CNC machine in the surface milling process. Iced coolant was used to reduce the temperature of the sheet in the milling process. After being milled, the glue holding the sheet was dissolved by acetone. Hence the optimised sheet thickness profile could be achieved.

In order to measure final thickness, it is necessary to cut up the domes along orthogonal axes. To achieve a neat section across the dome, electro-discharge machining (EDM) was employed to cut a quarter of the formed dome off (figure 6-10). The two half cross-sections of the one-quarter piece were measured by a sliding calliper at the points with 5 mm arc length intervals from the dome centre. The cross-section thickness profile of a dome was then plotted using the average value of the two sections.

Formings with Constant Sheet Thickness

Three 2 mm thick sheets, 2A, 3A and 6C were formed under the conditions of temperature $72 \sim 74^oC$ and pressure 300 kPa. Figure 6-11 shows these three dome section thickness profiles being formed. The horizontal coordinate is the arc length starting from the centre point of the dome, whereas the vertical coordinate is the thickness of the dome. These three profiles are compared well to each other except in the area

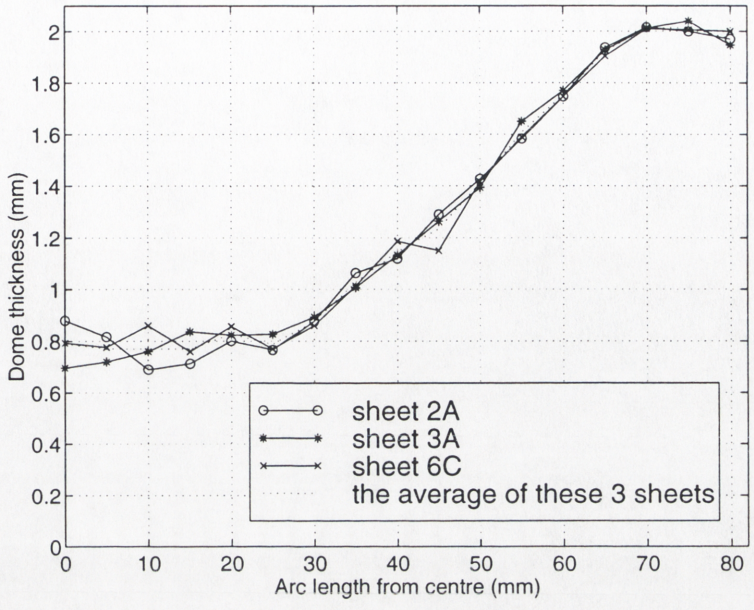

Figure 6-11: Three dome section thickness profiles with initial sheet thickness 2 mm, temperature $72 \sim 74^oC$ and pressure 300 kPa.

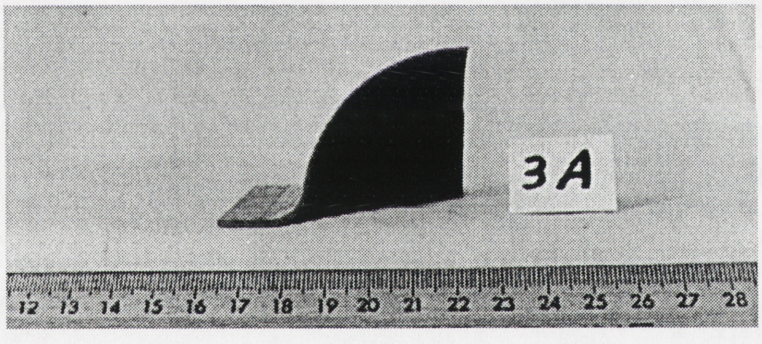

Figure 6-12: The section photo of dome 3A.

around the centre point. This may be caused by the larger strain in this area which tends to lead local thinning. The average section thickness profile of the three domes is plotted in a dotted line, which is considered as the typical experimental thickness profile (T=2mm)[2]. The photo of a quarter of dome 3A is shown in figure 6-12.

An additional task of these pilot experiments is to find the proper values of the strain rate sensitivity m and the friction coefficient μ. ABAQUS simulation results of dome thickness profiles (T=2 mm) with different values of the strain rate sensitivity m and the friction coefficient μ are plotted in figure 6-13 and 6-14 respectively.

[2]The comparisons of the simulation and experiment in the later section will be conducted based on this profile, instead of the individual profiles.

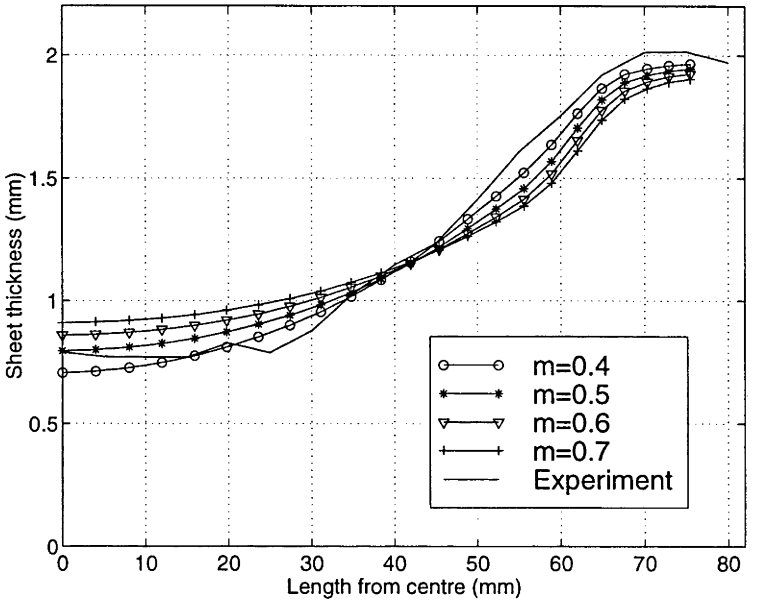

Figure 6-13: ABAQUS simulation of dome section thickness profile by various values of strain rate sensitivity m while friction coefficient μ is 0.5.

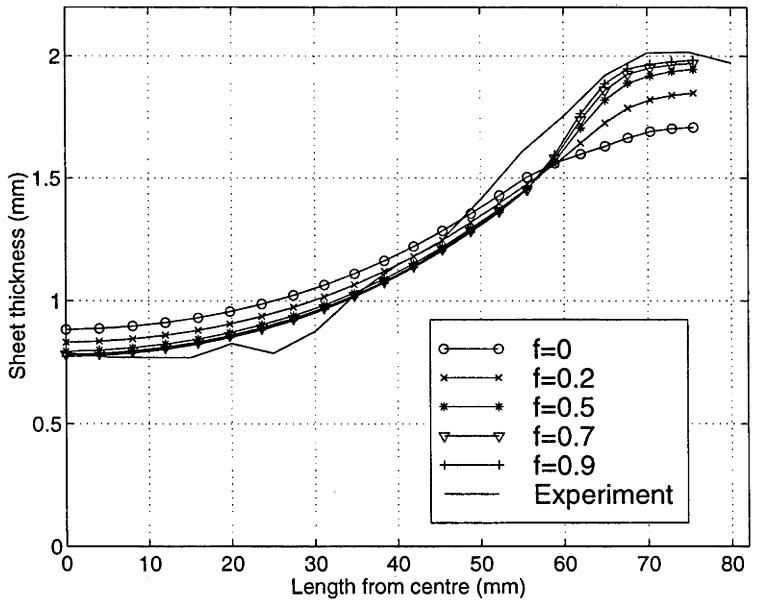

Figure 6-14: ABAQUS simulation of dome section thickness profile by various values of friction coefficient μ while strain rate sensitivity m is 0.5.

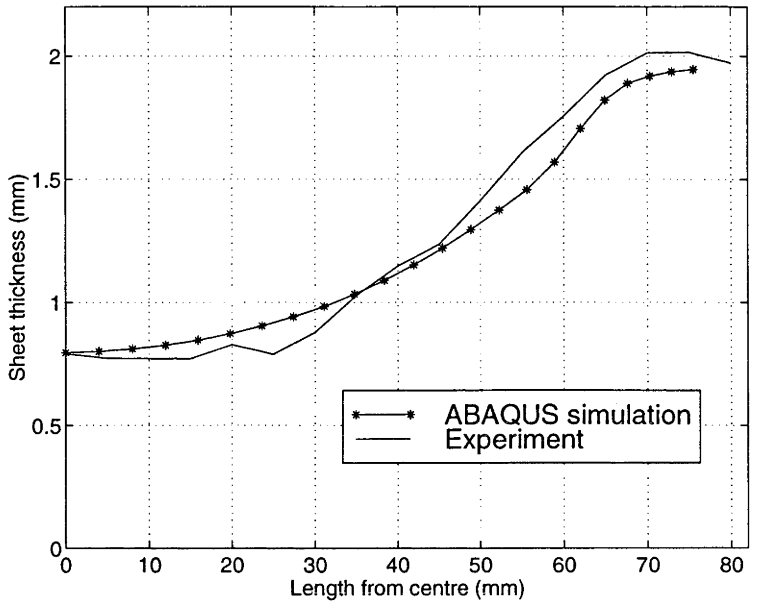

Figure 6-15: The comparison of dome thickness profiles by ABAQUS simulation and experiments.

From figures 6-13 we can see that larger strain rate sensitivity m leads to thicker thickness in the central and thinner around the edge, and the four profiles are distributed evenly. After comparing these profiles with the experimental one, $m = 0.5$ was chosen for the following ABAQUS simulations. In figure 6-14 we can observe that different small values up to 0.5 of friction coefficient μ give quite different profiles, whereas the profiles of large μ almost overlap to each other. Considering that 0.9 and 0.7 are too large for the Sn-Pb alloy and the perspex, $\mu = 0.5$ was chosen as the friction coefficient.

With the complete material properties, ABAQUS simulation was performed again, and the result is plotted in figure 6-15 where the profile by experiments is presented as well. The centre point has exactly the same value for both of the profiles. But at the area around the centre point, the simulation profile has higher values than those of experiments. However thinner simulation thickness exists near the dome fringe.

Forming towards a constant dome thickness profile

An optimised sheet thickness profile, towards 1 mm constant dome thickness, was achieved by 50 iterations of the proportional control algorithm, with $p = 0.8$ and the initial constant sheet thickness 1.5mm. Half cross-sections of this optimised sheet

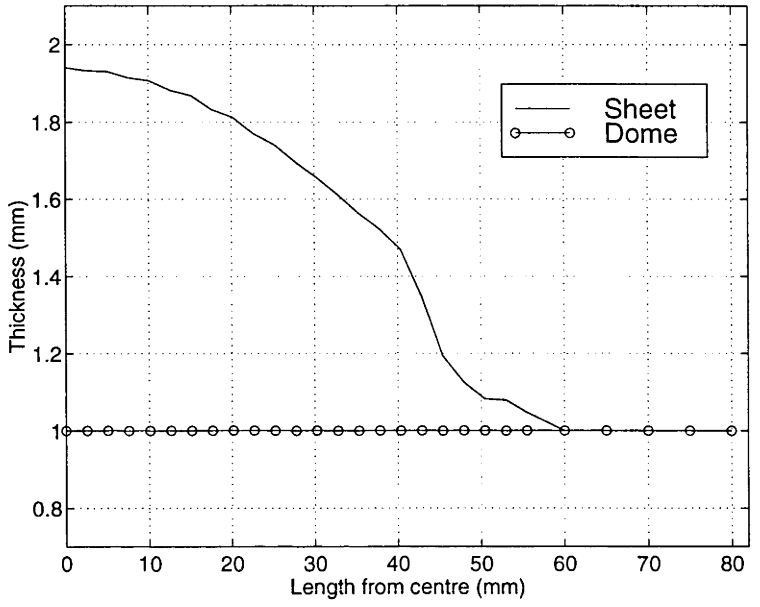

Figure 6-16: The optimised sheet thickness profile using the proportional control algorithm and its corespondent dome thickness profile by ABAQUS.

thickness profile and its correspondent dome thickness profile by ABAQUS are shown in figure 6-16.

The half cross-section of the sheet exhibits a sigmoidal shape thickness profile. The dome centre is the thickest point whose thickness is 1.94 mm, whereas the point 60 mm away from the centre is 1 mm thick which is consistent with the fact that there is no deformation occuring at this point in the forming process. Also there is a distinct convex shape in the sheet profile around 40mm. However good constant dome thickness profile is derived from this optimised sheet by ABAQUS simulation. The dome thickness is towards 1mm, and the biggest error -5.224×10^{-4}mm occurs at 12.61 mm away from the centre. Such a little error can be treated as *zero* in practice, and therefore "error-free" optimised sheet thickness profile by ABAQUS has been obtained.

Two 2 mm thick Sn-Pb alloy sheets, 2B and 4C, were milled by CNC machine using 8 mm ball-nose mill tool so that they were endowed with the optimised sheet thickness profile predicted by ABAQUS. The same forming conditions as previous experiments, temperature $72 \sim 74^oC$ and pressure 300 kPa , were then applied to these sheets, and the resultant half dome cross-section thicknesses are exhibited in figure 6-17. These two profiles are consistent with each other. However slight differences occur at the central area and the edge. This is because the large deformation in the central tended

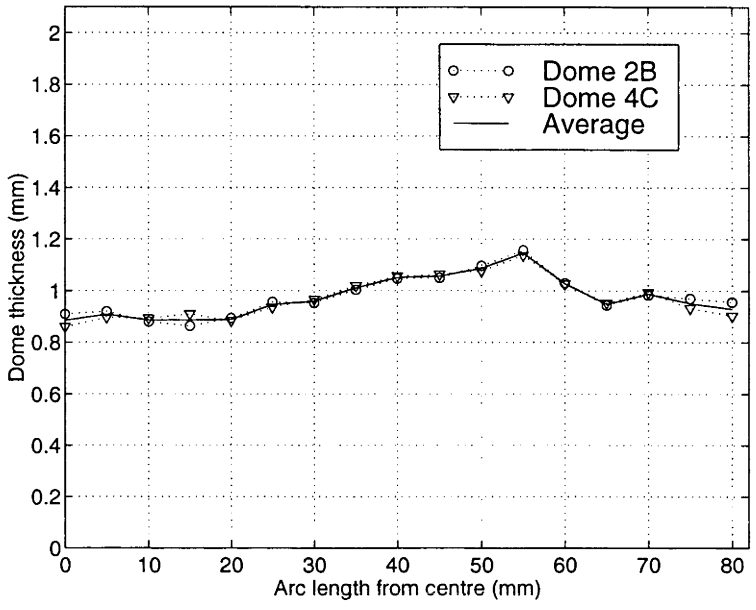

Figure 6-17: Dome section thickness profiles with optimised sheet thickness profile, temperature $72 \sim 74°C$ and pressure 300 kPa.

to lead to local thinning and the deformation by the clamping teeth at the edge was significant to the sheet thickness which was only 1mm at the edge. The average of these two profiles is plotted by a solid line which will be regarded as the typical experimental dome thickness profile using the optimised sheet thickness by ABAQUS simulations.

Generally the average profile in figure 6-17 is close to the target thickness 1mm. However there is a significant subsequent convex shape, where the thickness is up to 15% larger than required, existing around the area 55mm away from the dome centre. Less deformation in the convex shape led to more deformations in the other parts so that the thicknesses around the central and the edge are less than 1mm. This may be caused by either the homogeneity in the material properties or the numerical difficulties that ABAQUS had in simulating the SPF process.

To eliminate the influence of the undesired convex shape in the optimised sheet thickness profile, this profile was modified manually as shown in figure 6-18. Sheet 1B was machined into this profile and formed under the same conditions. Its dome cross-section thickness profile is displayed in figure 6-19 [3]. There was no significant convex

[3]Due to the difficulty of the glue thickness control, unnegligible error, 0.08mm thicker, of the milled sheet thickness occured. To compensate this undesired influence of the glue, the plotting of the dome thickness profile in this figure has been floated down 0.06mm.

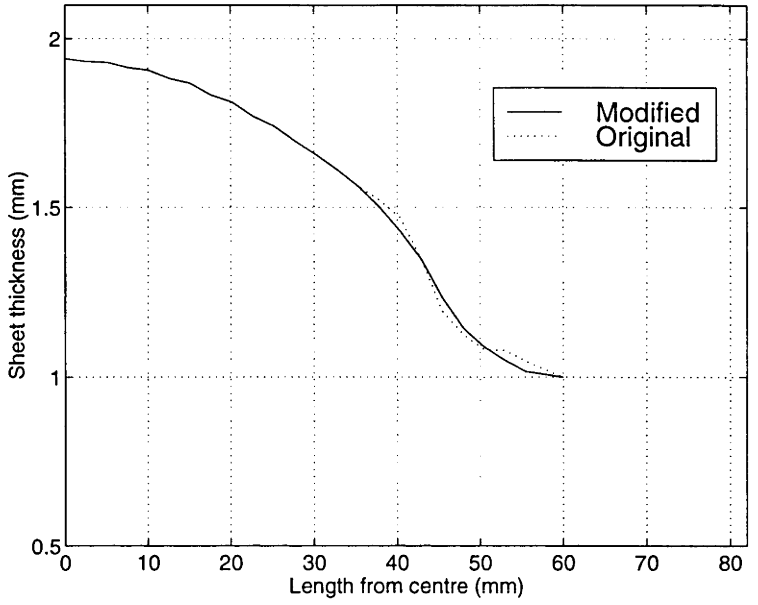

Figure 6-18: The modified optimised sheet thickness profile comparing with the original profile.

and concave shapes in this profile. The largest error, 9%, occured at 45mm away from the dome centre. Section photos of dome 2B, 4C and 1B are shown in figure 6-20.

6.4 Discussion

Dome formings are conducted by applying either constant sheet thickness of 2mm or the optimised sheet thickness profile and its modified version, as well as tensile testing.

Tensile tests show the superplastic properties of Sn-Pb alloy have strong relation with strain rate and temperature. Elongations up to 602% are achieved under the conditions of the crosshead speed 5mm/hour and the temperature $29 \sim 35^oC$.

The dome forming with 2 mm thick sheet has shown a reasonable agreement with the ABAQUS simulations when applying 0.5 for both the strain rate sensitivity m and the friction coefficient. Good agreement has also been achieved in the dome formings with the optimised profile, especially with the modified optimised profile. However errors between ABAQUS simulations and the experiments do occur. Quite a few factors, such as the estimated material propertied, numerical errors in the ABAQUS simulations, the impurities of the material, the influence of mounting glue on the sheet thickness profile and so on, can contribute to this error.

These experiment proved that the product thickness profile can be well controlled

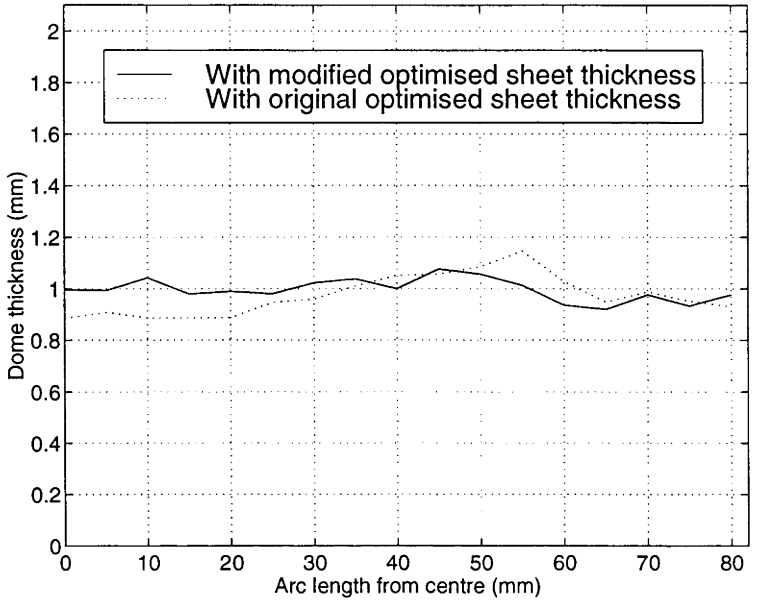

Figure 6-19: The dome thickness profile by the modified optimised sheet thickness profile comparing with the profile by the original optimised sheet thickness profile.

by the optimisation of sheet thickness profile using FEA simulations.

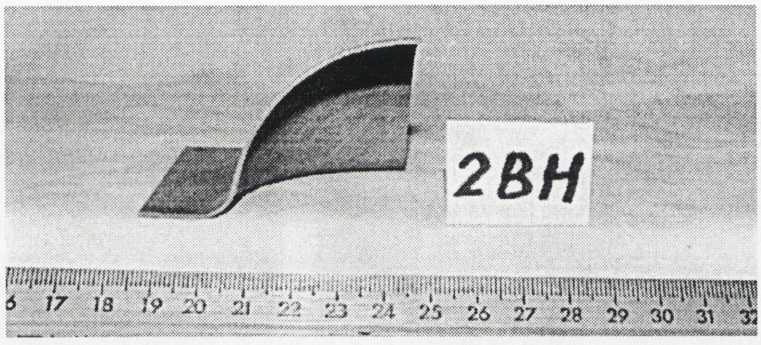

(a)

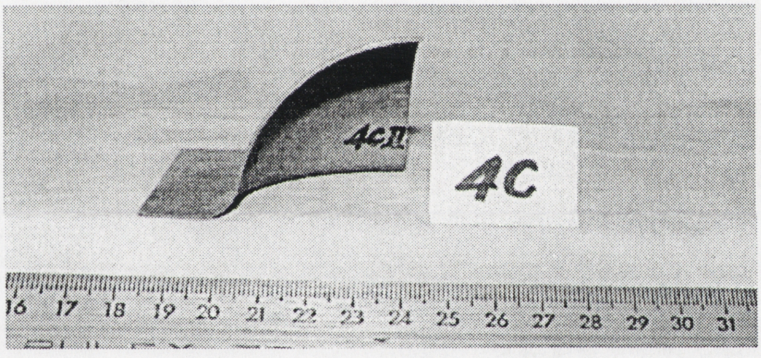

(b)

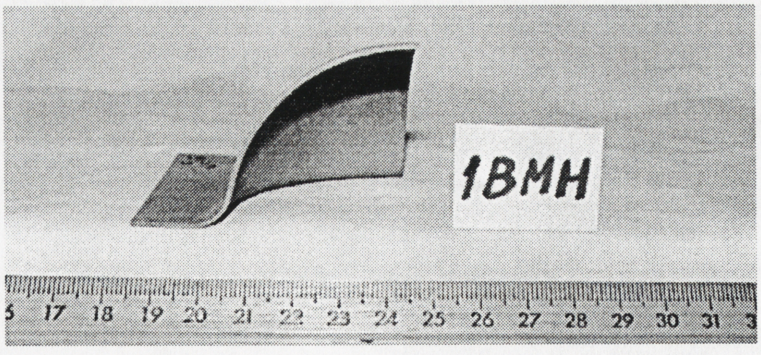

(c)

Figure 6-20: The section photos of dome 2B, 4C and 1B.

Chapter 7

Conclusion

7.1 Summary of Conclusions

Gradient Search and Proportional Control Method

Two optimisation methods, gradient search and proportional control, were adopted in the sheet thickness optimisation in SPF. Good optimisation criterion convergences can be achieved by both of the methods. They share some common characteristics, as well as possess their own distinguishing features.

These two methods all have an uncertain parameter, λ in gradient search and p in proportional control. There exist optimal constant values, λ^* and p^*, which can lead to the fastest convergences.

For the convenience of further discussion, the regions $\lambda < \lambda^*$ and $p < p^*$ are defined as region I of λ and p, and the region $\lambda > \lambda^*$ and $p > p^*$ as region II.

Decreases of λ and p in region I, or increases in region II will all cause decline of convergent speed or even failure in convergence. However large fluctuations of convergent speed occur in region II, and small fluctuations in region I, with respect to the changes of λ and p. The convergent speed is more sensitive to the values of λ and p in region II than in region I. The reason may be that, while λ and p are working in region II, excessive feedback leads to significant changes in sheet thicknesses so that dramatic variations occur in the consequent component thickness.

The optimal value of $\lambda^* = 0.45$ in the simple dome model is much higher than $\lambda^* = 0.2$ in pan model whose geometry is relatively complicated. This would imply a

sensitivity to geometric shape. Much slower convergent speed can be obtained if $\lambda = 0.2$ is applied in dome model, whereas no convergence can be obtained when $\lambda = 0.45$ in the model of pan. On the other hand, 0.9 and 0.8 are the values of p^* for dome, pan and 3-D box models, and they are quite close. Almost same good criterion convergence can be achieved if $p = 0.8$ is applied in dome model, and acceptable result will come out when $p = 0.9$ in the case of 3-D box. These indicate that values of λ^* in gradient search are completely different from model to model, and conversely different models can share one value of p with the promise that a compatible result is achievable, although it is not the p^* in some cases.

Significant difference also exists between the computational efficiencies of gradient search and proportional control techniques. In the dome model, the gradient search method spent 3 hours to obtain the final criterion at which proportional control arrived within 2 minute, 1.1% of 3 hours. Nevertheless, promising optimisation was achieved within 24 hours by proportional control on the model of 3-D box where years would be required if gradient search is applied.

It is worth noting that there was only one solution for each model, where the sheet thickness profile tended to reach. This indicates that the assumption of unimodality is valid.

The results and comparison of gradient search and proportional control method indicate that, acceptable optimised sheet thickness profile can be obtained by both of these methods. However the proportional control approach presented is easy to be implemented, and can yield a more accurate sheet profile within much less time. Its applicable area covers three dimensional models where gradient search will never reach in practice with current simulation times.

Tensile Testing and Experiments

The tensile testing shows that the superplastic property of Sn-Pb alloy has strong relation with strain rate and temperature applied, and exhibited good ductility in the temperature $29 \sim 35^oC$.

A dome model was adopted in the experiments by applying Sn-Pb alloy. Formings was conducted using both 2 mm sheet and the sheet with optimised profile towards 1 mm dome thickness. Good agreements were achieved in both kinds of the experiments.

No larger than 12% errors occured between the simulation and experiment in the formings with 2 mm sheet. However the largest error occured in the formings of optimised sheet profile was 15%. By using slightly modified optimised sheet thickness profile, the largest error reduced to 9%.

Whilst the aims of the project have been met, the results obtained were prone to three basic sources of error. First, due to lack of proved material properties needed in the ABAQUS simulations, some of the material properties were estimated by curve-fittings with the simulation results. Secondly numerical difficulty in ABAQUS itself brought a certain amount of error. Finally, limited by the manufacturing technology applied, small but non-negligible error remained in the thickness profile.

7.2 Recommendations

As a continuation of the research presented in this thesis, the following work or improvement could be the basis for possible future work.

Experiments on more complicated geometric models, for instance a 3-D box, are desirable in order to access the applicability of the optimisation strategies used, especially the proportional control method, to more general applications.

A CNC machine was employed to achieve the optimised thickness profile on the sheets. More economical technologies need to be investigated in order to obtain application of the thickness control of initial sheet thickness for simple and complex parts.

As previously discussed, the computational time could be reduced by applying a more reasonable estimated initial sheet thickness where the optimisation starts. Therefore strategies on the estimation of initial sheet thickness are worth investigating.

Further more, the proportional control strategy could be employed in the execution of FEA. The current situation is that no intermediate information is available, unless ABAQUS execution is completed. A better strategy would be to monitor the change of the thickness at each iteration of the simulation. Once it exceeds a certain range, compensation can then be applied to the correspondent areas. Roughly 50% of computational time could be saved by this method. Such an approach would require access to the FEA core code or the writing of a specific package for SPF.

Bibliography

[1] K. Higashi. Unpublished research. University of Osaka Prefecture, 1992.

[2] C.E. Pearson. Viscous Properties of Extruded Eutectic Alloys of Pb-Sn and Bi-Sn. *Journal of Industry Metals*, 54:111–123, 1934.

[3] T.G. Nieh, J. Wadsworht and O.D. Sherby. *Superplasticity in Metals and Ceramics.* Cambridge University Press, The Pitt Building, Trumpington Street, Cambridge CB2 IRP, United Kingdom, 1st edition, 1997.

[4] C.H. Hamilton and A.K. Ghosh. Superplastic Sheet Forming. In *Forming and Forging, ASM Handbook Vol 14.* ASM International, Metals Park, Ohio 44073, USA, 1988.

[5] D.L. Holt. An Analysis of the Bulging of a Superplastic Sheet by Lateral Pressure. *Int. J. Mech. Sci.*, 12:491, 1970.

[6] John Pilling and Norman Ridley. *Superplasticity in Crystalline Solids.* The Institute of Metals, 1989.

[7] C.H.M. Jenkins. Strength of Cd-Zn and Sn-Pb Alloy Solder. *J. Inst. Metals*, 40:21–32, 1928.

[8] E.E. Underwood. A Review of Superplasticity and Related Phenomenon. *J. Metals*, 14:914–919, 1962.

[9] T.H. Thomsen, D.L. Holt and W.A. Backofen. Forming Superplastic Sheet Metal in Bulge Dies. *Met. Eng. Quart.*, 2:1–12, 1970.

[10] P. Chaudhari. *Superplasticity, Science and Technology.* Springer-Verlag, Berlin, Germany, 1968. 42-75.

[11] A.A. Presnyakov. *Sverkhplastichnost' Metallov i Splavov (Superplasticity of Metals and Alloys).* The British Library, Wetherby, England, 1976.

[12] Jung-Ho Cheng. A Procedure for Designing Initial Thickness Variation for Superplastic Free Inflation. *International Journal of Mechanical Sciences*, 36(11):981–1000, 1994.

[13] D. Lee and W.A. Backofen. Superplasticity in Some Titanium and Zirconium Alloys. *Trans. AIME*, 239:1034–1040, 1967.

[14] W.A. Backofen, I.R. Turner and D.H. Avery. Superplasticity in Al-Zn Alloy. *Trans. ASM*, 57:980–990, 1964.

[15] A.K. Ghosh and C.H. Hamilton. Mechanical Behavior and Hardening Characteristics of a Superplastic Ti-6Al-4V Alloy. *Metall. Trans*, 10A:699–706, 1979.

[16] A.K. Ghosh. Deformation of Polycrystals: Mechanisms and Microstructures. In N. Hansen, editor, *Proceedings of the Second Riso International Symposium on Metallurgy and Materials Science*, page 277, 1981.

[17] E. R. Petty. The Deformation Behaviour of Some Aluminium Alloys Containing Intermetallic Compounds. *Journal of Industry Metals*, 91:274–279, 1962-63.

[18] M.J. Stowell, R. Grimes and B.M. Watts. Superplastic Aluminium-based Alloys. *Metals Technology*, 3:154–160, 1976.

[19] C. H. Hamilton. Superplasticity in Titanium Alloys. In B. Baudelet and M Suery, editor, *Superplasticite*, pages 14.11–14.16. Centre Nationale de la Recherche Scientifique, 1985.

[20] M. T. Cope, D. R. Evetts and N. Ridley. Superplastic Deformation Characteristics of Two Microduplex Titanium Alloys. *Journal of Materials Science*, 21:4003–4008, 1986.

[21] J. R. Leader, D. F. Neal and C. Hammond. The Effect of Alloying Additions on the Superplastic Properties of Ti-6Al-4V Alloy. *Metallurgical Transactions A*, 17:93–106, 1986.

[22] A. Wisbey and P. G. Partridge. Superplastic Deformation in a High Temperature Ti Alloy IMI-834. In S. Hori, M. Tokizane and N. Furushiro, editor, *Superplasticity in Advanced Materials*, pages 465–470. Japan Society for Research on Superplasticity, 1991.

[23] Q. Liu, W. Yang and G. Chen. On Superplasticity of Two Phase α-Titanium-Intermetallics Ti-(Co,Ni)-Al Alloys. *Acta Metall. Mater.*, 43:3571–3582, 1995.

[24] M.M. Tilman and L.A. Neumaier. *Superplasticity in Commercial and Experimental Compositions of Magnesium Alloy Sheet.* RI 8662. Bureau of Mines, U.S. Department of the Interior, 1982.

[25] G.D. Smith and H.L. Flower. Superplastic Forming of Alloy 718. *Adv. Mater. Proc.*, 145(4):32–34, 1994.

[26] O.W. Davis, C.F. Osborne and G.J. Brooks. Progress in Superplasticity II. Designing parts of superplastic alloys. *Met. Eng. Quartly*, page 5, Nov 1973.

[27] W. Johnson, T.Y.M. Al-Naib and J.L. Duncan. Superplastic Forming Techniques and Strain Distributions in a Zn-Al Alloy. *J. Inst. Met.*, 100:45, 1972.

[28] R. Hawkins and J.A. Belk. Deep Drawing of Superplastic Material. *Met. Technol.*, pages 516–521, Nov 1976.

[29] T.Y.M. Al-Naib and J.L. Duncan. Superplastic Metal Forming. *Int. J. Mech. Sci.*, 12:463, 1970.

[30] J.R. Williamson. Diffusion Bonding in SPF/DB. In *Proceedings of the American Welding Society*, Las Vegas, NV, 1982.

[31] O.D. Sherby, J. Wadsworth, R.D. Caligiuri, L.E. Eiselstein, B.C. Snyder and R.T. Whalen. Superplastic Bonding of Ferrous Laminates. *Scr. Metall.*, 13:941–946, 1979.

[32] E.D. Weisert and G.W. Stacher. Concurrent Superplastic Forming/Diffusion Bonding of Titanium. In N.E. Paton and C.H. Hamilton, editor, *Superplastic Forming of Structural Alloys.* TMS-AIME, Warrendale, PA, 1982.

[33] A.K. Ghosh. Tensile Instability and Necking in Materials with Strain Hardening and Strain-Rate Hardening. *Acta Metall.*, 25:1413–1424, 1977.

[34] F.A. Nichols. Plastic Instabilities and Uniaxial Tensile Ductilities. *Acta Metall.*, 28:663–673, 1980.

[35] N.E. Paton and C.H. Hamilton. Microstructural Influences on Superplasticity in Ti-6Al-4V. *Metall. Trans. A*, 10A:241–250, 1979.

[36] F.A. Mohamed and T.G. Langdon. Flow Localisation and Neck Formation in a Superplastic Metal. *Acta Metall.*, 29:911–920, 1981.

[37] G.G.W. Clemas, S.T.S. Al-Hassani and W. Johnson. The Bulging of a Superplastic Sheet from a Square Die. *Int. J. Mech. Sci.*, 17:711, 1975.

[38] J. Belk. A Quantitative Model of the Blow-Forming of Spherical Surfaces in Superplastic Sheet Metal. *Int. J. Mech. Sci.*, 17:505–511, 1975.

[39] G.J. Cocks, C. Rowbottom and D.M.R. Taplin. Bulge Forming Characteristics of Two Superplastic Cu Alloys. *Met. Technol.*, pages 332–337, July, 1976.

[40] J. Argyris and J. St. Doltsinis. In A. Sawczuk and G. Bianchi, editor, *Plasticity Today*, page 715. Elsevier, 1985.

[41] K.S.K. Chockalingam, M. Neelakantan, S. Devaraj and K.A. Padmanabhan. On the Pressure Forming of Two Superplastic Alloys. *J. Mater. Sci.*, 20:1310–1320, 1985.

[42] Yu-Quan Song and Zhao Jun. A Mechanical Analysis of the Superplastic Free Bulging of Metal Sheet. *Mater. Sci. Eng.*, 84:111–125, 1986.

[43] A.K. Ghosh and C.H. Hamilton. On Constant Membrane Stress Test for Superplastic Metals. *Metall. Trans. A*, 11A:1915–1918, 1980.

[44] C.H. Hamilton. Formability: Analysis, Modelling and Experimentation. The Metallurgical Society, 1977.

[45] A.K. Ghosh and C.H. Hamilton. *Process Modelling: Fundamentals and Applications to Metals.* American Society for Metals, 1979.

[46] F. Jovane. An Approximate Analysis of the Superplastic Forming of a Thin Circular Diaphragm: Theory and Experiments. *Int. J. Mech. Sci.*, 10:403–427, 1968.

[47] G.C. Cornfield and R.H. Johnson. The Forming of Superplastic Sheet Metal. *Int. J. Mech. Sci.*, 12:479, 1970.

[48] R. Courant. Variational Methods for the Solution of Problem of Equilibrium and Vibrations. *Bull. Amer. Math. Soc.*, 49:1–23, 1943.

[49] M.J. Turner, R.W. Clough, H. C. Martin and L. J. Topp. Stiffness and Deflection Analysis of Complex Structures. *Journal of Aeronautical Sciences*, 23(9):805–824, 1956.

[50] *ABAQUS/Theory Manual*, 5.5 edition.

[51] *ABAQUS/Explicit User's Manual*, 5.5 edition.

[52] J. Bonnet, R. D. Wood and O. C. Zienkiewicz. Modelling of the Superplastic Forming of Thin Sheet. *Superplasticity and Superplastic Forming, The Minerals, Metals and Material Society*, 1988.

[53] J. C. Nagtegaal and G. J. Davies. Comparison of Implicit and Explicit Finite Element Method for Analysis of Sheet Forming Problems. In *FE-Simulation of 3-D Sheet Metal Forming Processes in Automotive Industry, V.D.I. Berichte NR. 894*, pages 705–724, 1991.

[54] N. Rebelon,J. C. Nagtegaal, L. M. Taylor and R. Passman. Comparison of Implicit and Explicit Finite Element Methods in the Simulation of Metal Forming Processes. In *Numerical Methods in Industry Forming Processes*, 1992.

[55] J. Bonnet, R. D. Wood and R. Collins. Pressure Control Algorithms for the Numerical Simulation of Superplastic Forming. *International Journal of Mechanical Science*, 36:297–309, 1994.

[56] J. Bonnet, R. D. Wood and A. H. S. Wargadipura. Numerical Simulation of the Superplastic Forming of Thin Sheet Components Using the Finite Element Method. *International Journal for Numerical Methods in Engineering*, 30:1719–1737, 1990.

[57] E. Massoni, M. Bellet and J. L. Chenot. Thin Sheet Forming Numerical Analysis with a Membrane Approach. *Modelling of Metal Forming Processes, Kluwer Academic Publisher*, pages 187–196, 1988.

[58] M. Bellet and J. L. Chenot. Numerical Modelling of Thin Sheet Superplastic Forming. In *Numerical Methods in Industry Forming Processes*, 1989.

[59] S. C. Rama and N. Chandran. Development of a Pressure Prediction Method for Superplastic Forming Processes. *International Journal of Non Linear Mechanics*, 26:711–725, Nov. 1992.

[60] S. C. Rama and N. Chandran. Application of Finite Element Method to the Design of Superplastic Processes. *Journal of Engineering for Industry*, 114:452–458, Nov. 1992.

[61] *ABAQUS/Standard Example Problems Manual*, 5.5 edition.

[62] Roger Fletcher. *Practical Methods of Optimisation.* John Wiley & Sons, Ltd, 1980.

[63] L.R. Foulds. *Optimisation Techniques.* Springer-Verlag New York Inc., 1981.

[64] D.M. Burley. *Studies in Optimisation.* John Wiley & Sons, Ltd, 1974.

[65] Douglass J. Wilde. *Optimum Seeking Methods.* Prentice-Hall, Inc., 1964.

[66] S.L.S. Jacoby, J.S. Kowalik and J.T. Pizzo. *Iterative Methods for Nonlinear Optimisation Problems.* Prentice-Hall, Inc., Englewood Cliffs, New Jersey, 1972.

[67] R. Hooke and T.A. Jeeves. Direct Search Solution of Numerical and Statistical Problems. *Journal of the ACM*, 8:212, 1961.

[68] W. Spendley, G.R. Hext and F.R. Himsworth. Sequential Application of Simplex Designs in Optimisation and Evolutionary Operation. *Technometrics*, 4:441, 1962.

[69] J. A. Nelder and R. Mead. A Simplex Method for Function Minimisation. *Computer Journal*, 7:308–313, 1965.

[70] J.H. Schneibel and P.M. Hazzledine. The Role of Coble Creep and Interface Control in Superplastic Sn-Pb Alloys. *Journal of Materials Science*, 18:562–570, 1983.

[71] C.H. Hamilton, K. Zhang, M. Khraisheh and H.M. Zbib. Superplastic Flow under Transient Conditions and Multiaxial Stresses. In Amit K. Ghosh and Thomas R. Bieler, editor, *Superplasticity and Superplastic Forming*, pages 181–187. The Minerals, Metals & Materials Society, 1995.

[72] A.E. Geckinli and C.R. Barrett. Superplastic Deformation of the Pb-Sn Eutectic. *Journal of Materials Science*, 11:510–521, 1976.

Appendix A

Listings

A.1 ABAQUS Input Deck of Simulation

A.1.1 2-D Dome

```
*HEADING
SUPERPLASTIC FORMING -- 2-D DOME / AUTOMATIC LOADING
*RESTART, WRITE, FREQUENCY=30
**-----------------------------------------------
** SHEET DEFINITION
**-----------------------------------------------
*NODE
1,  0.,  20.
23, 28., 20.
*NGEN,NSET=PLATE
1, 23, 1
*ELEMENT, TYPE=MAX1, ELSET=SHEET1
1, 1, 2
*ELGEN, ELSET=SHEET1
1, 21, 1, 1, 1
*NSET, ELSET=SHEET1, NSET=NCONT
*ELEMENT, TYPE=MAX1, ELSET=SHEET2
22, 22, 23
*ELSET, ELSET=SHEET
SHEET1, SHEET2
*MEMBRANE SECTION, ELSET=SHEET, MATERIAL=SUPRAL, NODAL THICKNESS
*NODAL THICKNESS, INPUT=T23.inp
**-----------------------------------------------
```

```
** MATERIAL IS CLOSE TO SUPRAL100 AT 470C
**-----------------------------------------------
*MATERIAL, NAME=SUPRAL
*ELASTIC
10.3E6, 0.34
*CREEP, LAW=TIME
1.48E-9, 2., 0.
**-----------------------------------------------
** CONTACT SURFACE DEFINITION
**-----------------------------------------------
*NODE, NSET=DIE
10000, 0.0, 0.0
*RIGID SURFACE, NAME=DOME, TYPE=SEGMENTS, REF NODE=10000,
FILLET RADIUS=4.0
START, -1., 0.
LINE,  0.,  0.
CIRCL, 20.,  20.,  0., 20.
LINE,  30.,  20.
*CONTACT NODE SET, NAME=SLAVES
NCONT,
*CONTACT PAIR, INTERACTION=DIE_MET
SLAVES, DOME
*SURFACE INTERACTION, NAME=DIE_MET
*FRICTION
0.2
**-----------------------------------------------
** BOUNDARY AND INITIAL CONDITIONS
**-----------------------------------------------
*BOUNDARY
PLATE, 3, 5
1,     1
1,     6
23,    1,3
10000, 1,6
*INITIAL CONDITIONS, TYPE=STRESS
SHEET, 1., 1.
*AMPLITUDE, DEFINITION=SOLUTION DEPENDENT, NAME=AUTO
1., 1.E-03, 1000.
**-----------------------------------------------
** STEP 1
```

```
**-----------------------------------------------
*STEP, INC=30, NLGEOM
*STATIC
0.0002, 1., 1.0E-8
*DLOAD
SHEET, P, -0.2
*CONTACT PRINT, FREQUENCY=100
*CONTACT FILE, FREQUENCY=100
*END STEP
**-----------------------------------------------
** STEP 2
**-----------------------------------------------
*STEP, INC=500, NLGEOM
*VISCO, CETOL=0.0075
0.002, 2000., 1.0E-8
*DLOAD, AMPLITUDE=AUTO
SHEET, P, -0.2
*CREEP STRAIN RATE CONTROL, ELSET=SHEET, AMPLITUDE=AUTO
0.02
*EL PRINT, ELSET=SHEET, FREQUENCY=500, POSITION=AVERAGED AT NODES
STH,
*EL FILE, ELSET=SHEET, FREQUENCY=500, POSITION=AVERAGED AT NODES
STH,
*END STEP
```

A.1.2 2-D Box

```
*HEADING
SUPERPLASTIC FORMING SIMULATION -- 2-D BOX / AUTOMATIC LOADING
*RESTART, WRITE, FREQUENCY=30
**-----------------------------------------------
** SHEET DEFINITION
**-----------------------------------------------
*NODE
1,  0.,  20.
23, 28., 20.
*NGEN, NSET=PLATE
1, 23, 1
*ELEMENT, TYPE=MAX1, ELSET=SHEET1
```

```
1, 1, 2
*ELGEN, ELSET=SHEET1
1, 21, 1, 1, 1
*NSET, ELSET=SHEET1, NSET=NCONT
*ELEMENT, TYPE=MAX1, ELSET=SHEET2
22, 22, 23
*ELSET, ELSET=SHEET
SHEET1, SHEET2
*MEMBRANE SECTION, ELSET=SHEET, MATERIAL=SUPRAL, NODAL THICKNESS
*NODAL THICKNESS, INPUT=T23.inp
**-----------------------------------------------
** MATERIAL IS CLOSE TO SUPRAL100 AT 470C
**-----------------------------------------------
*MATERIAL, NAME=SUPRAL
*ELASTIC
10.3E6, 0.34
*CREEP, LAW=TIME
1.48E-9, 2., 0.
**-----------------------------------------------
** CONTACT SURFACE DEFINITION
**-----------------------------------------------
*NODE, NSET=DIE
10000, 0.0, 0.0
*RIGID SURFACE, NAME=BOX, TYPE=SEGMENTS, REF NODE=10000,
FILLET RADIUS=4.0
START, -1., 0.
LINE,  0.,  0.
LINE,  20., 0.
LINE,  20., 20.
LINE,  30., 20.
*CONTACT NODE SET, NAME=SLAVES
NCONT,
*CONTACT PAIR, INTERACTION=DIE_MET
SLAVES, DOME
*SURFACE INTERACTION, NAME=DIE_MET
*FRICTION
0.2
**-----------------------------------------------
** BOUNDARY AND INITIAL CONDITIONS
**-----------------------------------------------
```

```
*BOUNDARY
PLATE, 3, 5
1,     1
1,     6
23,    1, 3
10000, 1, 6
*INITIAL CONDITIONS, TYPE=STRESS
SHEET, 1., 1.
*AMPLITUDE, DEFINITION=SOLUTION DEPENDENT, NAME=AUTO
1., 1.E-03, 1000.
**-----------------------------------------------
** STEP 1
**-----------------------------------------------
*STEP, INC=30, NLGEOM
*STATIC
0.0002, 1.0, 1.0E-8
*DLOAD
SHEET, P, -0.2
*CONTACT PRINT, FREQUENCY=100
*CONTACT FILE, FREQUENCY=100
*END STEP
**-----------------------------------------------
** STEP 2
**-----------------------------------------------
*STEP, INC=500, NLGEOM
*VISCO, CETOL=0.0075
0.002, 2000.0, 1.0E-8
*DLOAD, AMPLITUDE=AUTO
SHEET, P, -0.2
*CREEP STRAIN RATE CONTROL, ELSET=SHEET, AMPLITUDE=AUTO
0.02
*EL PRINT, ELSET=SHEET, FREQUENCY=500, POSITION=AVERAGED AT NODES
STH,
*EL FILE, ELSET=SHEET, FREQUENCY=500, POSITION=AVERAGED AT NODES
STH,
*END STEP
```

A.1.3 3-D Box

```
*HEADING
 SUPERPLASTIC FORMING SIMULATION -- 3-D BOX / AUTOMATIC LOADING
*RESTART, WRITE, FREQUENCY=30
**-----------------------------------------------
** PLATE DEFINITION
**-----------------------------------------------
*NODE
1,     4.0, 20.0,  -4.0
23,   26.0, 20.0,  -4.0
3201,  4.0, 20.0, -36.0
3223, 26.0, 20.0, -36.0
*NGEN, NSET=EDGE3
1, 3201, 100
*NGEN, NSET=EDGE5
23, 3223, 100
*NFILL, NSET=PLATE
EDGE3, EDGE5, 22, 1
*NSET, NSET=EDGE1, GENERATE
1, 23, 1
*NSET, NSET=EDGE7, GENERATE
3201, 3223, 1
*NSET, NSET=CENTER
1,
*ELEMENT, TYPE=M3D4, ELSET=PLATE1
1, 1, 2, 102, 101
*ELGEN, ELSET=PLATE1
1, 21, 1, 1, 31, 100, 100
*NSET, ELSET=PLATE1, NSET=NCONT
*ELEMENT, TYPE=M3D4, ELSET=PLATE2
22,   22,   23,   123,  122
3101, 3101, 3102, 3202, 3201
*ELGEN, ELSET=PLATE2
22,   32, 100,100
3101, 21, 1,  1
*ELSET, ELSET=PLATE
PLATE1, PLATE2
*MEMBRANE SECTION, ELSET=PLATE, MATERIAL=SUPRAL
0.15
```

```
**-----------------------------------------------
** MATERIAL IS CLOSE TO SUPRAL100 AT 470C
**-----------------------------------------------
*MATERIAL, NAME=SUPRAL
*ELASTIC
10.3E6, 0.34
*CREEP, LAW=TIME
1.48E-9, 2.0, 0.
**-----------------------------------------------
** CONTACT SURFACE DEFINITION
**-----------------------------------------------
*NODE, NSET=DIE
10000, 0.0, 0.0, 0.0
*RIGID BODY, ELSET=ERIGID, REF NODE=10000
*NODE, INPUT=402040a.inp
*ELEMENT, TYPE=R3D3, ELSET=ERIGID, INPUT=402040b.inp
*SURFACE DEFINITION, NAME=DIE
ERIGID, SPOS
*CONTACT NODE SET, NAME=SLAVES
NCONT,
*CONTACT PAIR, INTERACTION=DIE_NODE
SLAVES,DIE
*SURFACE INTERACTION, NAME=DIE_NODE
**-----------------------------------------------
** BOUNDARY AND INITIAL CONDITIONS
**-----------------------------------------------
*BOUNDARY
EDGE1, 3
EDGE7, 2, 3
EDGE3, 1
EDGE5, 1, 2
10000, 1, 6
*INITIAL CONDITIONS, TYPE=STRESS
PLATE, 1.0, 1.0
*AMPLITUDE, DEFINITION=SOLUTION DEPENDENT, NAME=AUTO
1.0, 0.1, 1000.
*NSET, NSET=NSELECT
101, 121, 1001, 1101, 1507, 2509
1,   113, 1211, 1308, 1408, 1508, 1509, 1705
**-----------------------------------------------
```

```
** STEP 1
**-----------------------------------------------
*STEP, INC=30, NLGEOM
*STATIC
2.0E-3, 1.0,
*DLOAD
PLATE, P, -0.2
*CONTACT PRINT, FREQUENCY=100
*CONTACT FILE, FREQUENCY=100, NSET=NSELECT
*EL PRINT, ELSET=PLATE , FREQUENCY=100
S, E
CE
SINV
*PRINT, CONTACT=YES
*NODE PRINT, NSET=EDGE3, FREQUENCY=100
U
*NODE FILE, NSET=EDGE3, FREQUENCY=100
U
*END STEP
**-----------------------------------------------
** STEP 2
**-----------------------------------------------
*STEP, INC=500, NLGEOM
*VISCO, CETOL=0.005
0.2, 2000.0
*DLOAD, AMPLITUDE=AUTO
PLATE, P, -0.2
*CREEP STRAIN RATE CONTROL, ELSET=PLATE, AMPLITUDE=AUTO
0.02
** IN ORDER TO WRITE THE AUTOMATIC SOLUTION CONTROL VARIABLES
** AMPCU AND RATIO TO THE RESULTS FILE EVERY INCREMENT
** SUCH FILE HAS TO BE ACTIVATED
*NODE FILE, NSET=CENTER, FREQUENCY=1
U
*END STEP
```

A.2 ABAQUS Input Deck of Experiment

The following ABAQUS input deck file is used to simulation the Sn-Pb alloy sheet formed in the experiments.

```
*HEADING
SUPERPLASTIC FORMING SIMULATION -- 2-D DOME (Sn-Pb) CONSTANT LOADING
*RESTART, WRITE, FREQUENCY=30
**-----------------------------------------------
** length: 2mm=0.07874inch, R8mm=0.315inch
**         40mm=1.5748inch, R55.5mm=2.185inch
**-----------------------------------------------
** forming presure:          300kpa=43.6 lb/in^2
** Young's modulus:          10GPa=1.45E6 lb/in^2
** coefficient A:            50MPa=7.254E3 lb/in^2
** friction coefficient:     0.5
** strain rate sensitivity: 0.5
** Poisson's ratio:          0.34
**-----------------------------------------------
** SHEET DEFINITION
**-----------------------------------------------
*NODE
1,  0.0,   1.5748
23, 2.185, 1.5748
*NGEN, NSET=PLATE
1, 23, 1
*ELEMENT, TYPE=MAX1, ELSET=SHEET1
1, 1, 2
*ELGEN, ELSET=SHEET1
1, 21, 1, 1, 1
*NSET, ELSET=SHEET1, NSET=NCONT
*ELEMENT, TYPE=MAX1, ELSET=SHEET2
22, 22, 23
*ELSET, ELSET=SHEET
SHEET1, SHEET2
*MEMBRANE SECTION, ELSET=SHEET, MATERIAL=SUPRAL, NODAL THICKNESS
*NODAL THICKNESS, INPUT=T23.inp
**-----------------------------------------------
** MATERIAL IS Sn-Pb EUTECTIC ALLOY AT 74C
**-----------------------------------------------
```

```
*MATERIAL, NAME=SUPRAL
*ELASTIC
1.45E6, 0.34
*CREEP, LAW=TIME
19.0E-9, 2.0, 0.0
**-----------------------------------------------
** CONTACT SURFACE DEFINITION
**-----------------------------------------------
*NODE, NSET=DIE
10000, 0.0, 0.0
*RIGID SURFACE, NAME=DOME, TYPE=REVOLUTION, REF NODE=10000,
FILLET RADIUS=0.315
0, 0, 0, 0, 1, 0
START, 0.0000,  0.0000
CIRCL, 1.5748,  1.5748,  0.000, 1.5748
LINE,  2.5000,  1.5748
*CONTACT NODE SET, NAME=SLAVES
NCONT,
*CONTACT PAIR, INTERACTION=DIE_MET
SLAVES, DOME
*SURFACE INTERACTION,NAME=DIE_MET
*FRICTION
0.5
**-----------------------------------------------
** BOUNDARY AND INITIAL CONDITIONS
**-----------------------------------------------
*BOUNDARY
PLATE, 3, 5
1,     1
1,     6
23,    1, 3
10000, 1, 6
*INITIAL CONDITIONS, TYPE=STRESS
SHEET, 1.0,1.0
**-----------------------------------------------
** STEP 1
**-----------------------------------------------
*STEP, INC=30, NLGEOM
*STATIC
0.0002, 1.0, 1.0E-8
```

```
*DLOAD
SHEET,P,-43.60
*CONTACT PRINT, FREQUENCY=100
*CONTACT FILE, FREQUENCY=100
*END STEP
**-----------------------------------------------
** STEP 2
**-----------------------------------------------
*STEP, INC=500, NLGEOM
*VISCO, CETOL=0.0075
0.002, 7000.0, 1.0E-8
*DLOAD
SHEET, P, -43.60
*NODE PRINT, NSET=PLATE, FREQUENCY=50
U, COORD
*NODE FILE, NSET=PLATE, FREQUENCY=50
U, COORD
*EL PRINT,ELSET=SHEET,FREQUENCY=500,POSITION=AVERAGED AT NODES
STH,
*EL FILE,ELSET=SHEET,FREQUENCY=500,POSITION=AVERAGED AT NODES
STH,
*END STEP
```